

Comparing low-mass and high-mass star formation with protostellar outflows

MSc thesis

Femke Ballieux



Universiteit
Leiden
Observatory

Comparing low-mass and high-mass star formation with protostellar outflows

A thesis submitted in partial fulfillment
of the requirements for the degree of

Master of Science
in
Astronomy

Author:
Student ID:
Supervisor:
Second supervisor:
Second corrector:
Project duration:

Femke Ballieux
s2124149
Prof.dr. S. Viti
Dr. M.M.E. Bouvier
Dr. M.R. Hogerheijde
February 2024 – December 2024

Cover image:
Template style:
Template licence:

HH 211, ESA/Webb, NASA, CSA, T. Ray
Thesis style by Richelle F. van Capelleveen
Licenced under CC BY-NC-SA 4.0



Universiteit
Leiden
Observatory

P.O. Box 9513, 2300 RA Leiden, The Netherlands

Abstract

The process of high-mass ($M > 8M_{\odot}$) star formation is, unlike its low-mass counterpart, not well understood, due to the relative rarity of high-mass stars. Protostellar outflows are ubiquitous around protostars, and play an important role in enabling star formation and setting the star formation efficiency. In this work, we compare ALMA observations of protostellar outflows driven by low- and high-mass protostars, using low-J pure rotational transitions pf CO.

Our high-mass sample consists of five protoclusters selected from the ALMA-IMF program, and our low-mass sample consists of seven protostars in the ρ Ophiuchi cloud. Using the CO (1-0), CO (2-1), and CO (3-2) transitions, we identified outflows within these fields. We then derived rotational temperatures and CO column densities, using the rotational diagram method. In addition, we also derived some outflow parameters such as the radius (R), velocity extend (Δv), dynamical timescale (t_{dyn}), and opening angle (α).

We found that outflows driven by high-mass protostars have typically higher CO column densities, indicating they have more molecular material. They are also typically larger (weighted mean of $R = 2.7 \cdot 10^4 \pm 1 \cdot 10^3$ au) than outflows in our low-mass sample (weighted mean of $R = 6.5 \cdot 10^2 \pm 5 \cdot 10^1$ au), and they have higher velocities (weighted mean of $\Delta v = 1.57 \cdot 10^3 \pm 0.07 \cdot 10^3$ yr) compared to their low-mass counterparts (weighted mean of $\Delta v = 3.2 \cdot 10^2 \pm 0.2 \cdot 10^2$ yr). From these findings, we concluded that outflows driven by high-mass protostars are likely more massive and more energetic compared to outflows driven by low-mass outflows.

Furthermore, we found that outflows in the high-mass sample typically have longer dynamical timescales than outflows in the low-mass sample, by a factor of ~ 5 .

Finally, we determined the opening angles of the outflows in our low- and high-mass samples, and we found that outflows driven by high-mass protostars are more collimated than those driven by low-mass protostars, despite the high-mass protostars living in more clustered environments and their outflows therefore being more likely to be disturbed. We can explain these smaller opening angles by the outflows in the high-mass sample being more energetic, allowing them to remain collimated.

As we find that outflows in the high-mass sample are well-collimated, we might interpret this as evidence against the Competitive Accretion model, where it would be expected that outflows behave more chaotically. We could therefore conclude that high-mass stars form according to the same mechanisms as low-mass stars. However, a number of other mechanisms influence the widening of protostellar outflows, therefore no firm conclusion can be drawn.

Acknowledgements

I would like to express my sincere gratitude to my supervisors, Dr. Mathilde Bouvier and Prof. Dr. Serena Viti, for their invaluable guidance and for giving me the freedom to shape the direction of this project. I also wish to thank Dr. Michiel Hogerheijde, the second corrector of this work, for his time and attention in reviewing this thesis.

A special thank you to my office mates, both in office HL4.26 and in office BW3.22a, whose company has been a constant source of support throughout this master's. In particular, I want to thank Nikki, who has been going through it with me during these past few months, and Wout, my "rubber ducky" that actually talks back.

This work makes use of the following ALMA data: ADS/JAO.ALMA#2017.1.01355.L, ADS/JAO.ALMA#2018.1.01679.S, ADS/JAO.ALMA#2017.1.00914.S . ALMA is a partnership of ESO (representing its member states), NSF (USA) and NINS (Japan), together with NRC (Canada), NSTC and ASIAA (Taiwan), and KASI (Republic of Korea), in cooperation with the Republic of Chile. The Joint ALMA Observatory is operated by ESO, AUI/NRAO and NAOJ. This publication makes use of data products from the Two Micron All Sky Survey, which is a joint project of the University of Massachusetts and the Infrared Processing and Analysis Center/- California Institute of Technology, funded by the National Aeronautics and Space Administration and the National Science Foundation. This work makes use of the following software: CARTA (Comrie et al., 2018), CASA Team et al. (2022), NumPy (Harris et al., 2020), Matplotlib (Hunter, 2007)

Contents

Abstract	iii
Acknowledgements	iv
List of Tables	vii
List of Figures	viii
1 Introduction	1
1.1 High- and low-mass star formation	1
1.2 Protostellar outflows	4
1.3 Aims of this research	9
2 Source sample & observations	10
2.1 High-mass protoclusters	10
2.2 Low-mass protoclusters	12
3 Determination of physical parameters	15
3.1 Methodology	15
3.1.1 Inspecting the datacubes	15
3.1.2 Smoothing and regridding	15
3.1.3 Integrated emission maps	16
3.1.4 Determination of noise levels and clipping	16
3.1.5 Local thermodynamic equilibrium	17
3.1.6 Radiative transfer	18
3.1.7 Rotational diagram method	19
3.1.8 T_{rot} and $N_{\text{tot}}(\text{CO})$ determination	21
3.2 Results	21
3.2.1 Optically thick transitions in high-mass fields	22
3.2.2 Non-LTE or multiple component emission in low-mass fields	23

4 Morphology and outflow properties	25
4.1 Methodology	25
4.1.1 Integrated CO (2-1) maps	25
4.1.2 Outflow classifications	25
4.1.3 Radius determination	26
4.1.4 Outer velocity determination	26
4.1.5 Dynamical age determination	27
4.1.6 Opening angle determination	27
4.2 Results	30
4.2.1 Radii, velocities, and dynamical timescales	31
4.2.2 Opening angles	32
4.2.3 Details of individual outflows	32
5 Discussion	40
5.1 Comparing rotational temperatures	40
5.2 Molecular material in protostellar outflows	41
5.3 Differences in radius and velocity	43
5.4 Differences in the dynamical timescales	44
5.5 Opening angles in the low- and high-mass sample	46
5.6 The evolution of opening angles with age	48
6 Conclusions & future outlook	50
6.1 Conclusions	50
6.2 Future outlook	52
A Appendix	55
A.1 Constraining the physical high-mass parameters using <i>RADEX</i>	55
A.2 Rotational temperature and column density maps	57
A.3 Opening angle determination	68
Bibliography	82

List of Tables

2.1	Overview of the observations of the high-mass sample	12
2.2	Overview of the observations of the low-mass sample	14
3.1	The velocity ranges over which the CO emission was integrated	17
4.1	The morphological parameters for all outflows in this work	31
A.1	The input parameters for running <i>RADEX</i>	56

List of Figures

1.1	Overview of the constituents of a molecular cloud	2
1.2	Overview of the evolutionary sequence low-mass stars	3
1.3	Overview of different stages of high-mass star formation	4
1.4	Overview of a protostellar outflow	5
1.5	A proposed evolutionary sequence for the widening of protostellar outflows driven by a high-mass YSO	8
2.1	Overview of the high-mass protoclusters studied in this work	11
2.2	JWST NIRCam image of the ρ Ophiuchi cloud complex	13
3.1	CO (2-1) red-shifted integrated emission of G008.67	16
3.2	Example of a well-behaved rotational diagram of CO	20
3.3	T_{rot} and $N_{tot}(\text{CO})$ maps for G338.93.	22
3.4	Example of a deviated rotational diagram of CO	24
4.1	Integrated CO (2-1) emission showing the G328.25 outflow	29
4.2	Integrated CO (2-1) emission showing the Oph 26 outflow	30
4.3	Integrated CO (2-1) maps maps of sources in our low-mass sample. .	33
4.4	Integrated CO (2-1) maps of sources in our low-mass and high-mass sample.	34
4.5	Integrated CO (2-1) maps maps of sources in our high-mass sample. .	35
5.1	Mean values of the rotational temperatures	41
5.2	Mean column densities over the high- and low-mass fields	42
5.3	Dynamical timescales	45
5.4	Derived opening angles	46
5.5	Opening angles as function of dynamical timescale	48
5.6	The opening angles of outflows in the low-mass sample, as a function of the evolutionary stage	49

1 . Introduction

1.1 High- and low-mass star formation

Understanding star formation is at the core of the majority of contemporary astronomical research. Stars are the building blocks of the universe, star formation determines the structure and evolution of galaxies, almost all elements around us have been formed in stars, and the formation of planets is intrinsically linked to star formation.

Low-mass stars ($M \lesssim 8 M_{\odot}$) are the most abundant since they dominate the initial mass function (IMF), which is the distribution of stellar masses as they reach the main sequence (e.g. Kroupa, 2002; Chabrier, 2003). High-mass stars ($M \gtrsim 8 M_{\odot}$) are much rarer, constituting less than approximately 1% of the IMF (Rosen et al., 2020). However because of their extremely large luminosities ($\gtrsim 1 \cdot 10^3 L_{\odot}$, Kuiper, 1938) and mechanical impact on their environments (such as stellar winds and ionization), they play a dominant role in all kinds of processes (Tan et al., 2014). For example, they regulate the interstellar medium (ISM) by producing heavy elements, which are injected into the ISM through supernova explosions (e.g. Woosley et al., 2002). Furthermore, they enrich the ISM with dust (Dunne et al., 2003). Through feedback processes, they might also play a role in dispersing stellar clusters (Fall et al., 2010).

Although the process of low-mass star formation ($M \lesssim 8 M_{\odot}$) is quite well understood, the details of the high-mass star formation process are still widely debated (e.g. Tan et al., 2014), due to the rarity of high-mass stars and their consequent greater distance.

Star formation is a complex process, that occurs in large ($L \sim 10$ pc), dense ($N_H \gtrsim 10^3$ cm $^{-3}$), and cold ($T \sim 10$ K) giant molecular clouds (GMC) (e.g. Lada & Lada, 2003; Rosen et al., 2020). These clouds have a hierarchical structure, with increasing densities towards smaller structures. An example of the structure of a GMC is given in Figure 1.1.

A widely discussed hypothesis is that high-mass stars form through a scaled-up version of low-mass star formation (Shu et al., 1987). GMCs contain networks of filaments and clumps with a scale of ~ 1 pc and higher densities than the surrounding cloud. Within these clumps, gravitationally bound dense cores exist with typical sizes 0.1 pc. If these cores become gravitationally unstable, they undergo gravitational collapse via a central disk, to form one or multiple low-

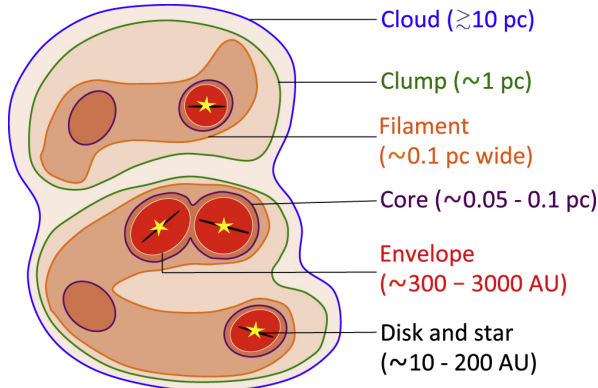


Figure 1.1: Schematic overview of the constituents of a molecular cloud, showing the low-mass star formation mechanism, in which clumps fragment into cores, that undergo gravitational collapse to eventually form stars. The image is not drawn to scale. Figure taken from Pokhrel et al. (2018).

mass young stellar objects (YSOs) with a surrounding envelope. In Figure 1.2, a schematic overview of the different stages of low-mass star formation is given.

The scenario in which high-mass stars form through a scaled-up version of the low-mass star formation model is called the 'Core Accretion' model. Similarly to low-mass star formation, self-gravitating, centrally concentrated cores form from a fragmenting clump. As these cores undergo gravitational collapse through a central disk, one or multiple high-mass YSOs form. In this scenario, the core represents the entire mass reservoir available for the formation of one massive, or multiple low-mass stars, and no mass is accreted from outside the core. A distinguishing feature of the Core Accretion model is that the shape of the pre-stellar core-mass function (CMF) is the same as the shape of the IMF (e.g. Tan et al., 2014).

Another widely considered hypothesis for high-mass star formation is 'Competitive Accretion' (Bonnell et al., 2001), in which high-mass stars accrete their mass chaotically from a wider region of the clump, that has never formed a consistent, gravitationally bound core. In this scenario, accretion occurs more efficiently near the center of the gravitational potential, and therefore the most massive stars would form in the center of a cluster. According to this model, high-mass stars would always form in a cluster in which the mass is dominated by low-mass stars, indicating that high- and low-mass stars form simultaneously. If the density of stars in the cluster center is sufficiently high, collisions might also assist in the formation of extremely massive stars. Competitive Accretion has been said to naturally produce the IMF (Bonnell et al., 2001), where massive stars form only a small fraction of the total stars formed. Observations show that high-mass star formation occurs in clustered environments, characterized by higher surface densities and larger velocity dispersions (e.g. Tan et al., 2014; Zhang et al., 2015; Rosen et al., 2020), which might be evidence for the Competitive Accretion model.

Low-mass YSOs are most often classified based on their infra-red spectral

slope (Lada, 1987; Andre & Montmerle, 1994; Greene et al., 1994), where Class 0 YSOs represent the earliest, deeply embedded stage of star formation. Class I sources are slightly more evolved YSOs, and Class II sources are T Tauri stars with gas-rich circumstellar disks.

A different low-mass YSO classification mechanism has been proposed (Whitney et al., 2003; Robitaille et al., 2006) that is based on physical characteristics, rather than observational properties. According to this mechanism, sources are either stage 0 in which they are deeply embedded, stage 1 in which they are less embedded, stage 2 in which they are classical T Tauri stars with gas-rich disks, and stage 3 in which they are main-sequence stars. Figure 1.2 gives an overview of the different evolutionary stages of low-mass YSOs.

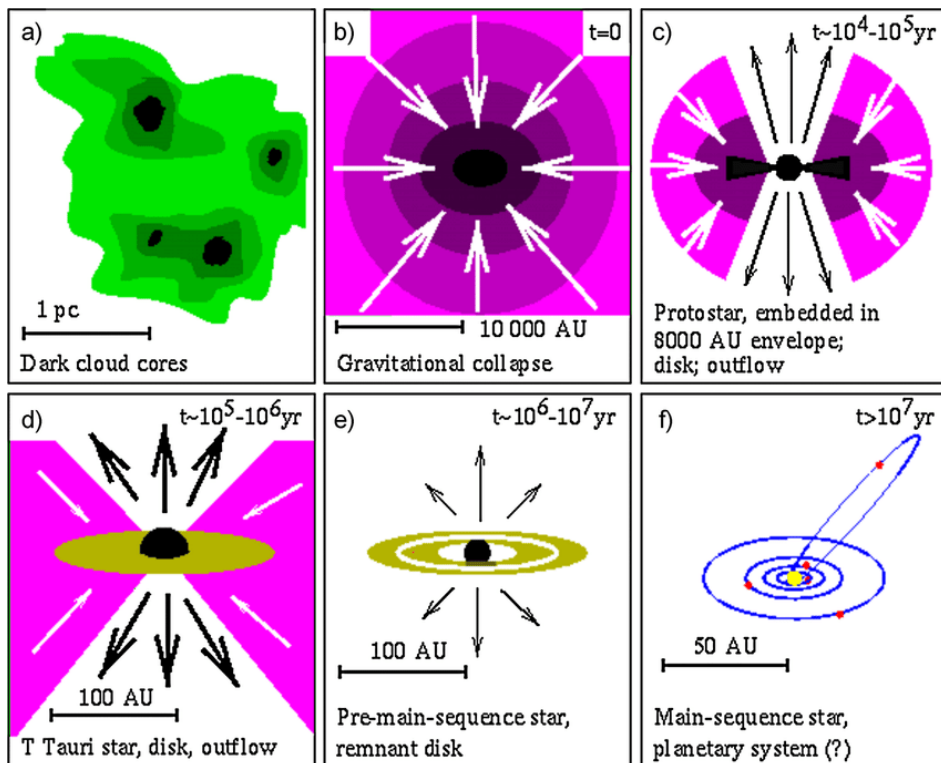


Figure 1.2: Schematic overview of the evolutionary sequence of a low-mass star. As cores undergo gravitational collapse, a protostar embedded in an envelope forms, accompanied by a disk and protostellar outflows. These protostars eventually evolve into T Tauri stars, which still have a disk and outflows. Eventually, a pre-main-sequence star forms, which evolves into a main-sequence star. The image was taken from Hogerheijde (1998)

An evolutionary sequence for high-mass star formation has been proposed (e.g. Walsh et al., 1999; Minier et al., 2003), which differs from the evolutionary sequence of low-mass star formation. After the initial collapse, the newly formed protostar will begin emitting UV photons. These photons cause the surrounding envelope to ionize, which is referred to as an ultra-compact HII (UCHII) region. As the ionization front expands, it forms a giant HII region. Eventually, the surrounding gas is blown away, revealing a high-mass star cluster. An overview of this evolutionary sequence can be found in Figure 1.3.

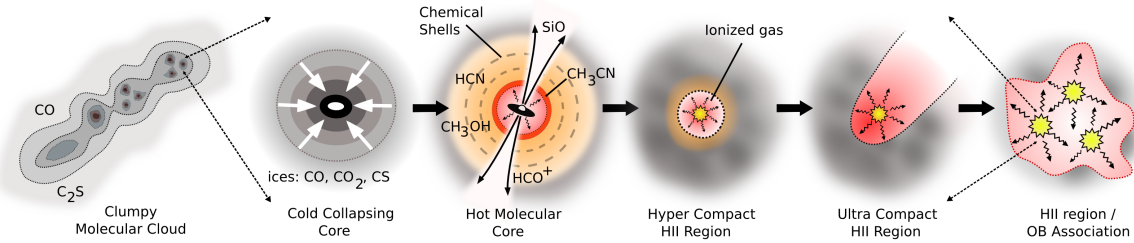


Figure 1.3: Schematic overview of different stages of high-mass star formation. Clumpy molecular clouds collapse through cold cores to hot cores, at which point protostellar outflows and heat from the central protostar evaporates ices from grains, causing a rich time-dependent chemistry. Due to UV photons emitted by the protostar, the surrounding medium becomes ionized (HII region). Massive stars often form in clusters. Image adapted from Purcell (2006)

1.2 Protostellar outflows

In the vicinity of the vast majority of both high- and low-mass YSOs, bipolar molecular outflows of high-velocity gas are detected (e.g. Bally & Lada, 1983; Edwards & Snell, 1982, 1983, 1984). These protostellar outflows consist of a range of morphologies, from collimated jets to less-collimated lobes, to barely-collimated spherical winds (Reipurth & Bally, 2001; Arce et al., 2011; Arce et al., 2013; Nakamura & Li, 2012). They range in velocity from a few km s^{-1} to over 10^3 km s^{-1} . Shocks further complicate the morphology of the outflow.

Their exact launching mechanism is still under debate (e.g. Bachiller, 1996; Tan et al., 2014), but for low-mass sources it is generally accepted that magnetocentrifugal acceleration from the disk region launches a jet, which entrains gas from the surrounding envelope (Bally, 2016; Pudritz & Ray, 2019). Outflows around high-mass stars rely on additional mechanisms, such as accretion via stellar collisions (Bonnell et al., 1998), radiative Rayleigh-Taylor instabilities (Krumholz & Matzner, 2009; Rosen et al., 2016), or dense filaments (Rosen et al., 2016). Protostellar outflows can be observed around low-mass sources from Class 0 to Class II sources (e.g. Bachiller, 1996; Bally, 2016). Although high-mass YSOs are rare, it has been found that protostellar outflows are ubiquitous around high-mass protostars as well (Beuther et al., 2002). Outflows are associated with significant mass loss. Low mass Class 0 YSOs have been seen to have a mass-loss rate up to $\sim 10^{-5} \text{ M}_\odot \text{ yr}^{-1}$ (Bally, 2016), and outflows driven by high-mass sources have been shown to have mass-loss rates from 10^{-5} to a few $\times 10^{-3} \text{ M}_\odot \text{ yr}^{-1}$ (Arce & Sargent, 2006).

A natural consequence of star formation is the launching of protostellar outflows, as these carry away angular momentum that would otherwise prevent core collapse. Conversely, protostellar outflows can start a negative feedback process, by clearing the dense gas surrounding the YSO, which limits further accretion (e.g. Nakano et al., 1995; Matzner & McKee, 2000; Hansen et al., 2012;

Cunningham et al., 2018; Rohde et al., 2020). Therefore, outflows likely set the star formation efficiency (SFE), which corresponds to the fraction of core mass that ends up in the protostar. The SFE has been estimated to be $\sim 0.3 - 0.5$ (Alves et al., 2007; Enoch et al., 2008; Könyves et al., 2015, 2020).

Protostellar outflows are most often observed using low- J ($J_{\text{upper}} \leq 3$) pure rotational transitions of CO (e.g. Williams et al., 2003; Plunkett et al., 2015; Bally, 2016). CO is abundant, the upper-energy levels of the lowest transitions are easily populated by collisions, and the rotational transitions trace the typical temperatures and column densities of molecular clouds. Furthermore, these CO rotational transitions are observable from the ground. Warmer regions in the outflows, such as shocks, are often traced by higher- J pure rotational transitions of CO, and by SiO, as these shocks can cause grain sputtering, which increases the abundance of SiO significantly compared to the surrounding cold gas (e.g. Schilke et al., 1997; Caselli et al., 1997; Gusdorf et al., 2008).

A schematic overview of the components of a protostellar outflow can be found in Figure 1.4, although it should be noted that real outflows are often more complex than indicated in the figure since interactions with the ISM, episodic activity and neighboring YSOs influence the shape of the outflow.

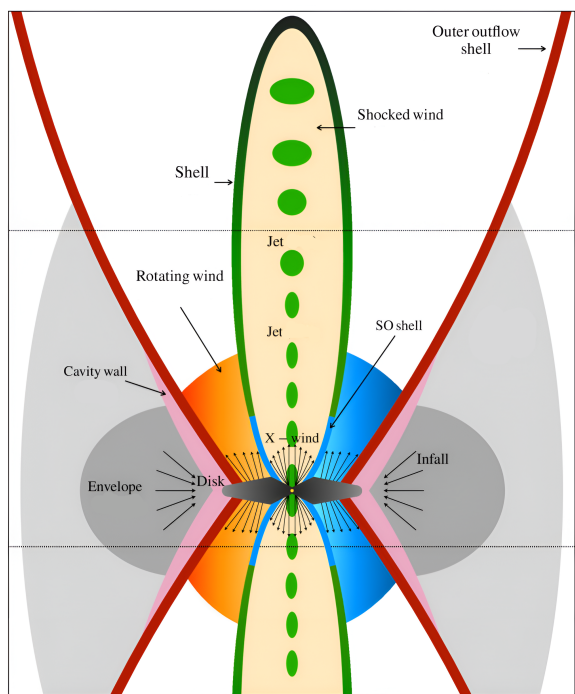


Figure 1.4: Schematic overview of a protostellar outflow, adapted from López-Vázquez et al. (2024). Indicated are the envelope, the protostellar disk, the jet, the outflow, and the infall regions. Further indicated are the shocked wind, a rotating wind, and the X-wind, which are components we do not discuss further in this thesis. Furthermore, this figure shows an SO shell, which is particular to the outflow studied in their work, and not a generic feature in protostellar outflows. Not indicated are possible cavities within the outflow.

Outflow temperatures

Rotational temperatures for outflows (around low-mass sources) are usually determined using low-J pure rotational lines of CO and CO isotopologues in the mm and sub-mm regime. These lines trace the cold gas ($T_{\text{ex}} \leq 10 - 50$ K) in the outflow and the envelope (e.g. Lada, 1985; Blake et al., 1995; Bontemps et al., 1996; Yıldız et al., 2012; Dunham et al., 2014). Observations of high excitation lines of CO trace warmer gas and find cavity walls with temperatures of $T \sim 100$ K (Yıldız et al., 2012). There are thus multiple different components of the outflow and envelope, with a range of temperatures. In this project, we only study low-J transitions, and therefore only trace the colder component.

Van Kempen et al. (2016) study outflows around intermediate-mass sources ($3 M_{\odot} < M < 8 M_{\odot}$) and find temperature limits of $T_{\text{ex}} \lesssim 50$ K, which is in agreement with temperature limits found for low-mass protostars.

Due to the rarity of high-mass YSOs, no general temperature range is known for outflows around high-mass protostars. McKee & Tan (2003) state that once a massive star is formed, temperatures of the surrounding gas may rise to $T \sim 50 - 100$ K, however at earlier stages outflows emerge from gas that has the same temperature range as low-mass stars.

Outflow column densities

CO column densities trace the amount of molecular material in a region. Tychoniec et al. (2019) study five outflows in the Serpens Main star-forming region, around two low-mass YSOs, and one YSO in between a low-mass and an intermediate-mass protostar (SMM1, a multiple system containing three outflow-driving sources). They determine CO column densities separately for slow ($|v - v_{\text{LSR}}| \lesssim 15 \text{ km s}^{-1}$), fast ($15 \lesssim |v - v_{\text{LSR}}| \lesssim 50 \text{ km s}^{-1}$), and extremely high velocity (EHV, $|v - v_{\text{LSR}}| \gtrsim 50 \text{ km s}^{-1}$) outflows. For the low-mass protostars, they find that the slow outflow components have CO column densities ranging from $4 \cdot 10^{16}$ to $5 \cdot 10^{17} \text{ cm}^{-2}$, while the fast outflows have CO column densities ranging between $5 \cdot 10^{15}$ and $3 \cdot 10^{17} \text{ cm}^{-2}$. For the outflows around slightly more massive YSOs (although not yet high-mass YSOs), they find the slow outflows have CO column densities ranging between $6 \cdot 10^{16}$ and $6 \cdot 10^{17} \text{ cm}^{-2}$, while the fast outflows have CO column densities ranging between $1 \cdot 10^{16}$ and $3 \cdot 10^{17} \text{ cm}^{-2}$.

Lefloch et al. (2015) study the Cepheus E protostellar outflow, which is an outflow driven by an intermediate-mass protostar. They find that the emission traced by low-J CO lines is cold ($T_{\text{kin}} = 80 - 100$ K), with a typical column density of $N(\text{CO}) = 9 \cdot 10^{16} \text{ cm}^{-2}$, while the emission traced by high-J lines is warm ($T_{\text{kin}} = 400 - 750$ K) with lower column densities $N(\text{CO}) = 1.5 \cdot 10^{16} \text{ cm}^{-2}$.

Although a specific range for low-J CO column densities is not known for protostellar outflows around high-mass stars due to their rarity, Li et al. (2018) find that properties like outflow mass, momentum, and energy are typically two orders of magnitude higher for their high-mass protostars, compared to typical values for low-mass protostars. Therefore, we expect outflows around high-mass sources to have higher CO column densities than outflows around low-mass sources.

Dynamical timescales

In many protostellar outflows, a ‘Hubble-like’ relationship in outflows between velocity and distance to the YSO has been observed (e.g. Stahler, 1994; Lada & Fich, 1996), where the velocity of the outflow increases linearly with the distance from the YSO. Such a relationship suggests that the dynamical timescale, defined as the radius divided by the velocity of an outflow, remains constant throughout the outflow.

Outflows are associated with accretion and can be highly episodic, on timescales from weeks to years (e.g. Billot et al., 2012; Safron et al., 2015; Mairs et al., 2017). Mass loss from protostellar outflows seems to increase with accretion rate (e.g. Ellerbroek et al., 2013). Li et al. (2020) find that the time between consecutive ejection events, and therefore episodic accretion events, decreases as a source evolves. They also find that the dynamical timescale increases with core masses, which indicates that more massive cores have longer accretion timescales than less massive cores. Therefore, we expect outflows in our high-mass sample to have longer dynamical timescales compared to outflows in our low-mass sample.

Opening angles

In low-mass protostars, the increase of the outflow opening angle with age seems to be a general trend, which has been shown both observationally and through simulations (e.g. Velusamy & Langer, 1998; Arce & Sargent, 2006; Lee & Ho, 2005). As a source evolves, the outflow becomes less collimated, until outflows around Class II sources have no definable structure.

Staff et al. (2019) find a similar relation for high-mass sources from 3D magnetohydrodynamic simulations. They find that as the high-mass sources evolve and accrete more mass, the opening angles of associated outflows increase as well. They state that the reason for this widening is likely related to the outflow eroding the protostellar envelope and widening the outflow cavity over time.

Richer et al. (2000) find a lack of well-collimated outflows in samples of high-mass protostars, suggesting outflows driven by low-mass protostars have smaller opening angles than outflows driven by high-mass protostars. However, this result might be biased by selection effects, as relatively few massive protostars were identified at the time. Wu et al. (2004) study a sample of low- and high-mass protostars and associated protostellar outflows, and determine the collimation factor of these outflows by considering the outflow to be an ellipsoid, calculating the area and the major axis, and then deriving the minor axis. The ratio between the major and minor axes is the collimation factor. They find average collimation factors of 2.05 ± 0.96 for the high-mass sample, and 2.81 ± 2.16 for the low-mass sample, and therefore find that protostellar outflows around low-mass protostars are more collimated than outflows around high-mass protostars. Beuther et al. (2002) disagree with these findings, and instead find similar collimation factors between outflows driven by high- and low-mass sources.

Beuther & Shepherd (2005) indicate several different reasons for this discrepancy; either some observations were wrongly interpreted, there exist multiple physically different modes of massive star formation, or the observed sources

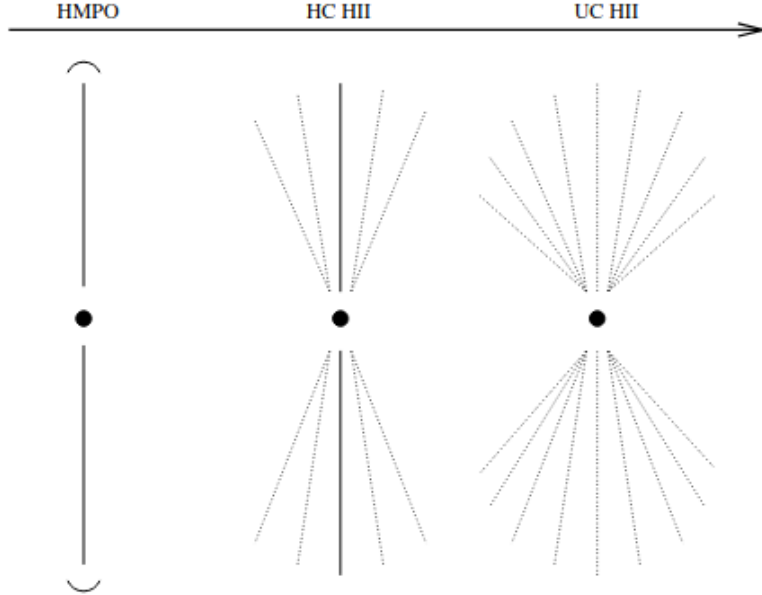


Figure 1.5: A proposed evolutionary sequence for the widening of protostellar outflows driven by a high-mass YSO. A jet-like outflow around the high-mass protostellar object (HMPO) dominates initially, until a hyper-compact HII (HC HII) region forms, that launches an additional wide-angled wind component. Eventually, a UC HII region forms and the winds start to dominate. The image was taken from Beuther & Shepherd (2005).

might not be comparable due to different evolutionary stages. The first might be true for some single-dish observations since low spatial resolution can significantly bias the determination of opening angles. Furthermore, the bias in distance to high-mass YSOs and unknown inclinations could influence the determined opening angles. However, high-resolution observations also show contradictory results regarding opening angles around high-mass YSOs. Multiple modes of high-mass star formation may exist, however, a link between accretion and outflows has been established between different spectral types, making it unlikely that there is more than one mechanism to form high-mass stars. Therefore it is more likely that different evolutionary stages cause the contradiction in observed opening angles. An evolutionary scenario is proposed by Beuther & Shepherd (2005), in which a very early massive protostar, that is not surrounded by a UC HII region, is able to launch a well-collimated jet-like outflow. Eventually winds from the massive protostar launch an additional wider-angled component. Finally, a UC HII region forms and the wide-angled winds begin to dominate over the entire system. An overview of this evolutionary sequence is given in Figure 1.5.

In recent work, Mignon-Risse et al. (2021) perform radiation-magnetohydrodynamic (RMHD) simulations on protostellar outflows around high-mass stars, and they find smaller opening angles than the opening angles observed by Wu et al. (2004) and Beuther et al. (2002), in a range of $20 - 30^\circ$ when magnetic fields dominate, and a range of $30 - 70^\circ$ overall. Their results are in line with CO observations, and they find that their simulated opening angles are larger than those of collimated

jets but smaller than wide-angle outflows.

1.3 Aims of this research

In this project, we study a sample of high- and low-mass star-forming regions, using CO observations from the Atacama Large Millimeter/Submillimeter Array (ALMA), which is especially well suited for research into outflows due to its high spectral and spatial resolution. We aim to determine whether there are differences in the outflow properties of these high- and low-mass YSOs, and to couple these potential differences back to various theories of high- and low-mass star formation.

In this work, we derive several outflow parameters, such as dynamical timescales, which give us information about the timescales of accretion, and outflow opening angles, which are linked to the interactions of protostellar outflows with the surrounding envelope. Parameters such as these provide us with information about the launching mechanism and evolution of protostellar outflows, which are intrinsically linked to theories of star formation.

Our high-mass sample consists of five high-mass protostellar clusters, selected from the ALMA-IMF program (e.g. Motte et al., 2022). Our low-mass sample consists of seven YSOs in the ρ Ophiuchi molecular cloud. We will introduce these samples in Chapter 2. In Chapter 3, we determine rotational temperatures and column densities for all outflows in our fields. In Chapter 4 we determine outflow properties such as radii, dynamical timescales and opening angles. We compare our results with each other and with literature in Chapter 5. Conclusions are found in Chapter 6.

2 . Source sample & observations

2.1 High-mass protoclusters

The five high-mass protoclusters considered in this project were selected from the ALMA-IMF sample (e.g. Motte et al., 2022, , project code 2017.1.01355.L). The ALMA-IMF sample consists of 15 high-mass ($2.5 \cdot 10^3 - 33 \cdot 10^3 M_{\odot}$), nearby (2–5.5 kpc) protoclusters in various evolutionary stages. A wide range of spectral lines have been observed with ALMA, including the CO (2-1) line. For a full description of the observational setup, see Motte et al. (2022).

In this project, we selected a sub-sample of the ALMA-IMF sample consisting of sources with additional higher-J level ALMA CO measurements, which yielded six sources with additional CO (3-2) observations. One protocluster (G327.29) was removed from this sample as the resolution of the available CO (3-2) observation was low (3.673"). The project codes for the CO (3-2) observations are 2018.1.01679.S for G328.25, and 2017.1.00914.S for the other four sources, (PI: Csengeri). The high-mass sample that was left thus consisted of five protoclusters with CO (2-1) and CO (3-2) observations. Observational details of the high-mass sample are described in Table 2.1. Continuum images of the fields are indicated in Figure 2.1.

Motte et al. (2022) determined the evolutionary stage of the protoclusters, based on the 1.3 mm-to-3 mm flux ratio and the free-free emission at the frequency of the H41 α recombination line. According to their classification, three of the high-mass protoclusters we consider (G328.25, G337.92, and G338.93) are 'Young', and two (G008.67 and G351.77) are 'Intermediate'. No 'Evolved' protoclusters were available with additional ALMA CO-line observations, which thus limits our high-mass sample to 'Young' and 'Intermediate' protoclusters. It should be noted that these classifications describe the evolutionary stage of the protocluster, not of any individual YSO in these clusters.

Using the SiO (5-4) line, Towner et al. (2023) identified outflows in the ALMA-IMF sample, which were classified as either 'likely', 'possible', or 'complex or cluster'. SiO is often found to trace high-velocity jets, as the energetic shocks cause silicon to be released from dust grains (e.g. Bally, 2016; Towner et al., 2023). Low-level CO transitions instead trace the lower velocity outflow, which is less compact than the jets traced by SiO. Therefore we do not directly use the SiO outflow identifications in this project. Rather, they were used as visual

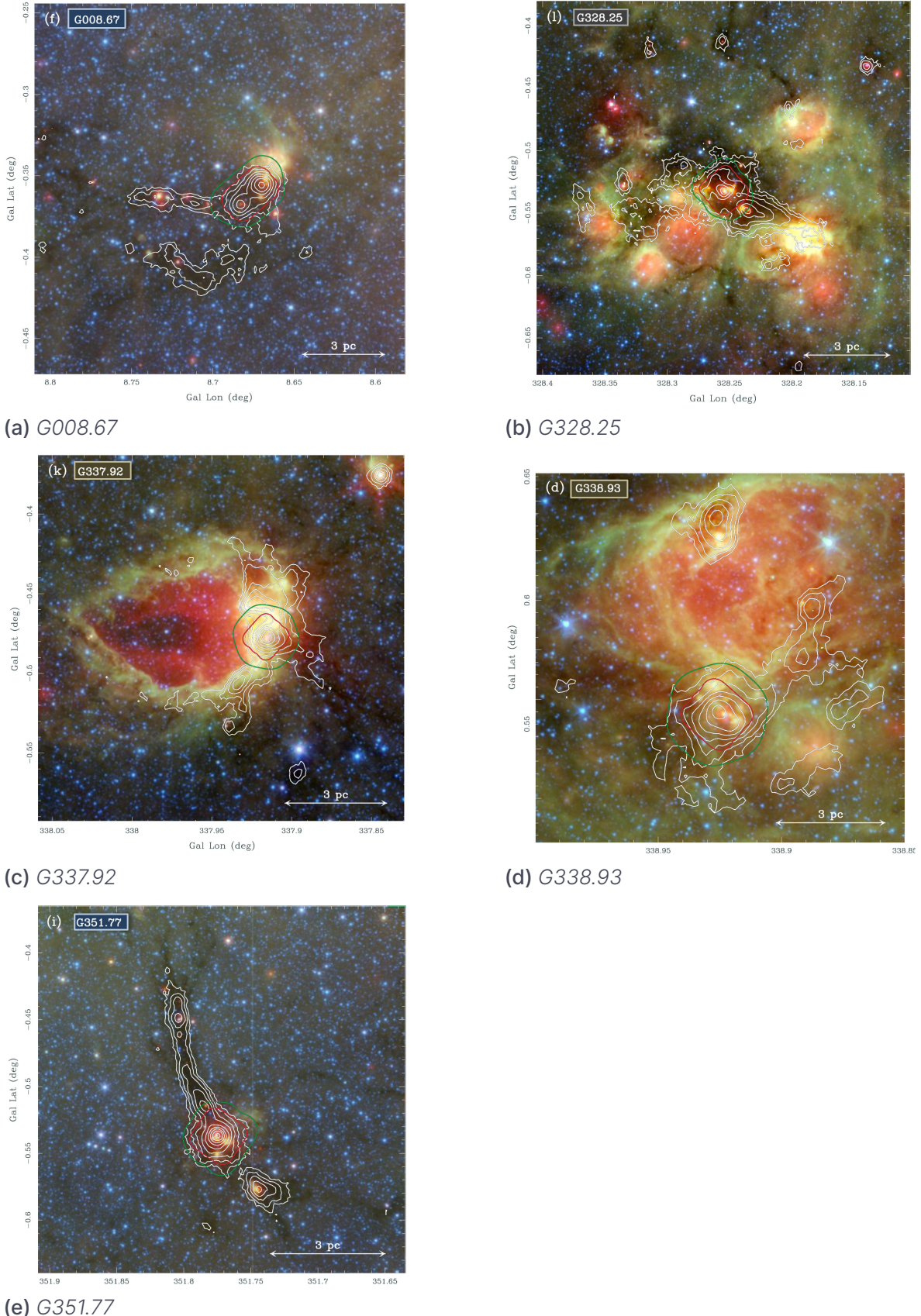


Figure 2.1: Overview of the high-mass protoclusters studied in this work. Shown are Spitzer three-color images, where red = 24 μm , green = 8 μm , and blue = 3.6 μm . Overlaid are ATLASGAL 870 μm contours, logarithmically spaced from 0.45 Jy beam^{-1} to 140 Jy beam^{-1} with a 19.2" beam. The green and red contours outline the primary beam response of the ALMA 12 m array mosaics down to 15% at 3 mm and 1.3 mm, respectively. All images were taken from Motte et al. (2022).

Source	Coordinates [ICRS]	d ⁽¹⁾ [kpc]	Stage ⁽²⁾	Line	Beam ⁽³⁾ [" x "]
G008.67	18:06:21.12 -21:37:16.7	3.4 ± 0.3	I	CO (2-1)	0.72×0.59
				CO (3-2)	4.9×2.7
G328.25	15:57:59.68 -53:58:00.2	2.5 ± 0.5	Y	CO (2-1)	0.62×0.47
				CO (3-2)	0.35×0.29
G337.92	16:41:10.62 -47:08:02.9	2.7 ± 0.7	Y	CO (2-1)	0.61×0.48
				CO (3-2)	0.50×0.47
G338.93	16:40:34.42 -45:41:40.6	3.9 ± 1.0	Y	CO (2-1)	0.56×0.51
				CO (3-2)	0.50×0.46
G351.77	17:26:42.62 -36:09:20.5	2.0 ± 0.7	I	CO (2-1)	0.89×0.67
				CO (3-2)	0.90×0.61

Table 2.1: Overview of the observations of the high-mass sources. 1) Distances to the sun from Csengeri et al. (2017) (G338.93, G008.67, and G328.25), and from Motte et al. (2022) (G351.77 and G337.92). 2) The evolutionary stages of the ALMA-IMF protoclusters, where Y = young and I = intermediate (Motte et al., 2022). 3) The values for the beam that are indicated in bold font are the limiting resolution, and any higher resolution observation is smoothed to this resolution in Chapter 3.

guidance to help confirm the presence and morphology of outflows detected in CO.

2.2 Low-mass protoclusters

For our low-mass sample, we selected seven fields in the ρ Ophiuchi molecular cloud, which is one of the most actively studied low-mass star-forming regions. In Figure 2.2, an image of the cloud is given. We adopted a distance of 140 ± 10 pc to the cluster (Bontemps et al., 2001). Star formation in the ρ Ophiuchus cloud was likely triggered by supernovae, ionization fronts, and winds from the Upper Scorpius OB association, which is located to the west of the Ophiuchus cloud (Preibisch & Zinnecker, 1999; Nutter et al., 2006; Wilking et al., 2008). The seven fields in our low-mass sample have been observed in CO (1-0) (2013.1.00187.S, PI: Schnee), CO (2-1) (2019.1.01792.S, PI:Mardones) and CO (3-2) (2018.1.01634.S, PI: Segura-Cox, for Oph 34, 2022.1.00236.S, PI: Artur de la Villarmois for all other fields). The observational details of the low-mass sample can be found in Table 2.2. Values for the systematic velocity V_{LSR} were taken from van der Marel et al. (2013) when available, and were otherwise defined in this paper using the peak of the CO transitions.

For the low-mass sources, no systematic outflow identifications using SiO were available. However, ρ Ophiuchi is a well-studied molecular cloud, which allows for comparison to literature in outflow identifications. The majority of the low-mass YSOs in this sample have been classified by Van Kempen et al. (2009) as either Stage 1, Stage 2, or as the transition phase Stage 1(T), based on



Figure 2.2: NIRCam image of the ρ Ophiuchi cloud complex, made by the James Webb Space Telescope. The image was taken in F187N = blue, F200W = Light Blue, F335W = Cyan, F444W = Yellow, F470N = Red. Image taken from Pontoppidan (2023).

the classification scheme by (Whitney et al., 2003; Robitaille et al., 2006). The majority of sources in our low-mass sample are Stage 1 embedded YSOs.

Source	Other names	Coordinates [ICRS]	Stage ⁽¹⁾	Transition	Beam ⁽²⁾ ["x"]
Oph 12	WL 12	16:26:44.100 -24:34:48.000	1	CO (1-0)	3.5 x 1.8
				CO (2-1)	1.2 x 0.9
				CO (3-2)	4.5 x 2.6
Oph 26	IRS 43	16:27:26.900 -24:40:50.000	1	CO (1-0)	3.5 x 1.9
				CO (2-1)	1.2 x 0.9
				CO (3-2)	4.6 x 2.6
Oph 27	IRS 44	16:27:27.900 -24:39:33.000	1	CO (1-0)	3.5 x 1.9
				CO (2-1)	1.2 x 0.9
				CO (3-2)	4.6 x 2.6
Oph 29	Elias 33	16:27:30.100 -24:27:43.000	1	CO (1-0)	3.5 x 1.9
				CO (2-1)	1.2 x 0.9
				CO (3-2)	4.6 x 2.6
Oph 31	IRS 51	16:27:39.900 -24:43:13.200	2	CO (1-0)	3.4 x 1.8
				CO (2-1)	1.2 x 0.9
				CO (3-2)	4.6 x 2.6
Oph 34	IRS 63	16:31:35.600 -24:01:29.000	1(T)	CO (1-0)	3.4 x 1.9
				CO (2-1)	1.2 x 0.9
				CO (3-2)	0.7 x 0.6
Oph 39	WLY 2-67	16:32:00.900 -24:56:42.000	-	CO (1-0)	3.4 x 1.9
				CO (2-1)	1.2 x 1.0
				CO (3-2)	4.6 x 2.6

Table 2.2: Overview of the observations of the low-mass sources. 1) Evolutionary stages as defined in Van Kempen et al. (2009) when available, where 1 indicates a stage 1 embedded YSO, 2 indicates a stage 2 disk, and 1(T) is a source in transition from a stage 1 embedded YSO to a stage 2 disk. 2) The values for the beam that are indicated in bold font are the limiting resolution, in Chapter 3 lower resolution observations are smoothed to this resolution.

3. Determination of physical parameters

In this chapter, we aim to derive the temperatures and CO column densities of the outflows in our low- and high-mass samples. The CO column densities allow us to determine the amount of molecular material in the outflows, which could indirectly tell us about their mass. Temperatures are an important factor in understanding the excitation conditions and the chemistry within an outflow. We create maps of these physical parameters for all fields in our low- and high-mass samples using the rotational diagram (RD) method, which we introduce below.

3.1 Methodology

3.1.1 Inspecting the datacubes

From the ALMA archive¹, we downloaded the continuum-subtracted primary beam corrected data cubes that were introduced in Chapter 2, and visually inspected the data quality. All observations were re-framed to the rest-frequency of their respective lines, using the *imreframe* function in *casa*, to ensure that the transition coincides with the systematic velocity of each source. This property allowed us to describe all spectral lines in terms of the relative velocity, rather than in terms of frequency or wavelength.

3.1.2 Smoothing and regridding

We aimed to create maps of T_{rot} and $N_{tot}(\text{CO})$ for each field in our high- and low-mass sample, which requires observations with consistent beams between different transitions. For each field, we smoothed all high-resolution observations to the lowest resolution available for that source, using the *imsmooth* function in *casa*. This function requires parameters for the input image, the major and minor axis of the beam, and the position angle of the beam. It uses Fourier-based convolution to smooth the image to the required beam. The limiting resolutions, to which the higher-resolution images were smoothed, are indicated in bold in Table 2.1 and Table 2.2. We used a Gaussian kernel for the smoothing. As a result of this smoothing, the flux density per beam increases, as the beam becomes larger. An example of the smoothing process is indicated in Figure 3.1, for the

¹<https://almascience.nrao.edu/aq/>

high-mass field G008.67. This field is an extreme example, as the resolution had to be smoothed from $0.72'' \times 0.59''$ to $4.9'' \times 2.7''$. For other sources, the smoothing was less extreme.

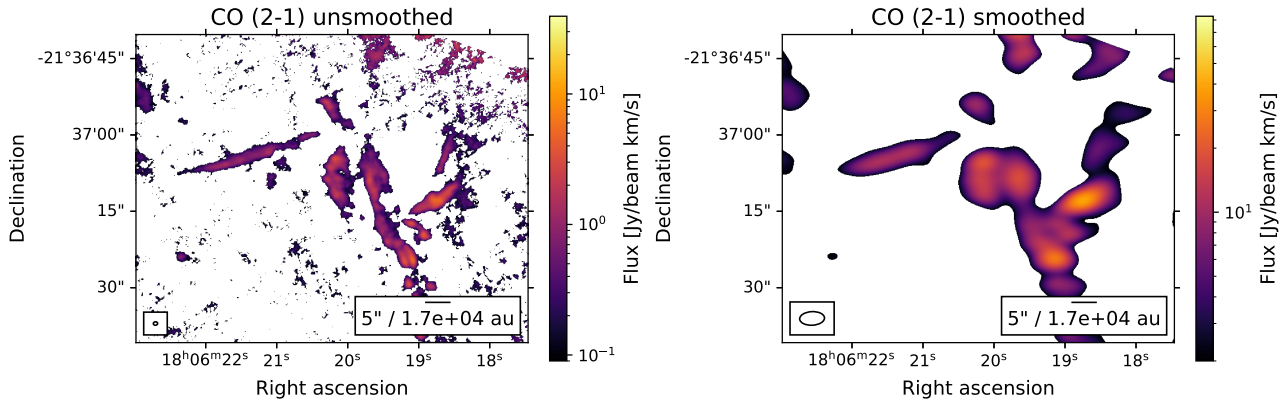


Figure 3.1: CO (2-1) red-shifted integrated emission of the high-mass source G008.67, before and after smoothing to the resolution of the CO (3-2) maps. The maps were both integrated over the same velocity range, as indicated in Table 3.1. This image merely serves as an example of the smoothing process, therefore the clipping was done at arbitrary values. This example is the most extreme smoothing that had to be done.

As a final calibration step, all fields that were smoothed to a lower resolution were regridded to the same pixel grid as the field to which it was smoothed. This step is required to be able to compare pixels with each other. Regridding was allowed since all images were well-sampled. We used the *reproject* Python package (Deil & Ginsburg, 2024) to perform the regridding.

3.1.3 Integrated emission maps

Through visual inspection of the high- and low-mass data cubes, we defined the velocity ranges in which the red- and blue-shifted lobes are detected. Channels near the systemic velocity v_{LSR} were excluded, as here the envelope emission dominates over the outflows. If multiple outflows were detected in a single field, we extended the velocity ranges to that of the outflow with the broadest velocity range. The chosen velocity ranges can be found in Table 3.1. Using these velocity ranges, red- and blue-shifted velocity-integrated maps were constructed of all observations.

3.1.4 Determination of noise levels and clipping

The noise levels of each velocity-integrated emission map were determined by selecting a region without a source in it. Then, the root mean square (rms) was taken over all pixels in this 'empty' region. This number was then convolved with a percentage of the emission, to obtain the noise level σ per pixel. The percentage of the integrated emission that was used is 5% for the CO (1-0) line, and 10% for the CO (2-1) and CO (3-2) line, in line with ALMA systematic uncertainties (Braatz

Source	$v_{LSR}^{(1)}$ [km s $^{-1}$]	$v_{red,min}^{(2)}$ [km s $^{-1}$]	$v_{red,max}^{(2)}$ [km s $^{-1}$]	$V_{blue,min}^{(2)}$ [km s $^{-1}$]	$V_{blue,max}^{(2)}$ [km s $^{-1}$]
Oph 12	4.3 ^(a)	5.1	10.5	-3.2	1.9
Oph 26	3.8 ^(a)	4.3	11.8	-6.3	1.9
Oph 27	3.8 ^(a)	5.9	11.0	-10.0	1.0
Oph 29	4.5 ^(a)	5.0	8.0	-6.0	1.3
Oph 31	2.7 ^(b)	4.5	9.0	-1.0	1.0
Oph 34	2.7 ^(a)	3.0	7.0	-9.0	0.9
Oph 39	3.0 ^(b)	4.5	11.0	-5.0	2.4
G008.67	37.6 ^(c)	48	82	-20	26
G328.25	-43 ^(c)	-35	35	-115	53
G337.92	-40 ^(c)	-31	23	-105	-50
G338.93	-62 ^(c)	-55	0	-130	-73
G351.77	-3 ^(c)	20	90	-120	-13

Table 3.1: The velocity ranges over which the CO emission was integrated to create the integrated blue- and red-shifted CO emission maps. (2) Values for the systematic velocity v_{LSR} , where (a)=van der Marel et al. (2013), (b)=this project, (c)=Wienen et al. (2015). (4) The upper and lower velocity limit over the CO emission was integrated. The spectral resolution for the low-mass sources is 0.1 km s $^{-1}$, and for the high-mass sources 1.3 km s $^{-1}$.

et al., 2021). We then define the signal-to-noise ratio (SNR) as the integrated emission divided by σ for each pixel.

Only pixels with a 3σ detection in two transitions (CO (2-1) and CO (3-2)) for the high-mass sample, or in three transitions (CO (1-0), CO (2-1), and CO (3-2)) for the low-mass sample are included in further calculations. Since emission near the systematic velocity was not included, most of the 3σ emission that is included will be part of an outflow. At this stage, we did not attempt to identify the outflows. We used a different selection limit for the high- and low-mass samples, since we require that pixels are detected in two transitions for the high-mass sample, and in three transitions for the low-mass sample. Outflow identifications at this stage would therefore introduce an unwanted bias between the high- and low-mass samples. Outflow identifications were made in Chapter 4 using unsmoothed CO (2-1) observations, which are more reliable for this purpose.

3.1.5 Local thermodynamic equilibrium

If the ISM is in thermodynamic equilibrium (TE), its macroscopic properties such as temperature T and density n are uniform and do not change over time. These conditions imply there are no flows of energy, and any chemical reaction is in equilibrium. TE does not generally hold, as we observe a wide range of temperatures and densities in the ISM. A weaker condition is local thermodynamic

equilibrium (LTE), in which macroscopic energy flows do exist, but temperature and density vary slowly enough for particles to behave as if they are in TE on small scales. In LTE, all particles have the same internal energy distribution, which depends only on the kinetic temperature T_{kin} . The velocities v of particles in LTE are distributed as a Maxwell distribution

$$f(v) = \sqrt{\frac{2}{3}} \left(\frac{m}{kT}\right)^{\frac{3}{2}} v^2 e^{-mv^2/kT_{kin}}, \quad (3.1)$$

where m is the particle mass and k is the Boltzmann constant. LTE does not generally hold in the ISM, due to the low densities and consequent low collision rates, however Equation 3.1 might still hold outside of LTE if the density is high enough to cause frequent collisions.

The population of energy levels in LTE is thermalized, and is described by the Boltzmann distribution

$$\frac{n_u}{n_l} = \frac{g_u}{g_l} e^{-(E_u - E_l)/kT_{kin}}, \quad (3.2)$$

where n_u and n_l are the number densities in the upper and lower level, respectively, g_u and g_l are the statistical weights of the upper and lower levels, and E_u and E_l are the energies of the upper and lower levels.

The Boltzmann distribution is not generally valid outside of LTE, however, we can still use the Boltzmann distribution to describe the population levels between any two levels using Equation 3.2, by introducing the excitation temperature T_{ex} . T_{ex} is not a physical temperature; it represents the ratio of level populations for a two-level system. In LTE, we retrieve $T_{kin} = T_{ex}$, however outside of LTE, T_{ex} is merely an approximation for T_{kin} .

3.1.6 Radiative transfer

In both TE and LTE, the radiation field follows the Planck function

$$B_\nu(T) = \frac{2h\nu^3}{c^2} \frac{1}{e^{\frac{h\nu}{kT}} - 1}, \quad (3.3)$$

also referred to as the blackbody function. Here, ν is the frequency, h is the Planck constant and c is the speed of light.

The Planck function does not generally hold in the ISM, due to discrete energy sources (e.g. stars), absorption, and emission processes. We can define the brightness temperature T_b as the temperature a blackbody radiator would need to have to reproduce the observed intensity of the region, at a specific frequency.

As light travels through the ISM, light can be absorbed or emitted through interactions with the ISM, which can change the observed specific intensity I_ν . In LTE, if the excitation properties remain constant along the line of sight, we can describe I_ν as

$$I_\nu = I_\nu(0)e^{-\tau_\nu} + B_\nu(T_{kin})(1 - e^{-\tau_\nu}), \quad (3.4)$$

where $I_\nu(0)$ is the initial specific intensity of the source, which gets attenuated as the light traverses the interstellar medium. This attenuation is governed by the

optical depth τ_ν , which is frequency-dependent. As the light traverses from its original source, it gets thermalized with the ISM, until at sufficient optical depth the light is fully described as $B_\nu(T_{kin})$, a blackbody at T_{kin} of the ISM. It should be noted that T_{ex} is frequency dependent. All spectral line dependence is encoded in T_{ex} .

Generally, we state that the ISM is optically thin at a specific frequency ν , if $\tau_\nu \ll 1$. In this case, we can see through the entire cloud, and observe objects behind it. If $\tau_\nu \gg 1$, we state the ISM is optically thick and thus opaque. Any background radiation is now fully thermalized, and we can only see the outer layers of the cloud.

3.1.7 Rotational diagram method

For a given species, if we detect enough transitions with a wide range of upper-level energies E_u , an RD can be constructed. The RD allows us to derive the rotational temperature T_{rot} , which is a proxy for the kinetic temperature T_{kin} of the gas, and the column density N_{tot} of the species (e.g. Turner, 1991; Sutton et al., 1995). Generally, T_{rot} is only defined if more than two levels are involved, otherwise, the RD method derives T_{ex} . In this work, we further refer only to T_{rot} , as a different number of transitions is observed between the low- and high-mass samples.

The RD assumes that all transitions are optically thin ($\tau_\nu < 1$), and a single rotational temperature characterizes all transitions (i.e. the observed object is in LTE). If the system is not in LTE, T_{rot} is not a good proxy for T_{kin} .

In this project, we are allowed to assume that the size of the emission is larger than the size of the beam of the observation, as we study well-resolved protostellar outflows. Therefore, we do not need to correct for beam dilution.

For a single transition, the column density of molecules in the upper energy level, N_u^{thin} , can be derived using the following equation for optically thin lines:

$$N_u^{thin} = \frac{4\pi \int F_\nu dV}{A_{ji} \Omega h c}. \quad (3.5)$$

In this equation, $\int F_\nu dV$ is the velocity-integrated specific flux density, ν is the frequency of the transition, A_{ji} is the Einstein coefficient of the transition, and Ω is the size of the beam.

In LTE, the total column density relates to the upper-level column density as

$$\frac{N_u^{thin}}{g_u} = \frac{N_{tot}}{Q(T_{kin})} e^{-E_u/kT_{kin}}, \quad (3.6)$$

where $Q(T_{kin})$ is the partition function at T_{kin} . Taking the natural logarithm of both sides of Equation 3.6 gives

$$\ln \left(\frac{N_u^{thin}}{g_u} \right) = \left(\frac{-1}{T_{kin}} \right) \left(\frac{E_u}{k} \right) + \ln \left(\frac{N_{tot}}{Q(T_{kin})} \right). \quad (3.7)$$

This equation allows us to derive T_{rot} and N_{tot} . By plotting $\ln\left(\frac{N_u^{thin}}{g_u}\right)$ against $(\frac{E_u}{K})$ and fitting a line ($y = a \cdot x + b$), the slope $a = -\frac{1}{T_{rot}}$, and the intercept $b = \ln\left(\frac{N_{tot}}{Q(T_{rot})}\right)$. The latter gives N_{tot} by interpolating Q at T_{rot} , which was derived from the slope, using values for $Q(T_{kin})$ found in molecular databases such as the CDMS (Müller et al., 2001, 2005; Endres et al., 2016). An example of a rotational diagram is shown in Figure 3.2.

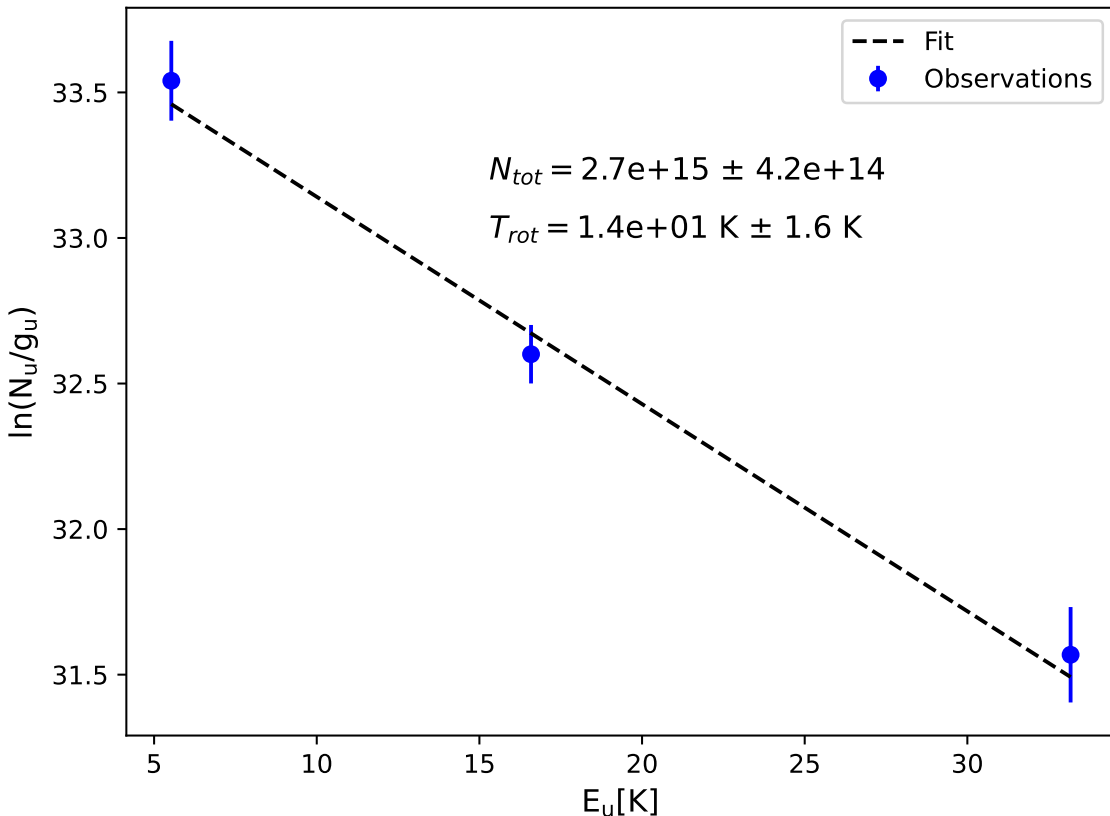


Figure 3.2: Example of a rotational diagram of CO, for a pixel in the blue-shifted lobe of Oph 12, close to the YSO. The derived values for T_{rot} and N_{tot} are indicated.

The RD method requires a minimum of two observed transitions, although it is preferable to perform the analysis on more than two transitions. If the assumption that all lines are optically thin fails, if the observed object is not in LTE, or if it consists of multiple gas components with different temperatures, a well-sampled rotational diagram will not show a straight line. When only observing two transitions, this nonlinearity cannot be detected, and one cannot determine when the underlying assumptions fail. The RD method should be used with care, and methods that do not assume LTE or optically thin transitions will be more reliable if enough transitions are detected. An example of such a method is modeling the gas using a non-LTE radiative transfer code, such as RADEX. This

method does not assume LTE and is able to constrain optically thick transitions. However, collisional coefficients of the species would need to be available in order to perform such an analysis.

3.1.8 T_{rot} and $N_{tot}(\text{CO})$ determination

For each 3σ pixel in our high- and low-mass fields, we determined the upper-level column density for all available transitions, using Equation 3.5. We then construct the RD for each pixel, using the upper-level energies retrieved from CDMS (Müller et al., 2001, 2005; Endres et al., 2016).

For our low-mass sample, we use least squares fitting to fit a line to the RD, and from the slope, we immediately retrieved T_{rot} for each pixel. We interpolated Q to retrieve $Q(T_{rot})$, which allowed us to determine $N_{tot}(\text{CO})$ from the intercept. Uncertainties were estimated from the covariance matrix. Any uncertainties in $Q(T_{rot})$ were neglected.

For our high-mass sample, the same method was used, although since there are only two detected transitions, uncertainties could not be estimated through the covariance matrix, and standard propagation of errors was used instead.

3.2 Results

As an example, the maps of T_{rot} and N_{rot} of G338.93 are indicated in Figure 3.3. For the remaining sources, the maps are indicated in Appendix A.2. In these maps, we indicate for the high-mass sources the continuum cores as traced by the DCN (3-2) transition (Cunningham et al., 2023), as well as the hot cores traced by CH₃OCHO (methyl formate, Bonfand et al., 2024). For the low-mass sample, we indicate the positions of sources in the Two Micron All Sky Survey (2MASS) Point Source Catalog (PSC, Skrutskie et al., 2006), that were identified as YSO in literature (Bontemps et al., 2001; Wilking et al., 2008; Pattle & Ward-Thompson, 2015; Connelley & Greene, 2010).

For each field, we determined the mean T_{rot} and $N_{tot}(\text{CO})$. We indicate these mean values below, however, care should be taken in interpreting these values as the temperature can vary significantly over a single field. We refer back to Appendix A.2 for a better overview of the ranges of values of T_{rot} and $N_{tot}(\text{CO})$ that were determined. In Section 3.2.1 and Section 3.2.2, we go into more depth about the ranges of temperatures that were found, and whether the underlying assumptions made for the RD method hold.

The mean rotational temperature over the low-mass fields ranges between 8.3 K and 21.8 K, with a weighted mean of 11.3 ± 0.6 K. For our high-mass sample, we find the mean temperature per field to range between 22.6 K and 58.9 K, with a weighted mean of 28 ± 6 K. If all assumptions of the RD method hold, we would find that outflows driven by high-mass protostars have higher rotational temperatures compared to outflows driven by low-mass protostars.

The mean CO column density over the low-mass fields ranges between $8 \cdot 10^{14} \text{ cm}^{-2}$ and $1.3 \cdot 10^{16} \text{ cm}^{-2}$, with a weighted mean of $2.0 \cdot 10^{15} \pm 0.2 \cdot$

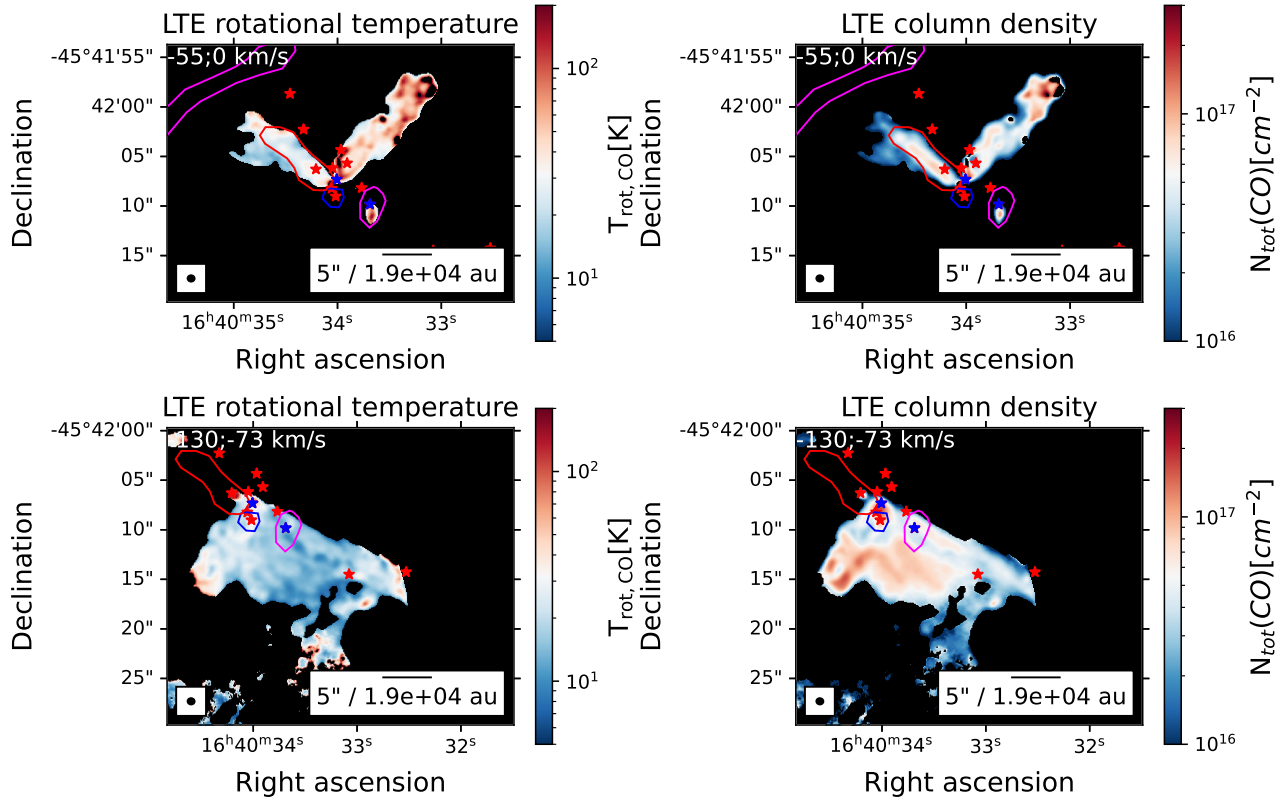


Figure 3.3: T_{rot} and $N_{\text{tot}}(\text{CO})$ maps for G338.93. The upper plots indicate the red-shifted lobes, integrated between -55 and 0 km s^{-1} . The lower plots indicate the blue-shifted lobes, integrated between -130 and -73 km s^{-1} . The beam size is indicated in the bottom left of each figure, a scale bar is indicated in the bottom right of each figure. SiO-identified outflows are indicated in red and blue for red-shifted and blue-shifted outflows, bipolar SiO-identified outflows are indicated in pink (Towner et al., 2023). Hot cores (Bonfand et al., 2024) are indicated as blue stars, while continuum cores (Cunningham et al., 2023) are indicated as red stars. Pixels are masked out if $T_{\text{rot}} < 1 \text{ K}$ or $T_{\text{rot}} > 200 \text{ K}$. We suspect that the majority of pixels is optically thick in the CO (2-1) line, therefore we treat derived temperatures as upper limits and derived column densities as lower limits.

10^{15} cm^{-2} . The mean column density over the high-mass fields ranges between $6.3 \cdot 10^{15} \text{ cm}^{-2}$ and $2.6 \cdot 10^{17} \text{ cm}^{-2}$, with a weighted mean of $9.0 \cdot 10^{15} \pm 0.6 \cdot 10^{15} \text{ cm}^{-2}$. Therefore under RD assumptions, we find that outflows driven by low-mass protostars have lower CO column densities compared to outflows driven by high-mass protostars.

3.2.1 Optically thick transitions in high-mass fields

Since our high-mass sample is only detected in two transitions, it is important to determine whether our initial assumptions hold. Therefore, we determined for all fields whether T_{rot} is well-behaved. We found that multiple pixels return a negative value for T_{rot} , which is a clear indicator that the CO (2-1) line is optically thick in those pixels, and the RD method fails. Any of these pixels were masked

out. Furthermore, there were many pixels with $T_{rot} >> 200\text{K}$, even upwards of $\sim 10^4\text{K}$, while a generous estimate for the maximum expected T_{rot} would be $\sim 100\text{K}$ (McKee & Tan, 2003). These extreme values further indicated that for many pixels, the CO (2-1) line is optically thick and T_{rot} is overestimated. We thus mask out any pixel with $T_{rot} > 200\text{K}$, and do consider either T_{rot} or $N_{tot}(\text{CO})$ to be valid for this pixel.

Even when masking out these unrealistic values, we could not determine whether pixels with ‘well-behaved’ temperatures are reliable, or if they were affected by optical thickness or non-LTE circumstances as well. Therefore, we assumed all values for temperature estimates in the high-mass fields are upper limits. As a consequence, column densities are likely underestimated, therefore we treated them as lower limits.

For G328.25 and G338.93, many pixels in the middle of outflows are masked out due to negative or extreme values of T_{rot} , while for the other high-mass sources (G008.67, G337.92, and G351.77), the masked out pixels are either near the YSO or on the furthest parts of the outflows, and in total, fewer pixels are masked out. We therefore suspect that for the latter sources, the problem is less significant, and the derived values are more reliable than the former sources. In Figure 3.3 multiple masked-out regions can be seen in the red-shifted lobe.

We attempted to constrain the temperatures and column densities of the high-mass fields more accurately by using the non-LTE modeling software *RADEX*, but we were unable to achieve a reliable fit, due to the limited amount of transitions available. More details on this process can be found in Appendix A.1.

3.2.2 Non-LTE or multiple component emission in low-mass fields

For the low-mass sources three transitions were detected, so optically thick transitions were more easily flagged. We found no pixels with negative temperatures, or temperatures higher than $\sim 50\text{ K}$. Furthermore, for all but one pixel the CO (1-0) transition laid at higher $\ln\left(\frac{N_{tot}(\text{CO})}{Q(T_{kin})}\right)$ than the CO (2-1) transition in the RD. Therefore, we assumed that the low-mass fields were not generally affected by optically thick transitions.

The only pixel in all of the low-mass fields that was deemed unreliable is a pixel in the red-shifted maps of Oph 27. The RD of this pixel shows the CO (1-0) transitions to be lower than the CO (2-1) transition, indicating that the pixel is optically thick in the former transition. van der Marel et al. (2013) found that this is the only source in their sample to be optically thick as well, further away from the source velocity. Their findings are based on the CO (3-2) and ^{18}CO (3 – 2) transitions. They found that these optically thick regions only occur in the blue-shifted lobes, while the optically thick pixel we identified is in the red-shifted lobe. Therefore, the derived T_{rot} and $N_{tot}(\text{CO})$ values for Oph 27 should be interpreted carefully.

Since we only detected a single pixel that is visibly optically thick in the CO (1-0) transition, and the RD is well-sampled for the low-mass sample, we did not consider the temperatures to be upper limits and column densities to be lower

limits. There could be pixels in this field or another low-mass field with optically thick transitions that we did not identify, however, any overestimation of the rotational temperature will be mitigated by the other transitions that are available. Therefore we suspected that the estimated rotational temperatures were reliable, and we did not treat them as upper-limits.

We manually inspected the RD for certain pixels close to and far from the YSO, to ensure that the RD method is reliable for these fields. We found that there is a slight deviation in the RD for a minority of the pixels, across various sources. An example can be found in Figure 3.4. Such a deviation in the RD could be explained by the sources not being in LTE. Another explanation might be that there are multiple regions with different temperatures in the same beam. Therefore, the low-mass temperature and column density maps should be interpreted with care as well.

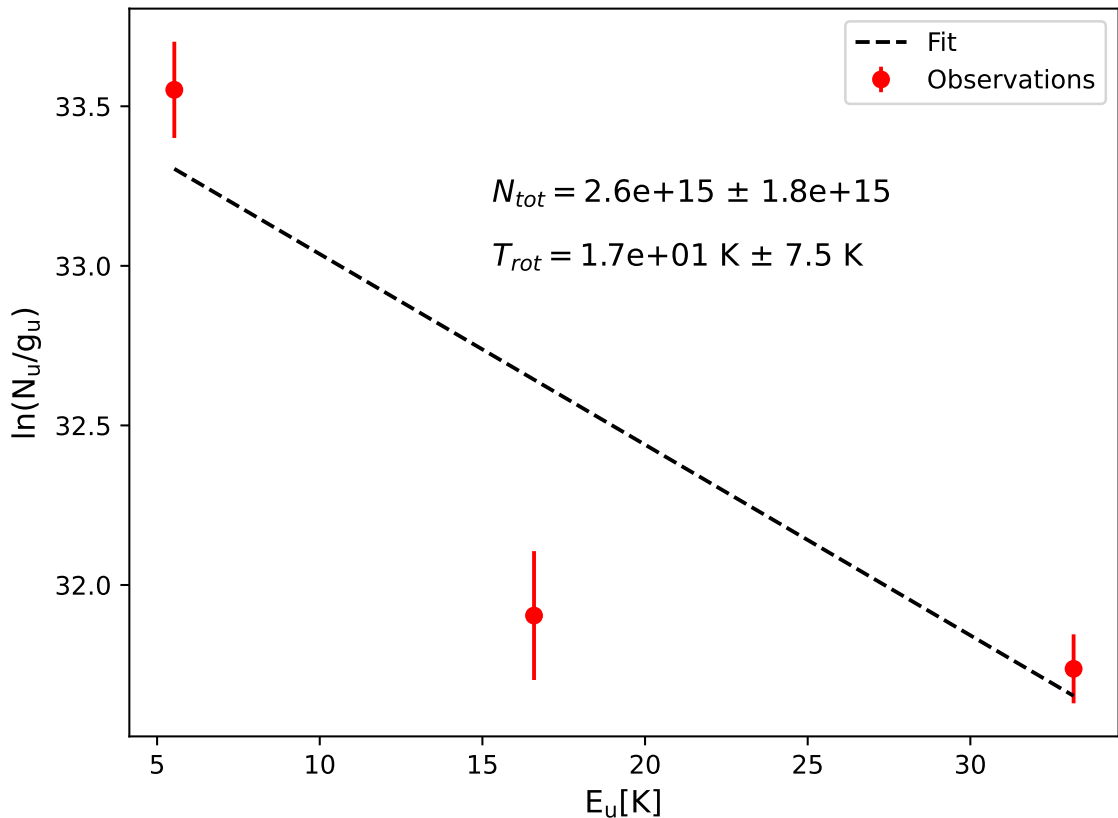


Figure 3.4: Example of the RD of a pixel in the red-shifted lobe in Oph 12. This RD displays a deviation, either caused by the gas not being in LTE, or there being multiple emitting regions with different temperatures in the same beam. The derived values for T_{rot} and $N_{tot}(\text{CO})$ are indicated.

4. Morphology and outflow properties

In this chapter, we study the morphology of the outflows in our low- and high-mass samples and determine properties such as radii, velocities, dynamical timescales, and opening angles. These physical properties give us information about the size of an outflow, the energy within an outflow, the timescales of accretion, and information about how outflows interact with their envelopes. Understanding these properties helps us identify differences in low- and high-mass star formation.

4.1 Methodology

4.1.1 Integrated CO (2-1) maps

To determine the morphological parameters of the outflows in our samples, we constructed integrated blue- and red-shifted CO (2-1) maps. This transition is the lowest upper-level energy that is detected for both samples. Since we inspected the morphology of the sources using only the CO (2-1) line, no smoothing was done on these maps. The resolution of the maps can be found in Table 2.1 and Table 2.2. The maps were integrated over the same velocity ranges as were used in Chapter 3, which are indicated in Table 3.1. The maps can be found in Figure 4.3, Figure 4.4, and Figure 4.5. An in-depth description of each field can be found in Section 4.2.3.

4.1.2 Outflow classifications

From the CO (2-1) maps, we identified red-shifted and blue-shifted outflows by eye, which we then classified as either ‘Likely’ or ‘Possible’. ‘Likely’ lobes are isolated, clearly connected to a YSO, with a red- or blue-shifted counterpart. For the high-mass sample, we also visually compared the CO outflows to outflow identifications using SiO (Towner et al., 2023), to further confirm outflow identifications. ‘Likely’ lobes are included in further calculations. ‘Possible’ lobes are lobes that might be overlapping with other lobes, or lobes that are disconnected from a protostar, and were not included in any further calculations in this chapter. For all ‘Likely’ lobes, we determined the outflow radius R , the outer velocity v_{out} , the dynamical age t_{dyn} , and the opening angle α .

4.1.3 Radius determination

We determined the radius of the 25 'Likely' lobes, which we eventually use to determine the dynamical ages of the outflows. We identified the outflow axis originating from the central YSO, by following the brightest contours of the integrated CO (2-1) maps. We then selected the furthest point on this axis where the integrated emission is still higher than 3σ . The length of this axis is then defined as the radius R of the outflow. The uncertainty on R was found by convolving the major axis of the beam with 10% of R .

Since R was determined by following the brightest parts of the lobe, the axis did not always extend to the furthest point of the lobe, for example, if there was a cavity in the outflow or if the lobe was severely asymmetric. Furthermore, the true value of R is inclination-dependent, which can usually not be determined accurately. For the purposes of this project, we were allowed to use R to compare the relative sizes between low- and high-mass sources, but care should be taken when interpreting it as a physical parameter.

If the position of the YSO aligns with the brightest part of the lobe, the direction of the axis could not be determined accurately. In such a case, the outflow axis was chosen to extend to the furthest point of the lobe.

Due to the intrinsic astrometric inaccuracy of 2MASS, the starting point of the radii for some low-mass sources was not always chosen as the exact location of the YSO, if the reported YSO position appears offset from the outflow axis. 2MASS has a positional accuracy of 0.5" (Skrutskie et al., 2006), therefore we ensured that the offset between the YSO and the new starting point of the axis was no larger than this value.

4.1.4 Outer velocity determination

We determined v_{out} for each lobe by determining the furthest velocity bin away from the systematic velocity v_{LSR} where there is still a 3σ detection. In the high-mass fields, multiple outflows are often present in a single field. For each red- and blue-shifted lobe, v_{out} was determined separately. We then found $\Delta v = |v_{out} - v_{LSR}|$, which we eventually use to determine the dynamical age t_{dyn} . The uncertainty in Δv is found by convolving the spectral resolution of the CO (2-1) observations (1.3 km s^{-1} for the high-mass fields, 0.08 km s^{-1} for the low-mass fields) with 5% of Δv .

In literature (e.g. van der Marel et al., 2013), v_{out} is defined as the last velocity bin where the emission is still above 1σ . However, since we determine the outflow radii R using a 3σ limit, we decided to determine v_{out} using a 3σ limit as well.

v_{out} is usually not a well-constrained parameter, and it should be interpreted with care. It depends significantly on the inclination, which is often unknown. Furthermore, outflows often have multiple epochs of activity (e.g. Arce et al., 2007; Plunkett et al., 2015), often follow a bow-shock (e.g. Cabrit et al., 1997) which includes forward and transverse motion, and outflows can show features such as cavities. Therefore, the measured v_{out} along the line of sight is not necessarily representative of the real velocity of the outflow. In this project, we

used v_{out} to compare our low- and high-mass sources and to determine t_{dyn} , however it should not be interpreted as the "true" velocity.

4.1.5 Dynamical age determination

We determined the dynamical age from $t_{dyn,obs} = \frac{R}{\Delta v}$, which was not corrected for inclination. An outflow in the plane of the sky (roughly $i = 90^\circ$) will have an overestimated dynamical age, while a pole-on source (roughly $i = 0^\circ$) will have an underestimated dynamical age. The corrected dynamical age is $t_{dyn,true} = \frac{t_{dyn,obs}}{\tan(i)}$. In Chapter 5, we compare both the uncorrected and corrected dynamical ages between the high- and low-mass samples.

The calculation for t_{dyn} ignores any episodic activity and depends on all the caveats in R and v_{out} that were mentioned above. Therefore, t_{dyn} is rarely a true tracer of the age of the outflow, and should not be interpreted as such. We can however use it to compare the relative timescale of dynamic activity between outflows driven by low- and high-mass protostars. Downes & Cabrit (2007) have developed a more accurate method to determine t_{dyn} , using the half-width of the outflow lobe, however this method might not apply to Class I sources or high-mass sources, since this method was only tested on low-mass Class 0 sources.

4.1.6 Opening angle determination

We determined the outflow angle α of each 'likely' outflow in our sample, using the method described by Dunham et al. (2024), first developed by Offner et al. (2011). An example of this method is given in Figure 4.1, for the high-mass field G328.25.

For each outflow, we masked out any pixel of the integrated CO (2-1) maps below 3σ , and any pixel not part of the outflow. In some fields, we also masked out pixels that are part of the outflow, for example, if the outflow was significantly asymmetric due to low-SNR lobes. In Figure 4.1, the included pixels are indicated in the shaded blue and red regions.

For all included pixels, we determined the angle between that pixel and the axis used to determine the outflow radius. Unlike Dunham et al. (2024), we treated the red-shifted and blue-shifted outflow separately, since the red and blue axes can be significantly offset. We plotted this angle distribution (as can be seen on the right-hand side of Figure 4.1) and use non-linear least-squares fitting to fit a Gaussian distribution to it.

In Figure 4.2, an example is given of a source where parts of the angle distribution were masked out before fitting the Gaussian distribution, as justified by Dunham et al. (2024). Since there is a cavity in the red-shifted lobe, only the wings of the distribution properly represent the opening angle, and the center of the distribution can be masked out.

The full width at quarter maximum (FWQM) of the Gaussian fit provides us with a measure for the opening angle, which is indicated in Figure 4.1 as solid lines, relative to the fitted axis. The method used to determine the opening angle

is more systematic than determining the opening angles 'by eye', however, it is not always a good representation of the 'true' opening angle, if such a parameter can even be defined. The opening angle is strongly dependent on inclination, which is not available for the majority of our sources. Therefore we are likely overestimating the opening angle of our sources.

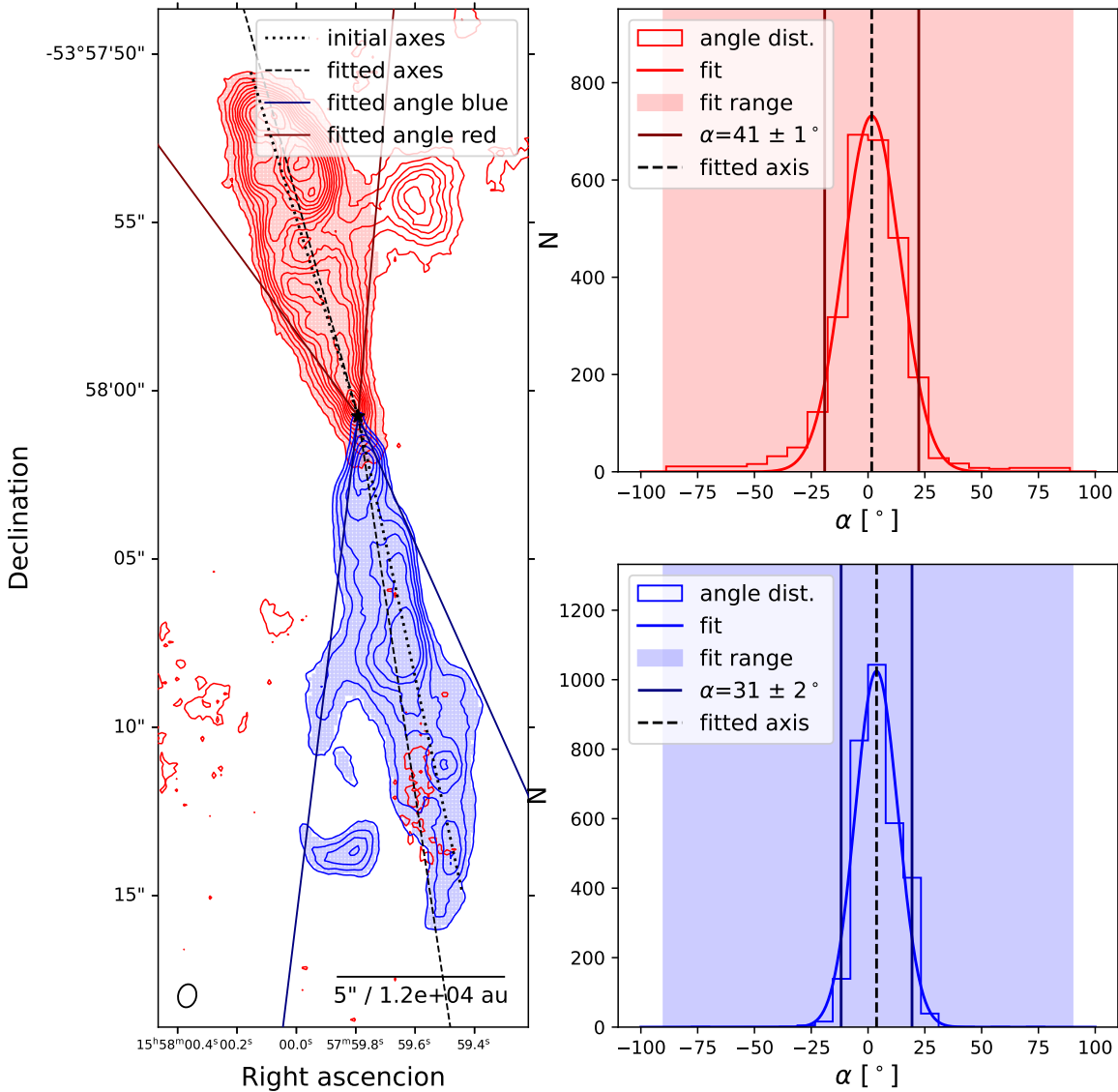


Figure 4.1: Left: Integrated blue- and red-shifted CO (2-1) emission showing the G328.25 outflow, integrated over the velocity interval reported in Table 3.1. The red contour levels start at 3σ , and are then at intervals of 5σ . The blue contour levels are at $(3, 4, 5, 6, 7, 8)\sigma$, and then at intervals of 5σ . The initial axes, indicated as dotted lines, are the axes used to determine the radii of the outflow. The pixels in the shaded areas are included in determining the opening angles. The fitted opening angles are indicated as solid lines, relative to the fitted axis indicated as a dashed line. The position of the YSO is indicated as a black star. Right: The histograms of the angle distributions used to determine the opening angles of the outflow, to which a Gaussian distribution is fitted. For this source, no angle distribution bins were excluded, which is indicated in the shaded region. The fitted axes are indicated as dashed lines, and the fitted opening angles are indicated as solid lines.

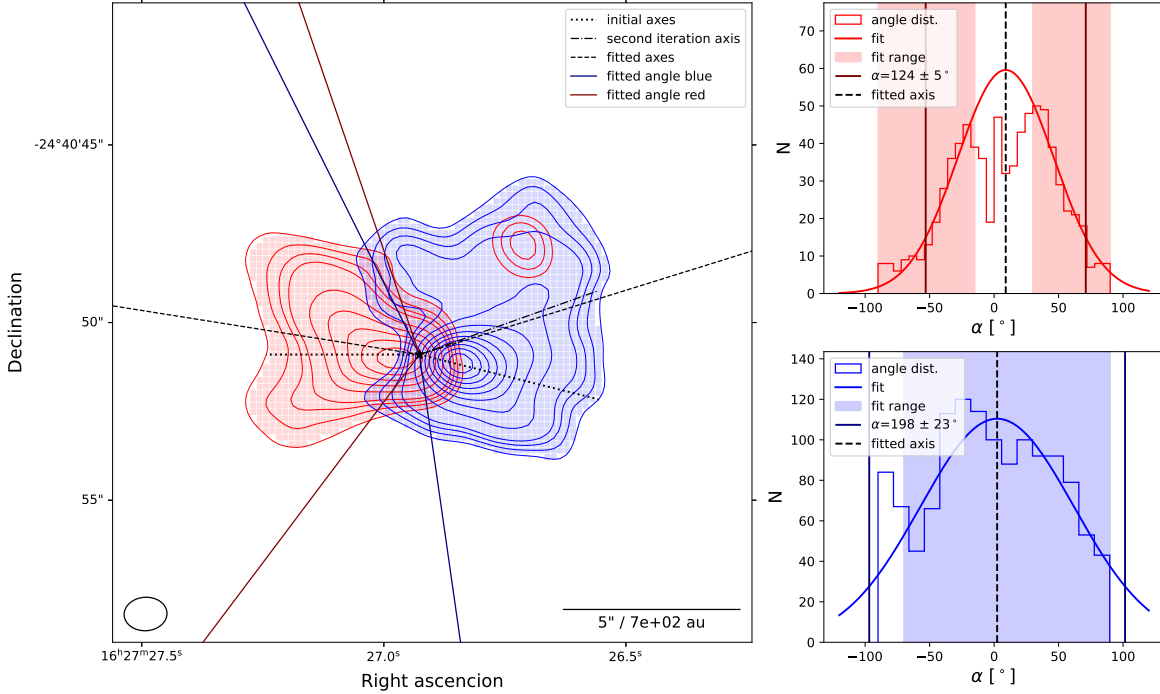


Figure 4.2: Left: Integrated blue- and red-shifted CO (2-1) emission showing the Oph 26 outflow, integrated over the velocity interval reported in Table 3.1. The contour levels are at 3σ , 4σ , 5σ , 6σ , and then at intervals of 3σ . The initial axes, indicated as dotted lines, are the axes used to determine the radii of the outflow. The pixels in the shaded areas are included in determining the opening angles. The fitted opening angles are indicated as solid lines, relative to the fitted axis indicated as a dashed line. The position of the YSO is indicated as a black star. The red lobe is an example of a source where some bins in the angle distribution had to be masked out due to the presence of a cavity. For the red lobe, some bins had to be masked out due to the asymmetry of the source. Right: The histograms of the angle distributions used to determine the opening angles of the outflow, to which a Gaussian distribution is fitted. The shaded regions indicate which bins were included in the fitting. For this source, some bins in the red-shifted distribution are removed due to the cavity in the lobe. The fitted axes are indicated as dashed lines, and the fitted opening angles are indicated as solid lines.

4.2 Results

In Table 4.1, we summarize all parameters that were calculated in this chapter. We also indicate the inclination when available (van der Marel et al., 2013). In Section 4.2.3, we justify for each source which outflows were identified and their classification, and any further source-specific detail about the determination of the outflow parameters.

Outflow ⁽¹⁾	$v_{sys}^{(2)}$ [km/s]	$i^{(3)}$ [°]	$R^{(4)}$ [$\times 10^4$ au]	$v_{out}^{(5)}$ [km/s]	Red			Blue				
					$t_{dyn}^{(6)}$ [$\times 10^2$ yr]	C ⁽⁷⁾	$\alpha^{(8)}$ [°]	$R^{(4)}$ [$\times 10^4$ au]	$v_{out}^{(5)}$ [km/s]	$t_{dyn}^{(6)}$ [$\times 10^2$ yr]		
Oph 12	4.3 ^(a)	30	0.10 ± 0.02	11.4	6 ± 1	L	91 ± 7	0.09 ± 0.02	-2.7	6 ± 1	L	96 ± 9
Oph 26	3.8 ^(a)	10	0.06 ± 0.02	12.5	3 ± 1	L	124 ± 5	0.07 ± 0.02	-6.8	3.3 ± 0.8	L	198 ± 23
Oph 27	3.8 ^(a)	30	0.03 ± 0.02	13.3	1.3 ± 0.9	L	-	0.05 ± 0.02	-11.4	1.7 ± 0.6	L	167 ± 12
Oph 29	4.5 ^(a)	70	0.08 ± 0.02	7.6	13 ± 3	L	137 ± 15	-	-6.8	-	P	-
Oph 31	2.7 ^(b)	-	0.08 ± 0.02	9.0	6 ± 1	L	209 ± 14	-	-1.4	-	P	-
Oph 34	2.7 ^(a)	30	0.03 ± 0.02	5.1	6 ± 3	L	181 ± 21	0.08 ± 0.02	-9.2	3.3 ± 0.8	L	158 ± 7
Oph 39	3 ^(b)	-	0.04 ± 0.02	10.9	2 ± 1	L	123 ± 10	0.10 ± 0.02	-4.8	6 ± 1	L	86 ± 5
<hr/>												
G008.67 _A	37.6 ^(c)	-	3.3 ± 0.4	76.5	40 ± 6	L	35 ± 12	5.0 ± 0.6	-26.4	37 ± 5	L	25 ± 2
G008.67 _B			1.9 ± 0.4	74.0	25 ± 6	L	39 ± 4	5.0 ± 0.6	-16.2	44 ± 6	L	57 ± 4
G008.67 _C			-	56.2	-	P	-	-	15.5	-	P	-
G008.67 _D			-	52.4	-	P	-	-	15.5	-	P	-
G328.25	-43 ^(c)	-	2.7 ± 0.3	26.4	18 ± 2	L	41 ± 1	3.5 ± 0.4	-117.1	22 ± 3	L	31 ± 2
G337.92	-40 ^(c)	-	4.3 ± 0.5	43.6	25 ± 3	L	50 ± 3	4.4 ± 0.5	-126.6	24 ± 3	L	61 ± 3
G338.93 _A	-62 ^(c)	-	4.4 ± 0.5	-11.4	41 ± 5	L	43 ± 3	-	-111.7	-	P	-
G338.93 _B			5.6 ± 0.6	28.0	29 ± 4	L	33 ± 1	-	-125.7	-	P	-
G338.93 _C			0.5 ± 0.3	-26.6	7 ± 4	L	-	-	-	-	P	-
G351.77 _A	-3 ^(c)	-	3.3 ± 0.4	126.1	12 ± 2	L	44 ± 4	-	-196.5	-	P	-
G351.77 _B			1.6 ± 0.3	102.0	7 ± 1	L	55 ± 4	-	-60.6	-	P	-

Table 4.1: The morphological parameters for all outflows in this project. (1) The name of the protostar. (2) The V_{LSR} values, where (a)=van der Marel et al. (2013), (b)=this project, (c)=Wienen et al. (2015). (3) Outflow inclinations where available, from van der Marel et al. (2013). (4) The outflow radii R in units of 10^4 au. (5) The outer velocities v_{out} . (6) The dynamical ages t_{dyn} , uncorrected for inclination. (7) The confidence in the outflow identification, where L = likely, P = possible. (8) Opening angles α uncorrected for inclination. Angles that could not be fit reliably are not indicated.

4.2.1 Radii, velocities, and dynamical timescales

The radii of the lobes in the low-mass sample are in a range between $3 \cdot 10^2$ au and 10^3 au, with a weighted mean value of $6.5 \cdot 10^2 \pm 5 \cdot 10^1$ au. The high-mass sample has a range of radii between $5 \cdot 10^3$ au and $5.5 \cdot 10^4$ au, with a weighted mean of $2.7 \cdot 10^4 \pm 1 \cdot 10^3$ au. The outflows in the high-mass sample are thus roughly a factor ~ 50 larger than the outflows in the low-mass sample.

The range of values we find for Δv in our low-mass sample is between 2.4 and 15.2 km s^{-1} , with a weighted mean of $4.9 \pm 0.1 \text{ km s}^{-1}$. For our high-mass sample, we find values of Δv between 35 and 129 km s^{-1} , with a weighted mean of $55 \pm 1 \text{ km s}^{-1}$. Therefore, we find that the high-mass sample has typical velocities ~ 10 times larger than the low-mass velocities.

We find dynamical timescales, uncorrected for inclination, in a range of $1.3 \cdot 10^2$ and $1.3 \cdot 10^3$ yr for the low-mass sample, with a weighted mean of $3.2 \cdot 10^2 \pm 0.2 \cdot 10^2$ yr. The high-mass sample has dynamical timescales in the range of $6.8 \cdot 10^2$ yr and $4.4 \cdot 10^3$ yr, with a weighted mean of $1.57 \cdot 10^3 \pm 0.07 \cdot 10^3$ yr. The outflows in the high-mass sample thus have typical uncorrected dynamic timescales ~ 5

times longer than the outflows in the low-mass sample.

4.2.2 Opening angles

Two examples of the opening angle determination method can be found in Figure 4.1 and Figure 4.2. For all other outflows in our high- and low-mass sample, we plot the determination of the opening angle in Appendix A.3.

For the low-mass sample, we find an average opening angle of $119 \pm 2^\circ$, while for the high-mass sample, we find an average opening angle of $38.5 \pm 0.6^\circ$. The outflows in the low-mass sample are thus much less collimated than the outflows in the high-mass sample.

We experienced a significant difference in the ‘ease of fitting’ between the high- and low-mass samples. The high-mass sources are generally more conical, and have smaller opening angles, so little manual masking had to be done on these sources. The low-mass sources are smaller and often have wider opening angles, which makes fitting the opening angle more difficult, and the method less reliable. Furthermore, there are often fewer pixels available to use for the fit of the low-mass sample, further complicating the determination of the opening angle for low-mass sources. In one case (the red-shifted lobe of Oph 27) no reliable fit could be achieved, therefore the value of α was not determined.

4.2.3 Details of individual outflows

In this section, we will describe for each field in our sample which outflows we were able to identify, their classification as either ‘Likely’ or ‘Possible’, and any comment on the determination of R , v_{out} , and t_{dyn} . We further comment on the determination of α and justify any masking done on the lobes and the angle distribution. Detailed figures of the opening angle determination can be found in appendix A.3 for each source. We do not indicate the derived outflow parameters for each lobe below, and instead refer to Table 4.1 for all derived values.

Oph 12

The integrated blue- and red-shifted CO (2-1) maps of Oph 12 are indicated in Figure 4.3a. We identify a bipolar outflow along the northeast-southwest direction, which we label ‘Likely’. van der Marel et al. (2013) also identify an outflow around this source, although they identified a northwest-southeast direction. This suggests that we might be identifying a different outflow or significantly different regions of the same outflow, compared to their work. This discrepancy might be caused by them observing at a higher J-level (CO (3-2)) and at a lower resolution (15’’). Therefore they might detect extended emission that gets resolved out in our observations, while our data is sensitive to more compact emission, possibly influencing which outflows are identified.

Oph 12 has an inclination of 30° (estimated by van der Marel et al. 2013), which explains why the red and blue outflows overlap significantly. It might be possible that this inclination is associated with another outflow, and not with the outflow we identify. Since we report on the uncorrected outflow parameters in Table 4.1,

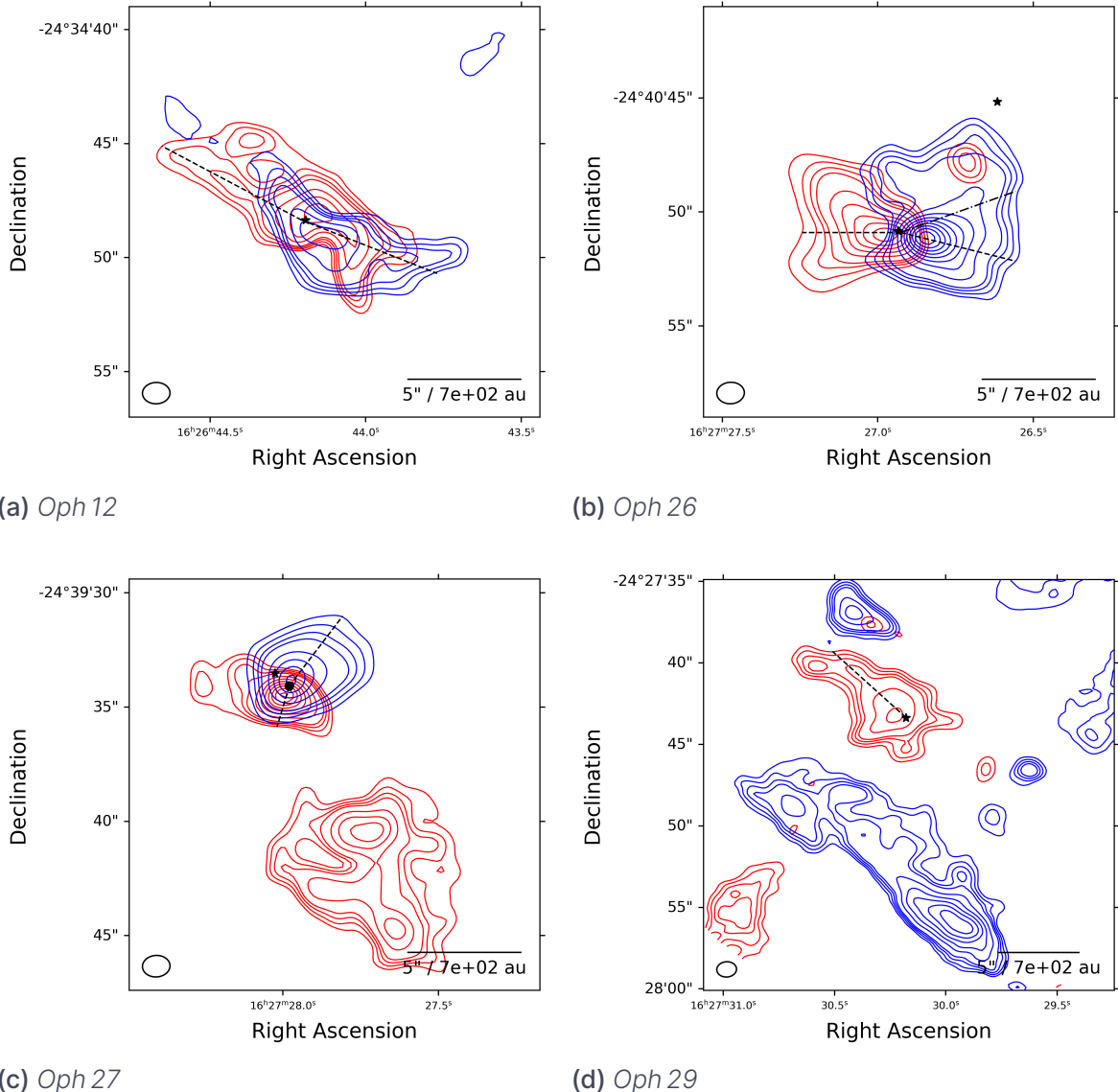


Figure 4.3: Integrated blue- and red-shifted CO (2-1) maps of sources in our low-mass sample. No smoothing was done on these maps. The velocity ranges used to create the maps are indicated in Table 3.1. The contour levels are at 3σ , 4σ , 5σ , 6σ , and then at intervals of 3σ . The positions of the YSOs are indicated as black stars, if the position of the outflow axis is manually altered from the position of the YSO, the new position is indicated as a black circle. Oph 26: The axis used for the second iteration of the angle determination is indicated as a dashed-dotted line.

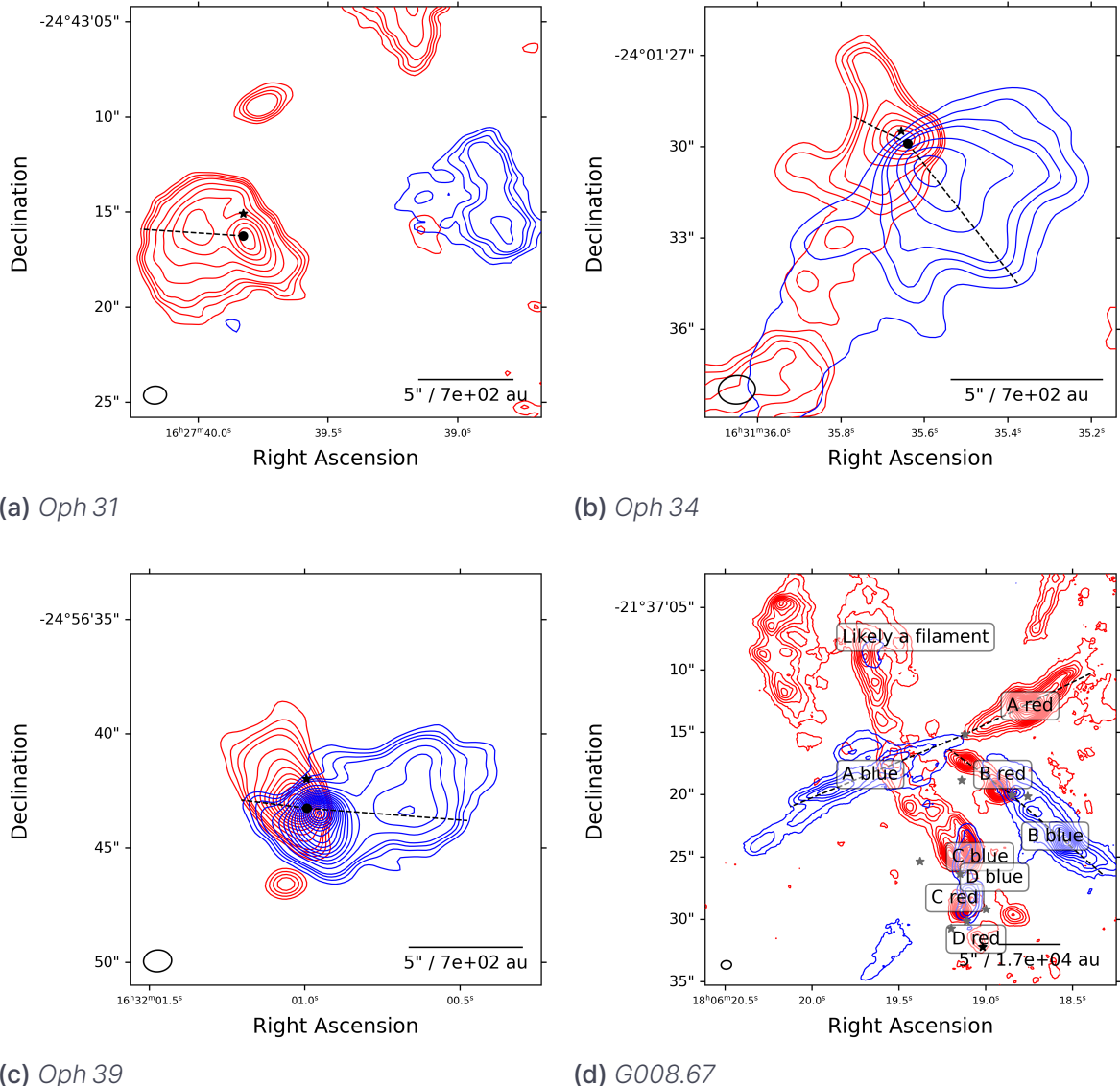
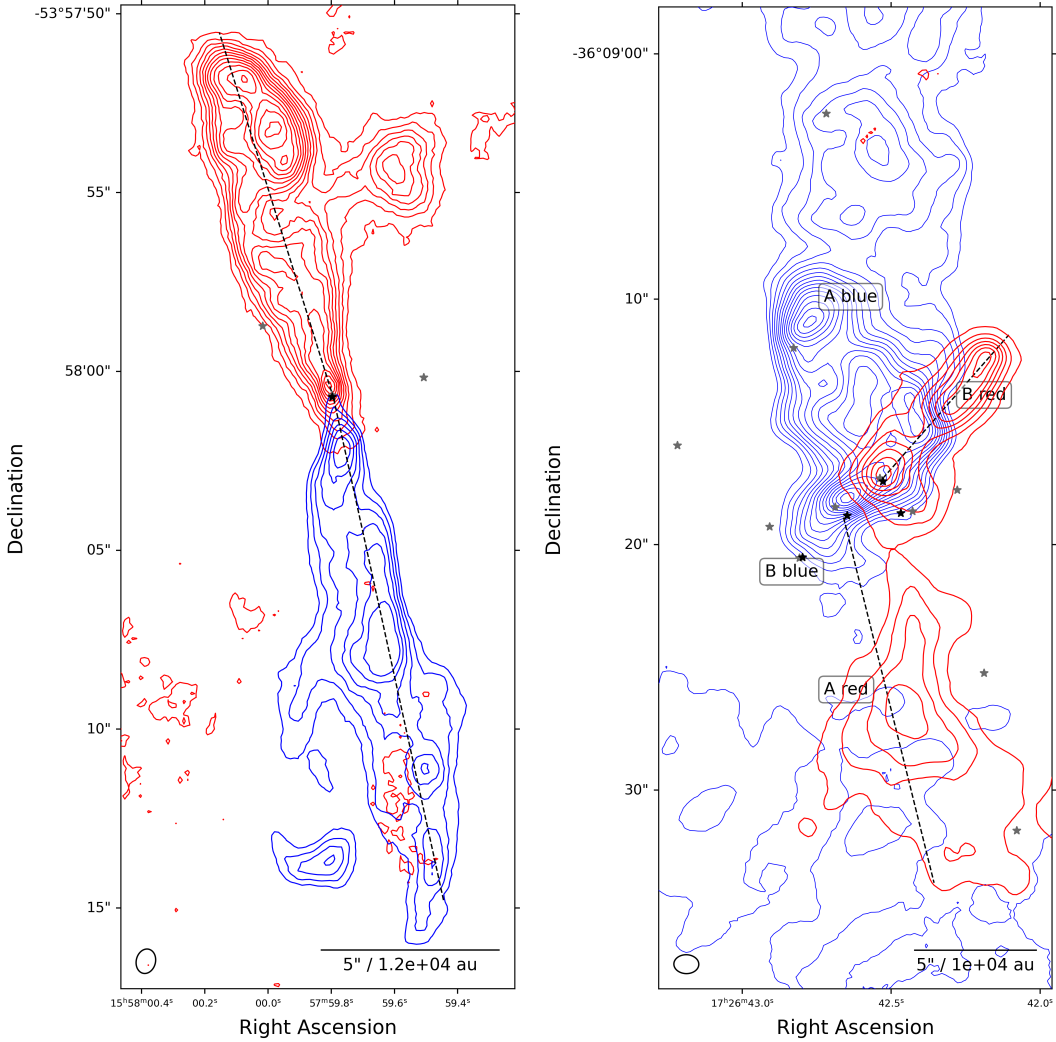
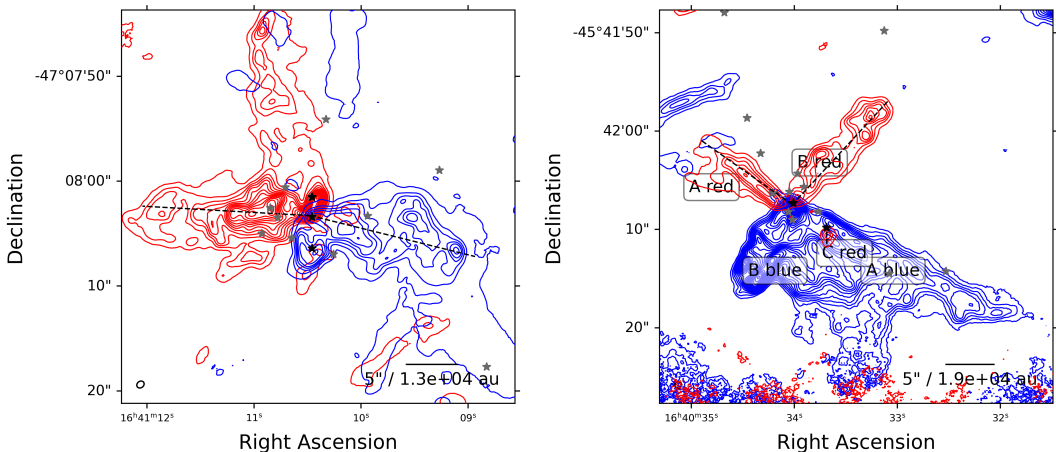


Figure 4.4: Integrated blue- and red-shifted CO (2-1) maps of sources in our low-mass sample (subfigure a-c) and high-mass sample (subfigure d). No smoothing was done on these maps. The velocity ranges used to create the maps are indicated in Table 3.1. For the low-mass sources, the contour levels are at 3σ , 4σ , 5σ , 6σ , and then at intervals of 3σ . The positions of the YSOs are indicated as black stars, if the position of the outflow axis is manually altered from the position of the YSO, the new position is indicated as a black circle. For the high-mass source G008.67, contour levels start at 3σ , and are then at intervals of 5σ . The positions of the hot cores are indicated as black stars, the positions of the continuum cores are indicated as gray stars.



(a) G328.25. The red contour levels start at 3σ , and are then at intervals of 5σ . The blue contour levels are at $(3, 4, 5, 6, 7, 8)\sigma$, and then at intervals of 5σ .

(b) G351.77. The red contour levels start at 3σ , and are then at intervals of 10σ . The blue contour levels start at 3σ , and then at intervals of 20σ .



(c) G337.92. The red contour levels start at 3σ , and are then at intervals of 10σ . The blue contour levels start at 3σ , and then at intervals of 20σ .

(d) G338.93. The contour levels start at 3σ , and are then at intervals of 5σ . The overlapping blue lobes are not included in any further calculations.

Figure 4.5: Integrated blue- and red-shifted CO (2-1) maps of sources in our high-mass sample. No smoothing was done on these maps. The velocity ranges used to create the maps are indicated in Table 3.1. Contour levels for specific sources are indicated in the sub-captions. The positions of the hot cores are indicated as black stars, the positions of the continuum cores are indicated as gray stars.

and this inclination seems reliable when visually inspecting the image, we assume this inclination remains valid for the outflow we identify. In the image, there is some unconnected blue emission, which was not included in the calculation of the opening angle. No other flux was masked out.

Oph 26

The integrated blue- and red-shifted CO (2-1) maps for Oph 26 are indicated in Figure 4.3b. We identify an isolated bipolar outflow in the east-west direction, which was also detected by van der Marel et al. (2013). They estimate an inclination of 10° , and the red- and blue-shifted lobes overlap almost completely, indicating they observe the source almost pole-on. In our work, the lobes overlap less, which might indicate that the inclination is underestimated in van der Marel et al. (2013). Both lobes were labeled as 'Likely' and were included in the further morphology analysis.

For the determination of the opening angle, the central bins of the angle distribution of the red lobe were excluded, as the red-shifted lobe contains a slight cavity which would influence the Gaussian fit. The blue lobe is asymmetric, which causes the fitted axis to be significantly offset from the initial axis. A second iteration was therefore done to determine the opening angle of the blue lobe, in which we used the fitted axis from the first iteration as the initial axis. This second iteration axis is indicated in the figure as a dashed-dotted line. By using this new axis for the determination of the opening angle, the opening angle could be fit more reliably.

Oph 27

The integrated blue- and red-shifted CO (2-1) maps of Oph 27 can be found in Figure 4.3c. We identify an outflow in the northwest-southeast direction, which we label as 'Likely'. There is some additional redshifted emission to the south, which was not included in any further calculation since it is disconnected from the YSO and the bipolar outflow. From van der Marel et al. (2013), we find this emission might be associated with the outflows of IRS 46, which lies approximately $20''$ north-east of Oph 27, outside the field of view of our observations.

van der Marel et al. (2013) has also identified this outflow, and they determine an inclination of 30° , which indicates that we are looking at the outflow quite pole-on. We indeed see quite some overlap between the red and blue lobes.

The pixel chosen for the origin of the axis is slightly offset from the position of the YSO, although the offset is smaller than the astrometric inaccuracy of 2MASS. The new origin was chosen to be in between the peak flux density of the red and blue lobes. The YSO is indicated as a black star in Figure 4.3c, while the origin is indicated as a black circle.

The red lobe is significantly flattened out, which might indicate there is an unresolved cavity influencing the shape of the lobe. Due to this shape, along with the relatively small number of pixels due to the small size of the outflow, no reliable fit could be achieved, and no opening angle was determined for this lobe.

Oph 29

The integrated blue- and red-shifted CO (2-1) maps of Oph 29 can be found in Figure 4.3d. We identify a red-shifted lobe, however the blue-shifted lobe does not seem to be connected to the central YSO. The blue lobe was therefore not included in any further calculations.

van der Marel et al. (2013) also identify this outflow, although they find a very broad red-shifted lobe to the east and a broad blue-shifted outflow to the west, coinciding with the disconnected blue lobe we find. Their identification indicates that we might be resolving out some emission. Furthermore, they observe a larger field of view and indicate the presence of a different YSO with an outflow, which falls just outside of the field of view of our observations. Therefore we find that this field might be quite chaotic, with multiple outflows interacting.

We thus only identify the radius, dynamical age, and opening angle of the redshifted lobe, which we label as 'Likely'. The blue lobe is labeled 'Possible' and is not included in further calculations. For the determination of the opening angle, we mask out some pixels on the opposite side of the YSO, as these pixels will influence the fitting. Furthermore, we mask out the parts furthest from the protostar. The opening angle is determined by the wings of the distribution, therefore masking out the central parts of the distribution is allowed.

Oph 31

The integrated blue- and red-shifted CO (2-1) maps of Oph 31 can be found in Figure 4.4a. We identify a red lobe and a disconnected blue lobe in an east-west direction. When comparing it to the smoothed images, we find some blue-shifted flux that is being resolved out in the unsmoothed images. Therefore, we labeled the blue lobe 'Possible' and did not include it in any further calculations. The red lobe is labeled as 'Likely'. Since this source was not included in the sample by van der Marel et al. (2013), we cannot make a comparison with literature and have no estimation for the inclination.

The starting point of the initial axis of the red lobe was shifted, to better constrain the opening angle. The fitted opening angle is quite wide ($\alpha = 209 \pm 14^\circ$).

Oph 34

The integrated blue- and red-shifted CO (2-1) maps of Oph 34 can be found in Figure 4.4b. We identify a bipolar outflow in the northeast-southwest direction, which we label as 'Likely'. The opening angle appears wide, and there are low SNR wings on the south side for both the red and blue lobes. The identification of these sources corresponds well with the findings of van der Marel et al. (2013), who further estimate this source to be quite pole-on, with an inclination of 30°.

For the determination of the opening angles, the southern parts of the red and blue lobes were masked out, as they carry the same weight as parts of the outflow with much higher flux densities, and would disproportionately influence the fit. Furthermore, a cavity can be seen for both the red and blue lobes. Therefore, the central bins were masked out before fitting the Gaussian distribution, which is allowed as only the wings of the distribution determine the opening angle.

Oph 39

The integrated blue- and red-shifted CO (2-1) maps of Oph 39 can be found in Figure 4.4c. We identify a bipolar outflow in the northwest-southeast direction, with a relatively wide opening angle. we label both lobes of this outflow as 'Likely'. The red and blue lobes do not seem to be aligned, possibly because the outflow might be an unresolved binary outflow, or because the axis might have shifted over time. No inclination is known from literature for Oph 39, although from the overlapping lobes we can suspect it is relatively pole-on.

For the determination of the opening angle, some small disconnected red emission was masked out, as it is likely not part of the red lobe. Some central bins were excluded from the fit, as the angle distribution appears flattened, which might indicate an unresolved cavity. Furthermore a peak in the distribution near -90° was removed, which appeared to be a consequence of the asymmetric morphology of the source. Similarly for the blue lobe, we exclude a peak in the distribution near 60° , which we suspect is caused by the outflow being an unresolved binary, and therefore asymmetric.

G008.67

The integrated blue- and red-shifted CO (2-1) maps of G008.67 can be found in Figure 4.4d. G008.67 is a complex field, at least four bipolar outflows can be identified in the field. Due to the complexity of the field, we also refer to the SiO maps by Towner et al. (2023) to identify the outflows. Outflow A, which has a red and a blue component in the northwest-southeast direction, can be confidently coupled to a continuum core (Cunningham et al., 2023), and has been identified using SiO (Towner et al., 2023). The same is true for outflow B, which has a northeast-southwest direction. Both outflow A and B are classified as 'Likely'. Outflows C and D overlap, and we cannot confidently state which lobe is part of which outflow. Therefore, we do identify these outflows, but classify them as 'Possible' and do not include them in any further calculations. Furthermore, there is some red-shifted emission, which is not coupled to any SiO emission and can not clearly be coupled to a protostar or a blue-shifted lobe. We therefore suspect this emission is a filament rather than an outflow.

For outflow B, some of the angle distribution of the red and blue lobes was masked out. No literature values for the inclination are available, however since the lobes overlap, we suspect outflow B is more pole-on compared to outflow A.

G328.25

The integrated blue- and red-shifted CO (2-1) maps of G328.25 can be found in Figure 4.5a. We identify a bipolar outflow, which appears to be quite edge-on. The blue lobe is at a significantly lower SNR compared to the red lobe, however we find that σ is higher for the blue-shifted map as well, which might explain the discrepancy. This offset in σ does not significantly influence the determined radii and opening angles.

The redshifted lobe has an asymmetric feature far away from the protostar, which might be old emission or unrelated to the outflow. This feature was masked

out in the determination of the opening angle.

G337.92

The integrated blue- and red-shifted CO (2-1) maps of G337.92 are shown in Figure 4.5c. At first sight, the source looks like a single bipolar outflow, however there are many hot cores (Bonfand et al., 2024) and continuum cores (Cunningham et al., 2023) identified in the central parts of the field. Towner et al. (2023) also identify multiple disconnected outflows in SiO, although not all red-shifted lobes can be coupled to blue-shifted lobes. We identify a bipolar outflow in the east-west direction and use this outflow for further morphology calculation, but there are likely multiple overlapping outflows in the vertical direction. Therefore we mask out some parts of the outflow when determining the opening angle, that are likely overlapping. The masked-out parts are near the center of the outflow.

G338.93

The integrated blue- and red-shifted CO (2-1) maps of G338.93 can be found in Figure 4.5d. We identify two bipolar outflows, in a northeast-southwest direction (outflow A) and in a northwest-southeast direction (outflow B). It might be a very wide single outflow, since the blue-shifted lobes overlap. However, the direction of the SiO emission suggests that they are two separate outflows. In the region of the overlapping blue-shifted lobes, a small redshifted lobe connected to a hot core can be identified, which we label outflow C. However, we cannot disentangle the blue-shifted lobe belonging to outflow C from the blue lobes of outflows A and B. Therefore, the red lobes of outflows A, B, and C are classified as 'Likely', while the blue lobes are classified as 'Possible', and not included in further calculations. Due to the limited amount of pixels in the redshifted outflow C, no angle determination was made for this source. However we can determine a radius and dynamical age for the red lobe of outflow C.

G351.77

The integrated blue- and red-shifted CO (2-1) maps of G351.77 can be found in Figure 4.5b. We identify two binary outflows, outflow A in the north-south direction, and outflow B in the northwest-southeast direction. The blue lobes overlap significantly, and we therefore do not use them in further calculations. For the red lobe of outflow B, some parts of the lobe were masked out when determining the opening angle, to account for emission on the opposite side of the YSO.

5. Discussion

In Chapter 3 and Chapter 4, we determined several physical parameters for our low- and high-mass samples. Below, we compare these parameters between the samples, compare them to literature, and attempt to couple them to known theories of high-mass star formation.

5.1 Comparing rotational temperatures

In Figure 5.1, we compare the mean value of T_{rot} for our high- and low-mass samples. The mean was taken over the entire field since the resolution of the smoothed maps was too low to accurately identify individual outflows. The rotational temperatures of the high-mass sample are indicated as upper limits, as we suspect the majority of pixels in the high-mass fields is optically thick in the CO (2-1) transition, causing us to overestimate T_{rot} (see Section 3.2.1 and below). The rotational temperatures for the low-mass sample are likely affected by non-LTE effects, as suspected by the deviation in the RDs of some low-mass sources (see Section 3.2.2). T_{rot} remains only an estimation of the true kinetic temperature of the gas. Non-LTE modeling would be required to properly constrain the kinetic temperature of the low-mass sources. Since we cannot determine whether we overestimate or underestimate the temperatures, we do not plot the rotational temperatures for the low-mass sample as upper limits.

The values of T_{rot} in our low-mass fields range between ~ 6 K to ~ 53 K. We determined the mean value of T_{rot} over our low-mass fields, and found a range between 8.3 K and 21.8 K, with a weighted mean over all fields of 11.3 ± 0.6 K. These values are in line with values found from other studies ($T_{ex} \sim 10 - 50$ K, e.g. Lada, 1985; Blake et al., 1995; Bontemps et al., 1996; Yıldız et al., 2012; Dunham et al., 2014). In this project we only studied outflows using low-J transitions of CO, therefore we are unable to trace warmer parts of the outflows, which might be detected using high-J CO transitions.

The values for T_{rot} in the high-mass fields range from negative numbers to $\sim 10^4$ K. These values are nonphysical, as negative rotational temperatures cannot exist, and the observed temperature range of outflows is 10 – 50 K. These nonphysical values are caused by the majority of the pixels in the high-mass fields being optically thick in the CO (2-1) transition. Therefore, we mask out

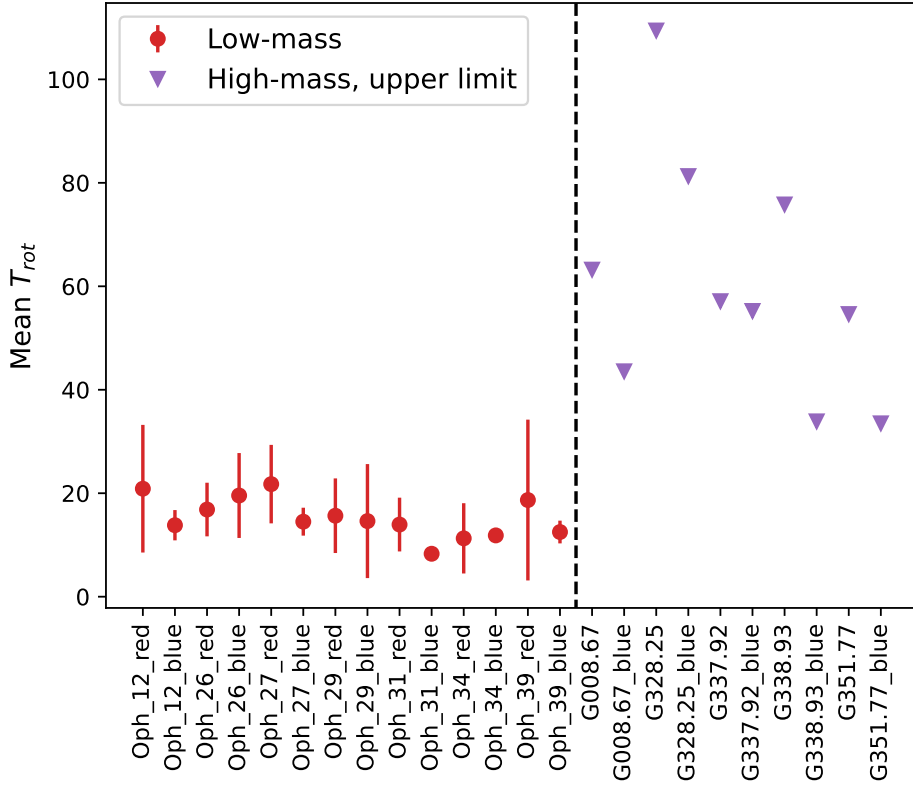


Figure 5.1: Mean values of the rotational temperatures over the entire field, separately for the red- and blue-shifted maps. The high-mass temperatures are indicated as upper limits and are plotted as the derived values from the RD method plus 1σ .

any negative values and any pixel with $T_{rot} > 200$ K, and interpret the rotational temperatures derived from the high-mass sample as upper limits. Observations of higher-J CO transitions or observations of CO isotopologues would be required to determine the rotational temperatures of the high-mass sources more accurately.

We determined the mean value of T_{rot} over each field, and found a range between 22.6 K and 58.9 K, with a weighted mean over all fields of 28 ± 6 K. As we only determined upper limits on T_{rot} for our high-mass sample, comparisons with the low-mass sample or with literature are limited. McKee & Tan (2003) state that outflows from high-mass protostars initially emerge from the same temperature gas as outflows from low-mass protostars and eventually reach temperatures of $T \sim 50 - 100$ K. The rotational temperatures for high-mass fields are indeed slightly higher than the temperatures derived for low-mass fields. However, due to severe limitations in our analysis, we cannot determine whether there is a significant difference.

5.2 Molecular material in protostellar outflows

We indicate the mean CO column densities that we derived for both our low-mass and high-mass samples in Figure 5.2, where the mean was taken over the entire

red- and blue-shifted fields.

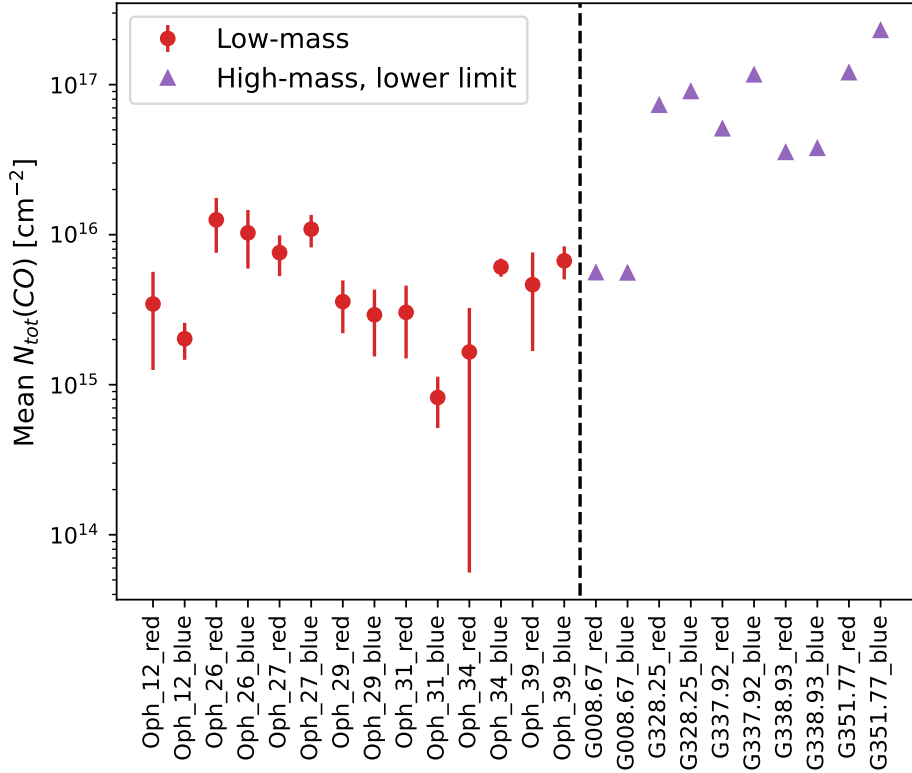


Figure 5.2: Mean column densities over the high- and low-mass fields, separately for the red- and blue-shifted maps. For high-mass fields, values are lower limits and indicated as the value derived from the RD method minus 1σ .

For the low-mass fields, mean column densities per field range between $8 \cdot 10^{14} \text{ cm}^{-1}$ and $1.26 \cdot 10^{16} \text{ cm}^{-1}$, with a weighted mean of $2.0 \cdot 10^{15} \pm 0.2 \cdot 10^{15} \text{ cm}^{-1}$. Compared to the column densities found by Tychoniec et al. (2019), the weighted mean column density of our low-mass samples is lower than the values they find in any of their sources (range between $4 \cdot 10^{16}$ and $5 \cdot 10^{17} \text{ cm}^{-2}$ for low-mass fields). This difference might be caused by a limited sample size in both of our works, as well as a difference in methodology. They determine column densities using the CO (2-1) line and an assumed value of T_{ex} of 75 K, which is a higher value than typical values of T_{rot} determined in this work. Furthermore, we have stated that low-mass sources might not be in LTE, or could contain multiple gas components, which might further influence the results we find.

For the high-mass fields, we only determined lower-limit values for the column densities, as we suspect the majority of pixels is optically thick. The mean column densities per field we found for the high-mass sample range between $6.3 \cdot 10^{15} \text{ cm}^{-1}$ and $2.6 \cdot 10^{17} \text{ cm}^{-1}$, with a weighted mean of $9.0 \cdot 10^{15} \pm 0.6 \cdot 10^{15} \text{ cm}^{-1}$. Comparisons to literature are difficult due to these lower limits. However, our results are in line with the findings by Lefloch et al. (2015), who observe an outflow around an intermediate-mass protostar using low-J CO transitions and

find column densities of $9 \cdot 10^{16} \text{ cm}^{-2}$, which is indeed higher than the lower-limit column densities we find.

We find that the high-mass fields have significantly higher CO column densities than the low-mass fields. This result is in line with previous studies, as outflows in the high-mass sample are typically both larger (e.g. Maud et al., 2015a) and more massive (e.g. Li et al., 2018) than outflows in the low-mass sample, suggesting that there is also a larger content of molecular gas.

5.3 Differences in radius and velocity

The outflow radii of our low-mass sample are between $3 \cdot 10^2 \text{ au}$ and 10^3 au , which are significantly lower than the values determined by van der Marel et al. (2013), who found low-mass outflow radii between $3 \cdot 10^3$ and $1 \cdot 10^4 \text{ au}$. As indicated in Chapter 4, van der Marel et al. (2013) observed at a lower resolution ($15''$), and they observe a larger field of view. Therefore, we might be resolving out emission that is observable in their sample, and we might be more sensitive to compact emission that is unresolvable in their observations.

We found values of R for our high-mass sample between $1.5 \cdot 10^4 \text{ au}$ and $5.5 \cdot 10^4 \text{ au}$, with an outlier for G338.93_C of $5 \cdot 10^3 \text{ au}$. Maud et al. (2015a) have observed 99 high-mass YSOs in the J=3-2 transition of C¹⁸O, and Maud et al. (2015b) have observed this same sample using ¹²CO and ¹³CO, at a resolution of $15.3''$. They determine radii by defining a source aperture and calculating an effective circular radius. This radius is then deconvolved from the beam. They find a range of deconvolved radii between $1 \cdot 10^4 \text{ au}$ and $5 \cdot 10^4 \text{ au}$. Therefore we find that the determined radii in our work are in the same order of magnitude compared to their work.

For our low-mass sample, we find values for $\Delta v = v_{\text{out}} - v_{\text{LSR}}$, between 2.4 and 15.2 km s^{-1} for Δv , which coincides well with the velocity ranges defined by van der Marel et al. (2013), who found values of Δv between 3 and 12 km s^{-1} .

We find values of Δv for our high-mass sample in the range of 35 to 90 km s^{-1} . An outlier is G351.77, which has velocities up to 130 km s^{-1} . Reasons for this source being an outlier are described below. Maud et al. (2015a) found a range of outflow velocities in the high-mass sample between 5 and 35 km s^{-1} , significantly smaller than the velocities we define. The difference in high-mass velocity ranges might be caused by them defining the velocities using C¹⁸O, which might be detectable in a smaller range of velocity bins compared to CO emission as this species primarily traces envelope material rather than outflows Tychoniec et al. (2021). Towner et al. (2023) found values of Δv roughly between 15 and 100 km s^{-1} from SiO observations of the same sources in our sample, which is more in line with the velocities we detect.

We found significantly higher radii for the high-mass sample compared to the low-mass sample. The weighted mean of the radii for our low-mass sample is $6.5 \cdot 10^2 \pm 5 \cdot 10^1 \text{ au}$, while the weighted mean radius for the high-mass sample is $2.7 \cdot 10^4 \pm 1 \cdot 10^3 \text{ au}$. This value might be biased, as high-mass YSOs are

more distant, and therefore we only identify massive outflows with larger radii. However, the absence of such large radii in the low-mass sample indicates that high-mass sources are generally larger than low-mass sources.

We found higher values for Δv for our high-mass sample compared to our low-mass sample. The weighted mean in Δv is $4.90 \pm 0.09 \text{ km s}^{-1}$ for the low-mass sample, while the weighted mean in Δv for the high-mass sample is $54.8 \pm 0.9 \text{ km s}^{-1}$. This difference might tell us that high-mass sources are more energetic and have a larger outflow force. van der Marel et al. (2013) state that the outflow force F_{CO} is calculated as

$$F_{CO} = \frac{M(\Delta v)^2}{R}, \quad (5.1)$$

where M is the mass of the outflow. The outflow force is more strongly dependent on Δv than on R . Furthermore, from the column densities, we find that the outflows driven by high-mass protostars have larger molecular gas content compared to outflows driven by low-mass protostars, suggesting M is also higher. Therefore we might find that the high-mass sources likely have a higher outflow force compared to low-mass sources. However, since we do not determine M in this project, we can not quantify this relation.

An outlier in Δv is G351.77, which has significantly higher values of Δv compared to other high-mass sources. Lurini et al. (2009) identify extremely high-velocity wings $|v - v_{lsr}| > 120 \text{ km s}^{-1}$ in CO lines for this source, which coincides with the high values of v_{out} we identify. We find that there is quite some emission in the field, both red- and blue-shifted, that we cannot couple to an outflow. Towner et al. (2023) studied the SiO (5-4) transition of G351.77 and also found additional large-scale, high-velocity emission that does not appear to trace individual outflows. They identified multiple possible explanations, such as there being an 'explosive outflow', or that a massive protostar has recently undergone an episodic accretion event in the field. A third possibility is that multiple outflows are aligned with each other, causing the high-velocity wings. However, this explanation is not preferred due to the low likelihood of both outflow axis alignment alignment of red-shift and blue-shift. Towner et al. (2023) has announced a future separate paper specifically on the high-velocity wings of this source.

5.4 Differences in the dynamical timescales

We have determined t_{dyn} for each identified lobe in our high- and low-mass sample in Section 4.1.5, as indicated in Figure 5.3. For sources with known inclination, we correct for this value. For sources with no known inclination, we correct for possible values of i ($i = [30, 50, 70]^\circ$).

We find that when we compare the uncorrected values, outflows around high-mass sources (weighted mean of $1.57 \cdot 10^3 \pm 0.07 \cdot 10^3 \text{ yr}$) have significantly larger dynamical timescales compared to outflows around low-mass sources (weighted mean of $3.2 \cdot 10^2 \pm 0.2 \cdot 10^2 \text{ yr}$). This difference is in agreement with the findings of Li et al. (2020), who find that dynamical timescales increase with core mass.

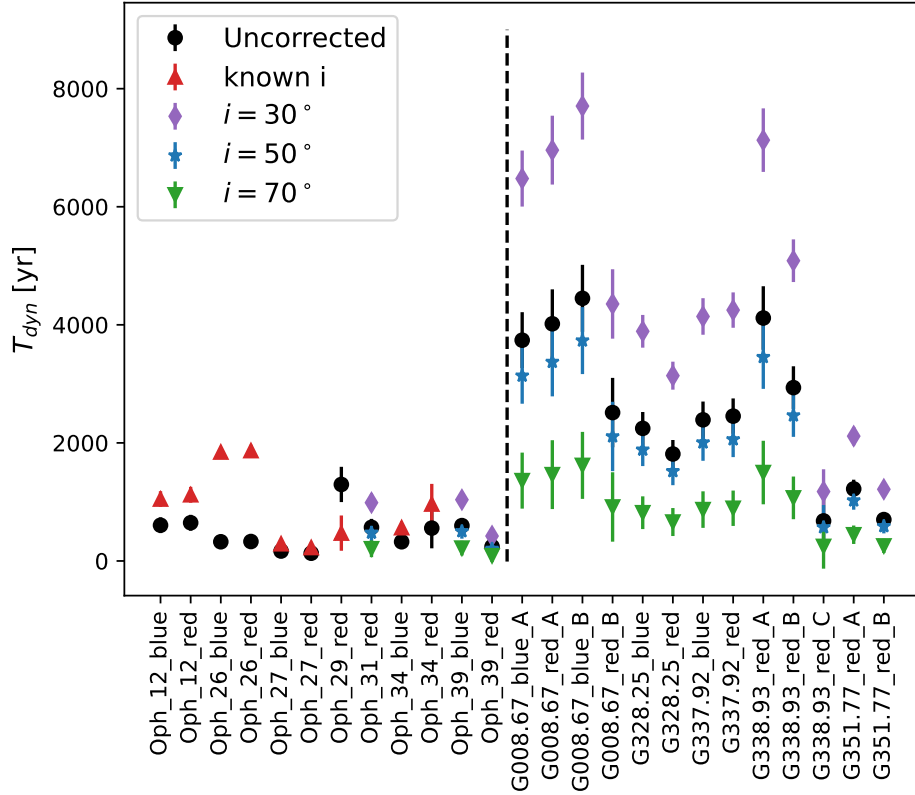


Figure 5.3: Dynamical timescales for all sources in our low-mass (left) and high-mass (right) sample. The values uncorrected for inclination are indicated as black dots. For the low-mass sources with known inclination (van der Marel et al., 2013), the corrected value is indicated as a red triangle. For all other sources with no known inclination, corrected dynamical timescales are indicated for $i = [30, 50, 70]^\circ$.

The dynamical timescales we determine for the high-mass sample are significantly smaller than the dynamical timescales determined by Maud et al. (2015b), who find values between $2 \cdot 10^4$ yr and $2.5 \cdot 10^5$ yr. However, their radii were determined using a different method, and their sources were not fully resolved, which might explain the discrepancies in the results.

Outliers in t_{dyn} are G338.93_C and G351.77, which are high-mass sources with similar dynamical timescales compared to the low-mass sources. G338.93_C is an outflow that is significantly shorter than the other outflows in the cluster (A and B), which is likely why we find smaller dynamical timescales. This outflow could have been launched more recently, or it might be a low-mass outflow in a high-mass cluster. The values of t_{dyn} for G351.77 are smaller than other high-mass sources, likely because of the high-velocity wings that have been reported for this source (Leurini et al., 2009; Towner et al., 2023). The shorter dynamical timescales might indicate that the source is highly dynamic.

Care should be taken in interpreting t_{dyn} , as often it is not representative of the true age of the outflow. Such a comparison would only hold if the outflow is launched as the protostar is formed, and keeps ejecting mass continuously

over time. This is not realistic, as outflows are highly episodic (e.g. Billot et al., 2012; Safron et al., 2015; Mairs et al., 2017), which means that t_{dyn} is rather representative of the timescale of the dynamical activity, and thus the timescale of consecutive accretion events. It should therefore only be used to estimate dynamical parameters between studies using the same methods.

5.5 Opening angles in the low- and high-mass sample

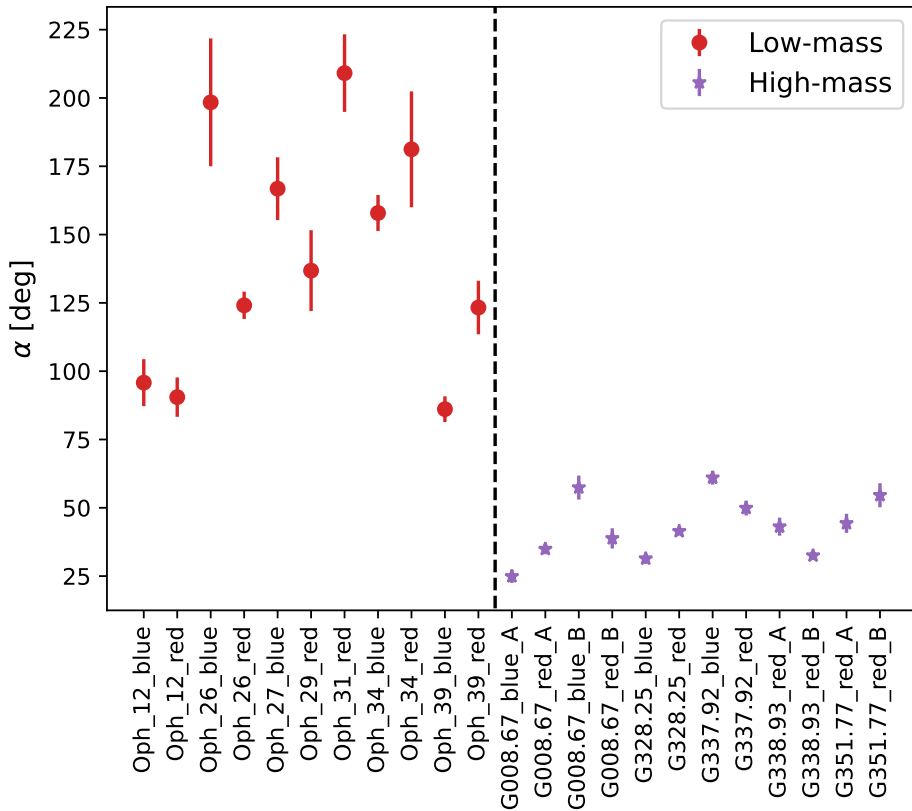


Figure 5.4: Derived opening angles for all outflows in our low- and high-mass sample. Opening angles are uncorrected for inclination.

In Figure 5.4, we compare the derived opening angles, as determined in Chapter 4, between the high- and low-mass samples. We find that high-mass sources have significantly smaller opening angles compared to high-mass sources. For the low-mass sample, we find a weighted mean opening angle of $119 \pm 2^\circ$, while for the high-mass sample, we find a weighted mean opening angle of $38.5 \pm 0.6^\circ$. The mean opening angle we find for our high-mass sample is in line with Mignon-Risse et al. (2021), who find high-mass outflow opening angles in the range of $30\text{--}70^\circ$.

Outflow opening angles are dependent on inclination since all angles observed are projected on the plane of the sky. Since for most sources, the inclination is either unknown or highly uncertain, no inclination correction was applied to the

opening angles. Therefore, the opening angles derived in this work are likely overestimated. We find that outflows in the high-mass sample have smaller opening angles than outflows in the low-mass sample, and are thus more collimated.

High-mass sources having smaller opening angles is in conflict with the findings by Richer et al. (2000) and Wu et al. (2004), who find outflows around high-mass sources to be less collimated than outflows around low-mass sources. However, Richer et al. (2000) determined that their results might be biased by selection effects, as high-mass sources with collimated outflows might have been missing from the sample. Wu et al. (2004) also mentioned that multiple outflows might be unresolved and identified as a single outflow, which would be more prevalent for high-mass sources as they occur in more clustered environments (e.g. Tan et al., 2014; Zhang et al., 2015; Rosen et al., 2020). Therefore the difference between our work and earlier research might be caused by the limited resolution and sample size of high-mass sources.

Since high-mass stars typically form in more clustered environments, it might be expected that in the high-mass sample, protostellar outflows would have larger opening angles than in the low-mass sample. In clustered environments, there is significant substructure and clumpy material (e.g. Rosen et al., 2020; Lada & Lada, 2003), and surrounding YSOs and outflows are more likely to interact with the outflow. Both of these factors would increase the opening angle of a high-mass protostellar outflow.

The smaller opening angles for high-mass sources that we find might be explained by them having larger outflow forces and being more energetic, as was also suggested in Section 5.3. The increased energy in an outflow would allow it to remain collimated for longer, despite the clustered environment. According to the Competitive Accretion model, mass accretes in a chaotic way from a broader region around a protostar. This chaotic accretion might cause outflows to behave more chaotically as well, from which we would expect that outflows in the high-mass sample have broader opening angles than outflows in the low-mass sample. As we find the opposite, this might be evidence in favor of the 'Core Accretion' model. However, a number of other physical circumstances might influence the broadening of outflow opening angles, therefore we can not state with confidence that high-mass outflows form according to a scaled version of low-mass star formation.

According to the evolutionary track of outflows around high-mass sources established by Beuther & Shepherd (2005), well-collimated outflows around high-mass stars are young and are not associated with a UCHII region yet, and the opening angle increases as a wide-angled wind starts to dominate. As we mostly identify small opening angles for the high-mass sources, we suggest that these are typically quite young. However, since the proposed evolutionary track does not indicate specific ranges of opening angles, this statement can not be quantified.

The results we find might be biased by selection effects, as we identify and classify outflows 'by eye'. Since high-mass sources occur in more clustered environments, we might be more likely to label less-collimated outflows as 'Possible',

when they overlap or interact with other outflows in the field. Low-mass sources are often isolated, therefore we often classify an outflow as 'likely', even if it is barely collimated.

5.6 The evolution of opening angles with age

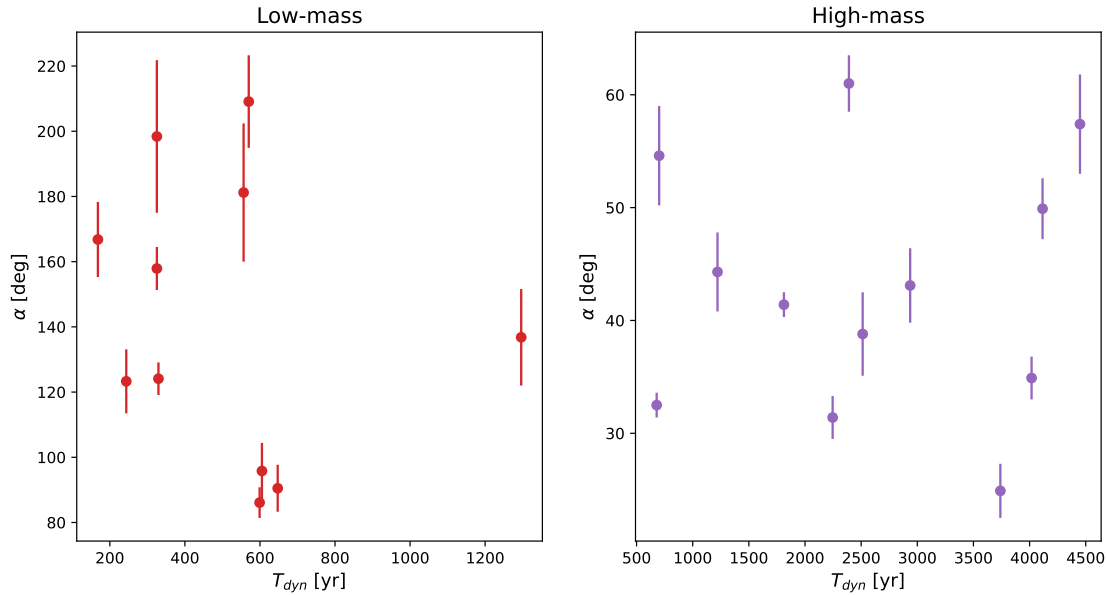


Figure 5.5: Opening angles of low-mass (left) and high-mass (right) outflow lobes, as a function of the dynamical timescale. No correlation can be determined.

It is generally accepted that outflow opening angles grow as a source ages, due to the interactions with the envelope (e.g. Velusamy & Langer, 1998; Arce & Sargent, 2006; Lee & Ho, 2005). In Figure 5.5, we plot the opening angle of each lobe against the dynamical timescale. We find no correlation between dynamical timescales and opening angles, likely because the dynamical timescale is not a proxy for the true age of a YSO, and rather measures the timescale of dynamical activity.

In an attempt to determine a relationship between the evolutionary stage and opening angle, we compare our derived opening angles with the evolutionary stages known from Motte et al. (2022) for the high-mass sample, and Van Kempen et al. (2009) for the low-mass sample.

It is important to note that for the high-mass sources, no evolutionary stage is known for individual YSOs. Rather, the evolutionary stage of the clump is known, which is classified as either 'Young', 'Intermediate', or 'Evolved'. Of the 12 high-mass lobes for which we define the opening angle, six are in a 'Young' cluster, and six are in an 'intermediate' cluster. We find the mean opening angle of the 'Young' lobes is $43 \pm 2^\circ$, while the mean opening angle for the 'Intermediate' lobes is $42 \pm 3^\circ$. Thus, we find no correlation between the protocluster evolutionary stage and opening angles, although this result might be limited by sample size.

A relationship might be found if we were to compare the opening angle with the evolutionary stage of individual high-mass YSOs, rather than the cluster evolutionary stage.

For the low-mass samples, evolutionary stages have been determined for individual YSOs. We are again limited by sample size, as four outflows (Oph 12, Oph 26, Oph 27, and Oph 29) are classified as Class I embedded YSO, but only Oph 31 is a Class II source with a protostellar disk. Oph 34 was classified as Class I(T), a source in transition between Class I and Class II. The relation we find in Figure 5.6 does not contradict opening angles growing with the evolutionary stage, however, there are too few Class II sources in our sample to properly determine a relation between the opening angle and evolutionary stage. Furthermore, there is a total lack of Class 0 sources in our sample, which limits a proper comparison.

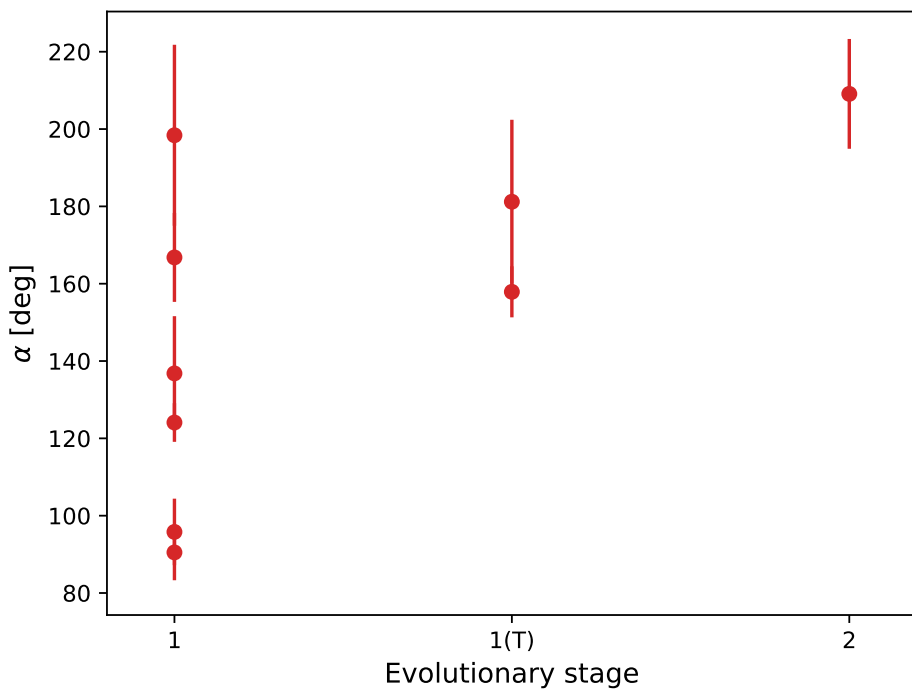


Figure 5.6: The opening angles of outflows in the low-mass sample, as a function of the evolutionary stage that was defined by Van Kempen et al. (2009).

6. Conclusions & future outlook

6.1 Conclusions

Although low-mass star formation is typically well-understood, the mechanisms behind high-mass star formation are still under debate due to the rarity and consequent distance of high-mass protostars. Protostellar outflows have been detected around the vast majority of YSOs, and play a vital role in the star formation process. In this work, we have studied five high-mass protostellar clusters, selected from the ALMA-IMF program (e.g. Motte et al., 2022), and seven low-mass YSOs in the ρ Ophiuchi molecular cloud. More details about the samples we study can be found in Chapter 2. We have created maps of rotational temperatures and CO column densities of outflows in these fields, as was described in Chapter 3. In Chapter 4, we identified candidate outflows, and classified the lobes of these outflows as either ‘Possible’ or ‘Likely’. Of each ‘Likely’ lobe, we attempted to constrain the outflow radius, the outer velocity, the dynamical timescale, and the opening angle. In Chapter 5, we compared the derived parameters between the low- and high-mass samples, and attempted to couple these parameters to current theories on high- and low-mass star formation theory. We summarize our findings below.

- We compared the derived values for T_{rot} between our low-mass and high-mass samples (see Figure 5.1). Due to optically thick transitions, the temperatures for T_{rot} derived for the high-mass sample were considered to be upper limits. A deviation could be seen in the RD of some pixels in the low-mass sample, which suggested that there could be non-LTE effects, or that we might have been observing multiple gas components with different temperatures within the same beam. The derived rotational temperatures suggested that the outflows in our high-mass sample are slightly warmer than the outflows in our low-mass sample, however due to the limitations in our analysis, this result could not be confirmed.
- We compared the derived CO column densities $N_{tot}(\text{CO})$ between our low- and high-mass samples, where the high-mass column densities were considered to be lower limits due to optically thick transitions. We found that the high-mass sample (weighted mean of $9.0 \cdot 10^{15} \pm 0.6 \cdot 10^{15} \text{ cm}^{-2}$, lower limit) had larger values of $N_{tot}(\text{CO})$ compared to the low-mass sample (weighted

mean of $2.0 \cdot 10^{15} \pm 0.2 \cdot 10^{15} \text{ cm}^{-2}$), from which we concluded that outflows driven by high-mass protostars have more molecular material than outflows driven by low-mass protostars.

- We found that outflows in our high-mass sample have significantly larger radii (weighted mean of $2.7 \cdot 10^4 \pm 1 \cdot 10^3 \text{ au}$) than outflows in the low-mass sample (weighted mean of $6.5 \cdot 10^2 \pm 5 \cdot 10^1 \text{ au}$). It should be mentioned that this result might be biased by selection effects, as the high-mass protoclusters are significantly further away compared to the sources in our low-mass sample, and therefore smaller outflows in the high-mass sample might not be identified. However, due to an absence of larger outflows in the low-mass sample, we could still conclude that outflows driven by high-mass sources are typically larger than outflows driven by low-mass sources.
- We found that outflows driven by high-mass protostars have velocities Δv that are larger (weighted mean of $54.9 \pm 0.9 \text{ km s}^{-1}$) than outflows driven by low-mass protostars (weighted mean of $4.90 \pm 0.09 \text{ km s}^{-1}$). This result could suggest that the outflows in the high-mass sample are more energetic and have higher outflow forces compared to the outflows in the low-mass sample.
- By dividing R by Δv , we obtained an estimate for the dynamical timescale t_{dyn} (see Figure 5.3). We corrected for the inclination when available. If no inclination was known for the outflow, we corrected for possible values of the inclination. We found that the weighted mean of the dynamical timescale in the low-mass sample is $3.2 \cdot 10^2 \pm 0.2 \cdot 10^2 \text{ yr}$, while the mean dynamical timescale in the high-mass sample is $1.57 \cdot 10^3 \pm 0.07 \cdot 10^3 \text{ yr}$, both uncorrected for inclination. Therefore we concluded that outflows driven by high-mass protostars typically have higher dynamical timescales compared to outflows driven by low-mass protostars. It should be noted that t_{dyn} is not a tracer of the true age of an outflow, and rather traces the timescale of dynamical activity, and thus of the timescale between consecutive accretion events.
- We determined the opening angles of the outflows in our low-mass and high-mass samples (see Figure 5.4). We found that the outflows in our high-mass sample (weighted mean of $38.5 \pm 0.5^\circ$) have significantly smaller opening angles than the outflows in our low-mass sample (weighted mean of $119 \pm 2^\circ$). It should be noted that these angles are projected in the plane of the sky, and are thus uncorrected for inclination. We might be biased toward more collimated outflows in the high-mass sample compared to the low-mass sample, since there are typically multiple outflows present in a high-mass field, while outflows driven by low-mass protostars are usually more isolated.

Since high-mass protostars typically form in more clustered environments (e.g. Tan et al., 2014; Zhang et al., 2015), it might be expected that the

outflows in our high-mass sample would have larger opening angles due to interactions with the surrounding cloud and neighboring outflows. We instead found that outflows in the high-mass sample have smaller opening angles, which could be explained by the outflows being more energetic and having a larger outflow force, as we also suggested based on the velocities of the outflow. These larger energies would allow the outflow to remain more collimated. Since we find collimated outflows in our high-mass sample, the evolutionary scheme of outflows around high-mass protostars as proposed by Beuther & Shepherd (2005) might suggest that we are observing typically young outflows in the high-mass sample, although we are unable to quantify this result.

The main differences between the different theories of high-mass star formation are in the manner of accretion. The Core Accretion model is a scaled-up version of low-mass star formation, in which a high-mass star forms through a gravitationally bound core, while the Competitive Accretion model assumes high-mass protostars accrete chaotically from a wider region of the clump. According to the latter mechanism, it might be expected that since accretion is more chaotic, outflows would be more chaotic as well, and therefore be less collimated. As we find that outflows in the high-mass sample are in fact highly collimated, this might be in favor of Core Accretion. However, since a number of other mechanisms are involved in the widening of outflow angles, we are unable to state with confidence that high-mass protostars indeed form similarly to low-mass star formation.

The outflow parameters we derive are typically larger in the high-mass sample, which could indicate that the preferred high-mass star formation mechanism is indeed Core Accretion. However, since we do not know exact protostar masses, we can not determine whether these outflow parameters scale proportional to the mass. In Competitive accretion, these outflow parameters could also be increased, therefore we can not reach a definite conclusion.

6.2 Future outlook

In this work, we were unable to properly constrain the rotational temperatures and CO column densities in our high-mass sample, as the CO (2-1) transition was likely optically thick for a significant number of pixels. In order to more accurately constrain these parameters, additional observations of CO transitions would be required. The CO (1-0) line would likely be even more affected by optical depth, therefore higher-J CO transitions, such as the CO (4-3) or the CO (6-5) transition, are more suitable. Additionally, CO isotopologues such as ^{13}CO and C^{18}O might be used to extend the RD, as these rarer isotopologues are significantly less affected by optical thickness. An isotopologue abundance ratio would need to be assumed, which are typically well determined (e.g. Wilson & Rood, 1994).

We have seen that our low-mass sample is likely affected by either non-LTE effects, or that we might be observing multiple gas components with different

temperatures in the same beam. These conditions might make the determined rotational temperatures and column densities less reliable. We might be able constrain the physical parameters in the outflows more accurately using a non-LTE radiative transfer code, such as *RADEX*. Although we were not able to constrain these parameters using *RADEX* for the high-mass sample, as described in Appendix A.1, such an analysis might be more successful for the low-mass sample, since an additional CO transition is observed.

We determined outflow parameters such as radii, dynamic ages, and the opening angles of outflows based on the CO (2-1) observations. However, our samples are limited by the availability of additional ALMA CO observations that are required for constructing the RD, but that are unused for this analysis. Our samples could be expanded by determining outflow parameters in fields with no additional CO observations available.

The ALMA-IMF program consists of 15 massive protoclusters with available CO (2-1) observations, of which we only include five in our high-mass sample. Determining the outflow parameters of the other ten fields would increase the size of our high-mass sample roughly threefold. Furthermore, of the five fields included in our high-mass sample, we do not use the whole image, instead we limit ourselves to the field of view of the additional available CO transitions. More outflows could be identified within the fields of our existing high-mass sample, if we use the entire available image.

For the low-mass sample, 41 sources are observed in the project of our CO (2-1) observations (2019.1.01792.S, PI: Mardones), of which we only select seven. The remaining 34 sources have similar resolutions ($\sim 1''$) and observe the same CO transitions. Adding these sources to our low-mass sample would expand it by a factor of almost six.

If the outflow parameters are determined for more sources in the low- and high-mass fields, we could constrain the typical values of these parameters more accurately. Comparing inclination-dependent parameters between the low- and high-mass samples would be more reliable, as for a large enough sample the inclination should be distributed randomly. Furthermore, we might compare more robustly the relation between the opening of an angle and the evolutionary stage of its driving source. We attempted to make such a comparison in Figure 5.6, however our conclusions were limited by sample size. Van Kempen et al. (2009) derived evolutionary stages of 45 YSOs in the ρ Ophiuchi cloud, which would allow for a more well-sampled comparison.

We were unable to compare the evolutionary stage of high-mass YSOs with the outflow opening angles derived for our high-mass sample, as only evolutionary stages of the protoclusters were determined, not of individual sources. If such classifications are available, we might determine whether the outflow opening angles grow with the protostar evolutionary stage, as we suggested by Beuther & Shepherd (2005).

A valuable addition to the work done in this project would be to determine additional outflow parameters, such as the momentum p , outflow mass, outflow force, and the mass outflow rate \dot{M} . Furthermore, determinations of the protostar

mass would be needed to distinguish between different mechanisms of star formation. We find that outflows driven by high-mass stars are likely more massive and more energetic compared to outflows driven by low-mass stars, which could either be caused by the star formation mechanism being different between low- and high-mass stars, or by the high-mass stars being simply more massive and thus scaled-up from low-mass stars. The mass of the protostars would allow us to determine whether the increase in outflow mass and energy scales proportionately, which might indicate that the Core Accretion model applies. If the increase in outflow properties is not proportional to the increase in protostar mass, this could indicate that the Competitive Accretion model might apply.

A. Appendix

A.1 Constraining the physical high-mass parameters using *RADEX*

As was described in section 3.2.1, the assumption that our high-mass fields are optically thin might not always hold. Therefore, the rotational temperatures and column densities we find for the high-mass sources are considered to be upper and lower limits, respectively. We attempted to constrain the kinetic temperatures and hydrogen densities $n(H_2)$ independent of optical depth using *RADEX* (van der Tak et al., 2007). *RADEX* is a statistical equilibrium radiative transfer code. While the RD method requires the assumption that all transitions are optically thin and the observed object is in local thermodynamic equilibrium, *RADEX* uses the escape probability formulation, assuming an isothermal and homogeneous medium without large-scale velocity fields. This method can be reliable even when optically thick transitions are detected, or if the source is not in local thermal equilibrium.

We initially attempted to run *RADEX* on the high-mass field G328.25, as this is the field with the most masked out pixels from the RD method, and therefore likely the most affected by optically thick transitions. As we only observe our high-mass fields in two transitions, we run *RADEX* with only two free parameters, $n(H_2)$ and T_{kin} . An overview of all input parameters is found in Table A.1.

For T_{kin} , a range was chosen between 25 K and 225 K, in steps of 25 K. This range was based on the typical temperature range of outflows around low-mass protostars (10–50 K, e.g. Lada, 1985; Blake et al., 1995; Bontemps et al., 1996; Yıldız et al., 2012; Dunham et al., 2014), which was extended to higher temperatures as outflows around high-mass protostars might be warmer than outflows around low-mass outflows. Van Kempen et al. (2016) find temperatures above 50 K for outflows observed in CO (6–5), and Hoang et al. (2023) find a range of temperatures in outflows around high-mass protostars between 120 and 220 K for high CO ($> J = 11\text{--}10$) transitions, although this likely traces warmer gas.

The other free parameter was the hydrogen number density, for which we defined a grid of values between $1 \cdot 10^3$ and $1 \cdot 10^7 \text{ cm}^{-3}$. Nisini et al. (2007) find values of $n(H_2)$ between 10^5 and 10^6 cm^{-3} in molecular bullets associated with outflows around low-mass protostars. Lefloch et al. (2015) find for the intermediate-mass protostellar outflow Cepheus E that values of $n(H_2)$ in the

jet between $5 \cdot 10^4$ and $1 \cdot 10^5 \text{ cm}^{-3}$, traced by low-J transitions. Since these values are not based on high-mass sources, we choose to extend our grid to reach significantly higher and lower densities than what is defined in these papers.

We fixed the input CO column density at $1 \cdot 10^{17} \text{ cm}^{-2}$, which was chosen based on typical values in the LTE maps of G328.25. For the line width, we selected a fixed value of 15 km s^{-1} , based on the average of a Gaussian fit to the line wings of G328.25. Furthermore, we selected the homogeneous slab geometry, which is most suitable for protostellar outflows. We used ortho- and para-H₂ as collisional partners, with the default ortho-to-para ratio of 3. Energy levels, frequencies, and Einstein A coefficients were taken from the LAMDA database (Schöier et al., 2005). Collisional rate coefficients were taken from Yang et al. (2010), and are available for temperatures between 2 K and 3000 K for energy levels up to $J_{\text{upper}} = 40$.

Parameter	Value(s)
T_{kin}	[25, 50, 75, 100, 125, 150, 175, 200, 225] K
$n(\text{H}_2)$	[1e3, 5e3, 1e4, 5e4, 1e5, 5e5, 1e6, 5e6, 1e7] cm ⁻³
$N_{\text{tot}}(\text{CO})$	$1 \cdot 10^{17} \text{ cm}^{-2}$
Line width	15 km s^{-1}
Geometry	Homogenous slab
Collisional partners	H ₂

Table A.1: The input parameters for running RADEX.

Running RADEX using these input parameters resulted in a grid of values for the flux density of the CO (2-1) and CO (3-2) lines, for different combinations of T_{kin} and $n(\text{H}_2)$. We then used the χ^2 goodness-of-fit test to determine for which values of T_{kin} and $n(\text{H}_2)$ we found the best fit. This test minimizes the value of χ , which is determined by

$$\chi^2 = \sum \frac{(O - E)^2}{E}, \quad (\text{A.1})$$

where O is the observed velocity-integrated flux from our CO (2-1) and CO (3-2) maps, and E are the integrated flux densities returned from RADEX. The observed flux densities were determined by taking the mean velocity-integrated flux density over the whole outflow, separately for both the red-shifted and blue-shifted components.

As we determine χ^2 for one degree of freedom, the χ^2 value for significance $\alpha = 0.05$ is 3.841. The resulting χ^2 values we found were higher than 80, which indicated that even the lowest χ^2 values would not provide a reliable constraint on T_{kin} and $n(\text{H}_2)$.

Several attempts were made to constrain the parameters better. By integrating the observed flux densities over smaller regions within the outflow, we expected that the regions would be more homogeneous. This did not result in lower values

of χ^2 . We also ran *RADEX* in a finer grid of T_{kin} and $n(H_2)$, while spanning the same range of values, which also did not provide a better fit.

By changing the initial CO column density to $1 \cdot 10^{18} \text{ cm}^{-2}$, lower χ^2 values were found (between 25 and 50). However, this then resulted in values for $n(H_2)$ to be at $1 \cdot 10^7 \text{ cm}^{-2}$. As this is the highest possible value that can be returned, the *RADEX* grid was extended to even higher hydrogen densities (up to $1 \cdot 10^{13}$). However, the derived value for $n(H_2)$ again returned the highest value that could be returned. Therefore we found that for a CO column density of $1 \cdot 10^{18} \text{ cm}^{-2}$, no fit could be constrained.

We further attempted to constrain T_{kin} and $n(H_2)$ by increasing the number of molecular lines available. Since no other ALMA CO measurements are available, we attempted to include transitions from other molecules in the analysis, which would not be allowed in the RD method. In the ALMA-IMF program, multiple other molecular lines are available. It is important to ensure these lines trace the same gas as CO. Candidates were the C¹⁸O (2-1) line and the SiO (5-4) line. We opted for the SiO line, as the C¹⁸O line did not seem to be tracing the same gas due to a lack of detected high-velocity wings. The SiO line might also trace different regions, since SiO is known to also trace the high-velocity jet. We selected a small region where both SiO and CO were emitting strongly and performed the same experiment as above. This does require the SiO column density to be fixed, which was taken as $7 \cdot 10^{12} \text{ cm}^{-2}$ (e.g. Gibb et al., 2004). Even when including the SiO transition, the values for χ^2 were still too high (>20). Therefore, we were still not able to constrain the physical parameters, which might be caused by the SiO line tracing different gas than the CO lines.

As a final attempt, we performed the initial test, so without including SiO and using the grid defined in Table A.1, on another field (G338.93), where fewer pixels were masked out. These provided slightly better χ^2 values (between 15 and 40). However, the values found for the hydrogen number density would then be $5 \cdot 10^3 \text{ cm}^{-3}$, significantly lower than the typical values derived in molecular outflows, which would be in a range of $n(H_2)$ between $5 \cdot 10^4$ and 10^6 cm^{-3} .

We conclude that there is simply too little data available to provide a reliable fit of the high-mass fields using either the RD method or *RADEX*.

A.2 Rotational temperature and column density maps

The maps of T_{rot} and $N_{tot}(\text{CO})$ as derived in Chapter 3 can be found below for all sources in the low-mass and high-mass sample. Not indicated is G338.93, which was indicated in Figure 3.3.

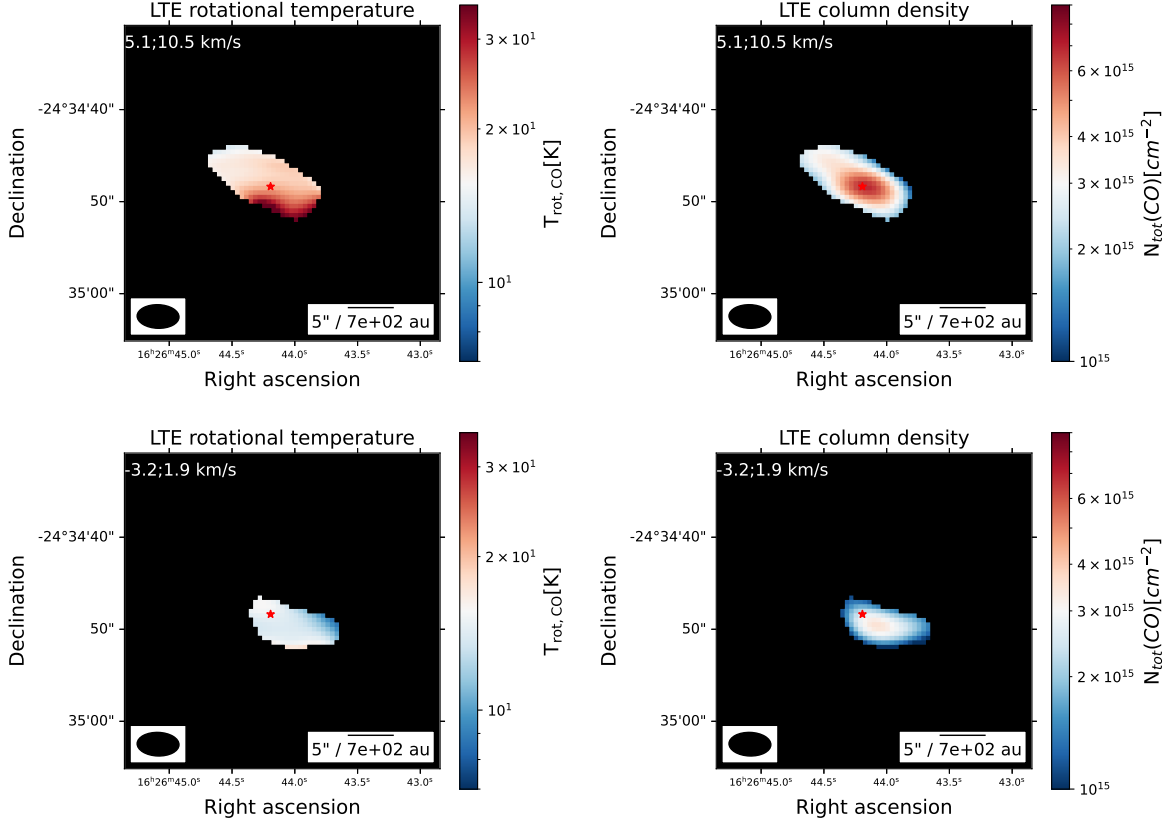


Figure A.1: T_{rot} and $N_{\text{tot}}(\text{CO})$ maps for Oph 12. The upper plots indicate the red-shifted lobes, integrated between 5.1 and 10.5 km s $^{-1}$. The lower plots indicate the blue-shifted lobes, integrated between -3.2 and 1.9 km s $^{-1}$. The beam size is indicated in the bottom left of each figure, a scale bar is indicated in the bottom right of each figure. 2MASS sources identified as YSO are indicated as red stars (Skrutskie et al., 2006; Bontemps et al., 2001).

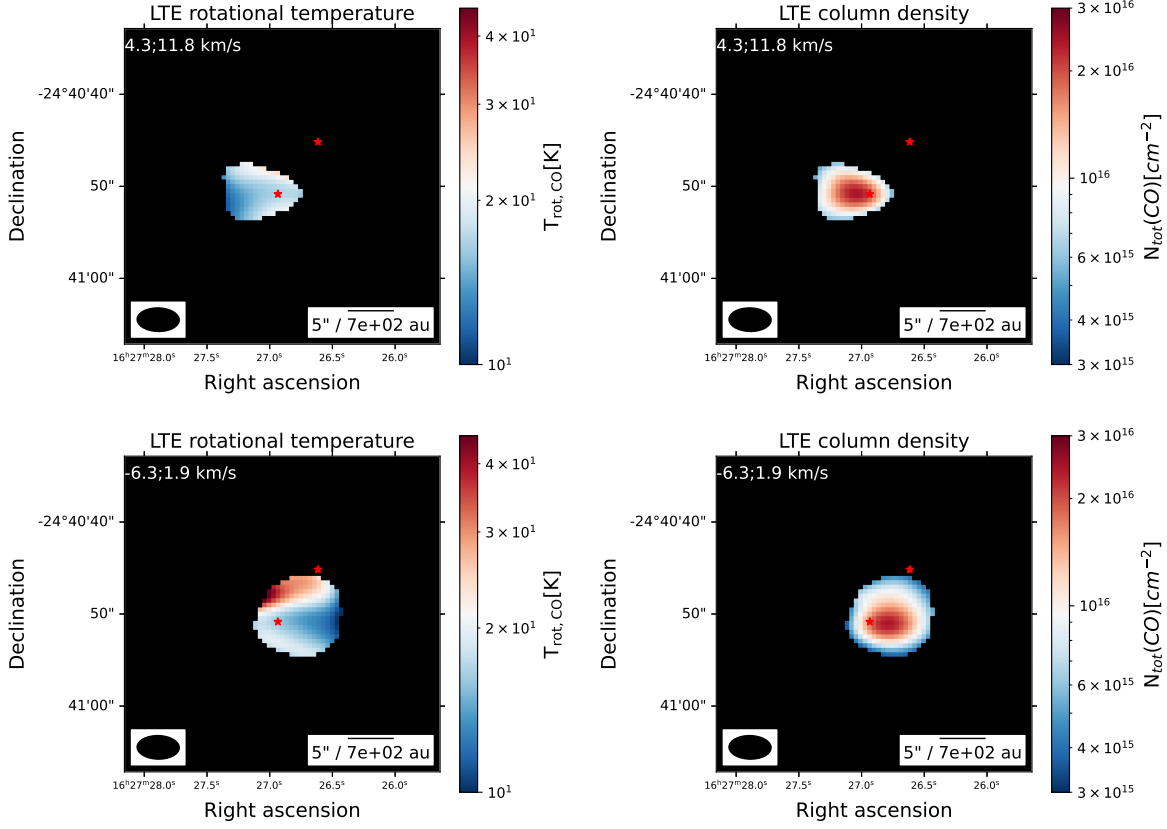


Figure A.2: T_{rot} and $N_{\text{tot}}(\text{CO})$ maps for Oph 26. The upper plots indicate the red-shifted lobes, integrated between 4.3 and 11.8 km s^{-1} . The lower plots indicate the blue-shifted lobes, integrated between -6.3 and 1.9 km s^{-1} . The beam size is indicated in the bottom left of each figure, a scale bar is indicated in the bottom right of each figure. 2MASS sources identified as YSO are indicated as red stars (Skrutskie et al., 2006; Wilking et al., 2008).

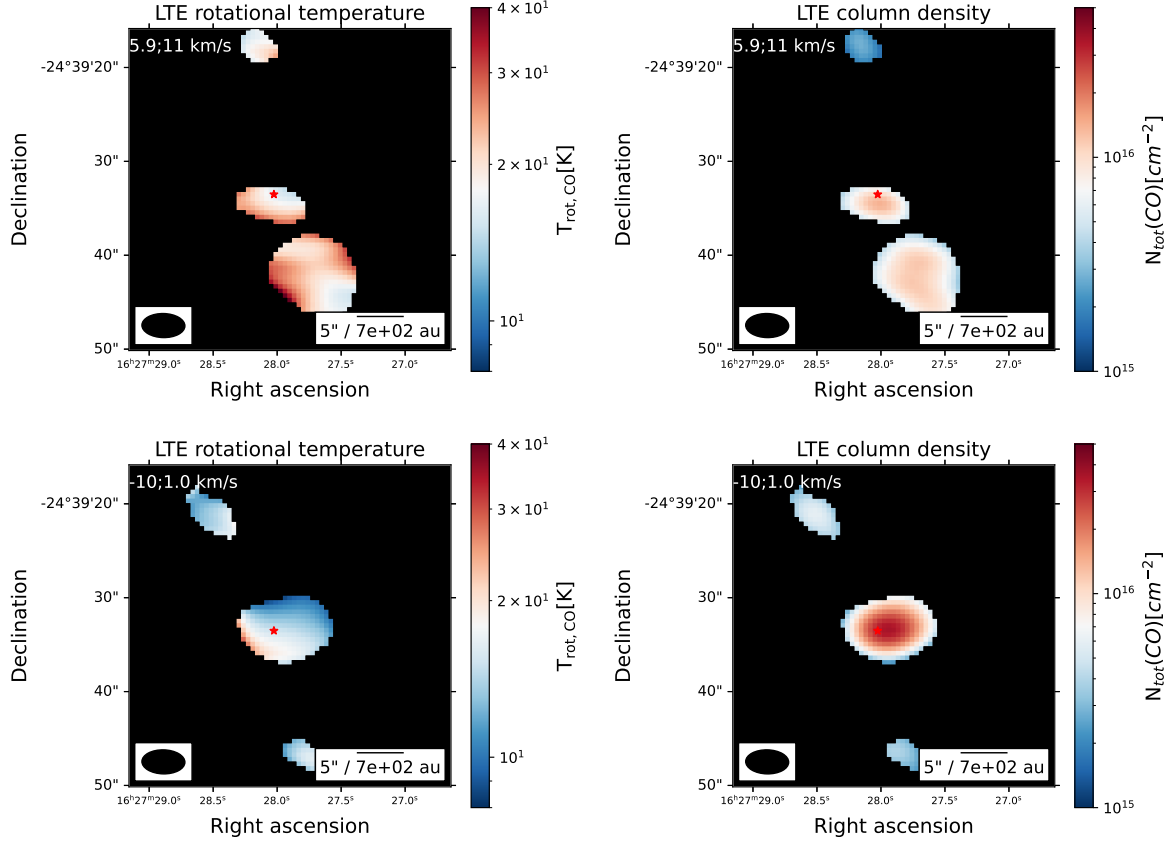


Figure A.3: T_{rot} and $N_{\text{tot}}(\text{CO})$ maps for Oph 27. The upper plots indicate the red-shifted lobes, integrated between 5.9 and 11.0 km s^{-1} . The lower plots indicate the blue-shifted lobes, integrated between -10.0 and 1.0 km s^{-1} . The beam size is indicated in the bottom left of each figure, a scale bar is indicated in the bottom right of each figure. 2MASS sources identified as YSO are indicated as red stars (Skrutskie et al., 2006; Wilking et al., 2008).

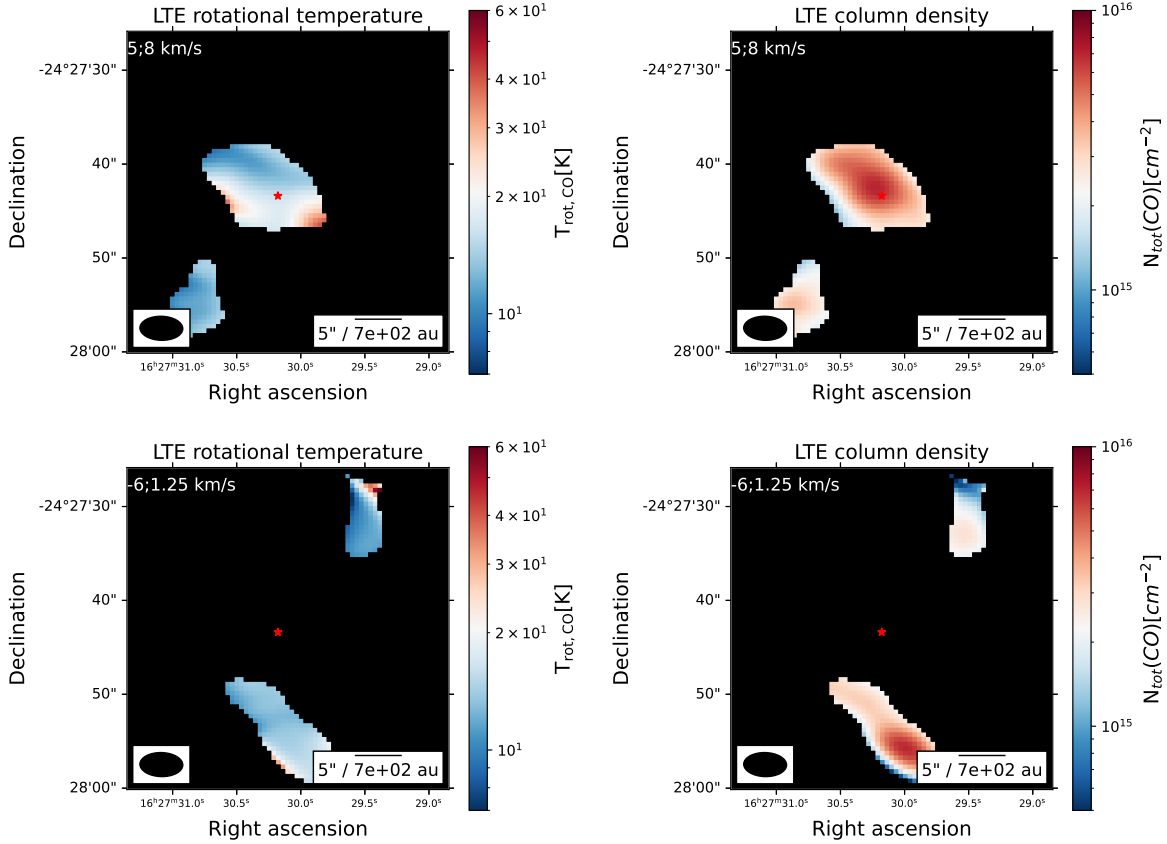


Figure A.4: T_{rot} and $N_{\text{tot(CO)}}$ maps for Oph 29. The upper plots indicate the red-shifted lobes, integrated between 5.0 and 8.0 km s^{-1} . The lower plots indicate the blue-shifted lobes, integrated between -6.0 and 1.3 km s^{-1} . The beam size is indicated in the bottom left of each figure, a scale bar is indicated in the bottom right of each figure. 2MASS sources identified as YSO are indicated as red stars (Skrutskie et al., 2006; Wilking et al., 2008).

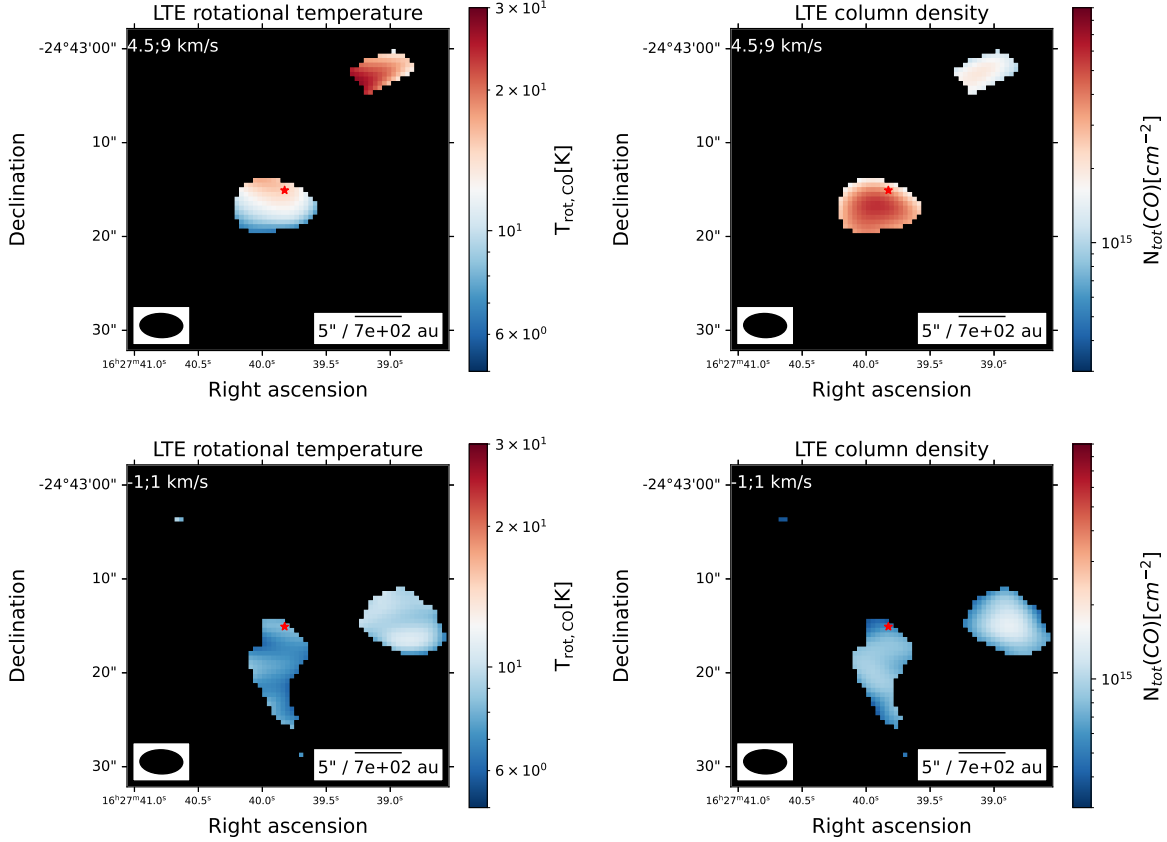


Figure A.5: T_{rot} and $N_{\text{tot(CO)}}$ maps for Oph 31. The upper plots indicate the red-shifted lobes, integrated between 4.5 and 9.0 km s^{-1} . The lower plots indicate the blue-shifted lobes, integrated between -1.0 and 1.0 km s^{-1} . The beam size is indicated in the bottom left of each figure, a scale bar is indicated in the bottom right of each figure. 2MASS sources identified as YSO are indicated as red stars (Skrutskie et al., 2006; Wilking et al., 2008).

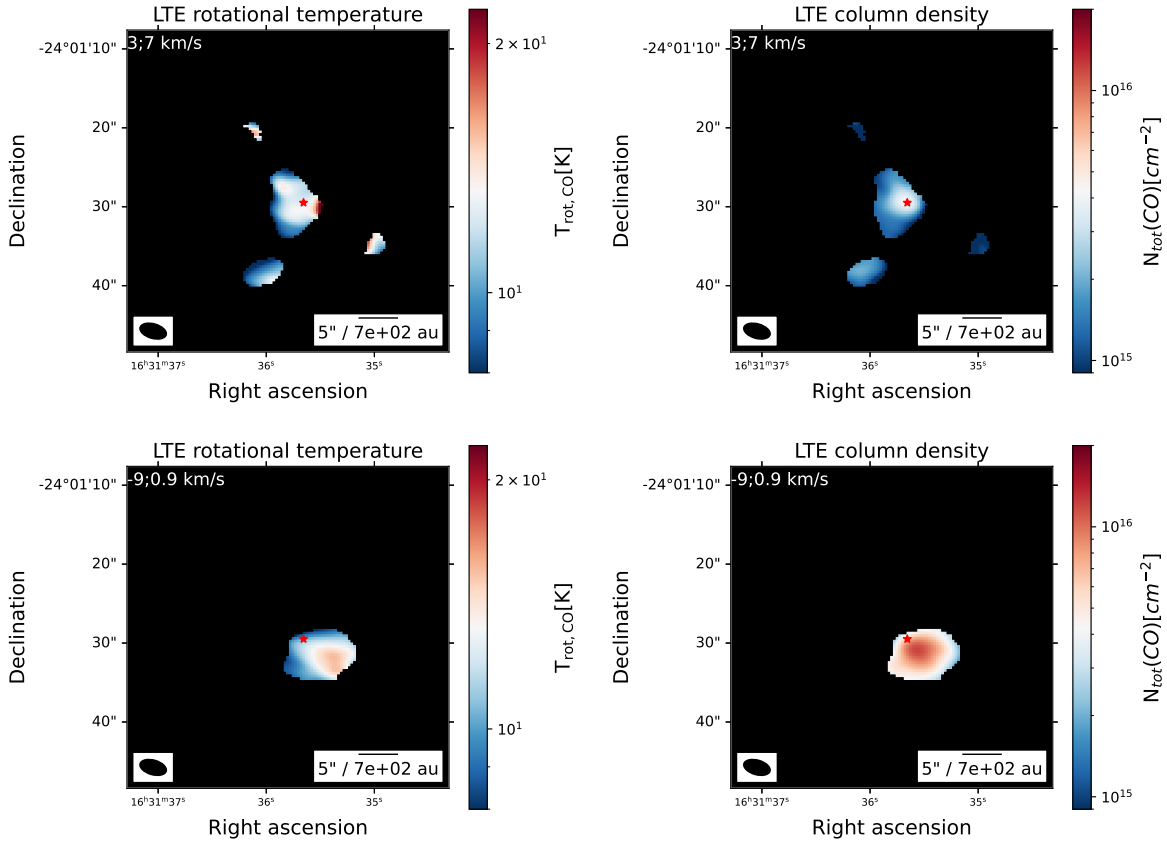


Figure A.6: T_{rot} and $N_{\text{tot}}(\text{CO})$ maps for Oph 34. The upper plots indicate the red-shifted lobes, integrated between 3.0 and 7.0 km s⁻¹. The lower plots indicate the blue-shifted lobes, integrated between -9.0 and 0.9 km s⁻¹. The beam size is indicated in the bottom left of each figure, a scale bar is indicated in the bottom right of each figure. 2MASS sources identified as YSO are indicated as red stars (Skrutskie et al., 2006; Pattle & Ward-Thompson, 2015).

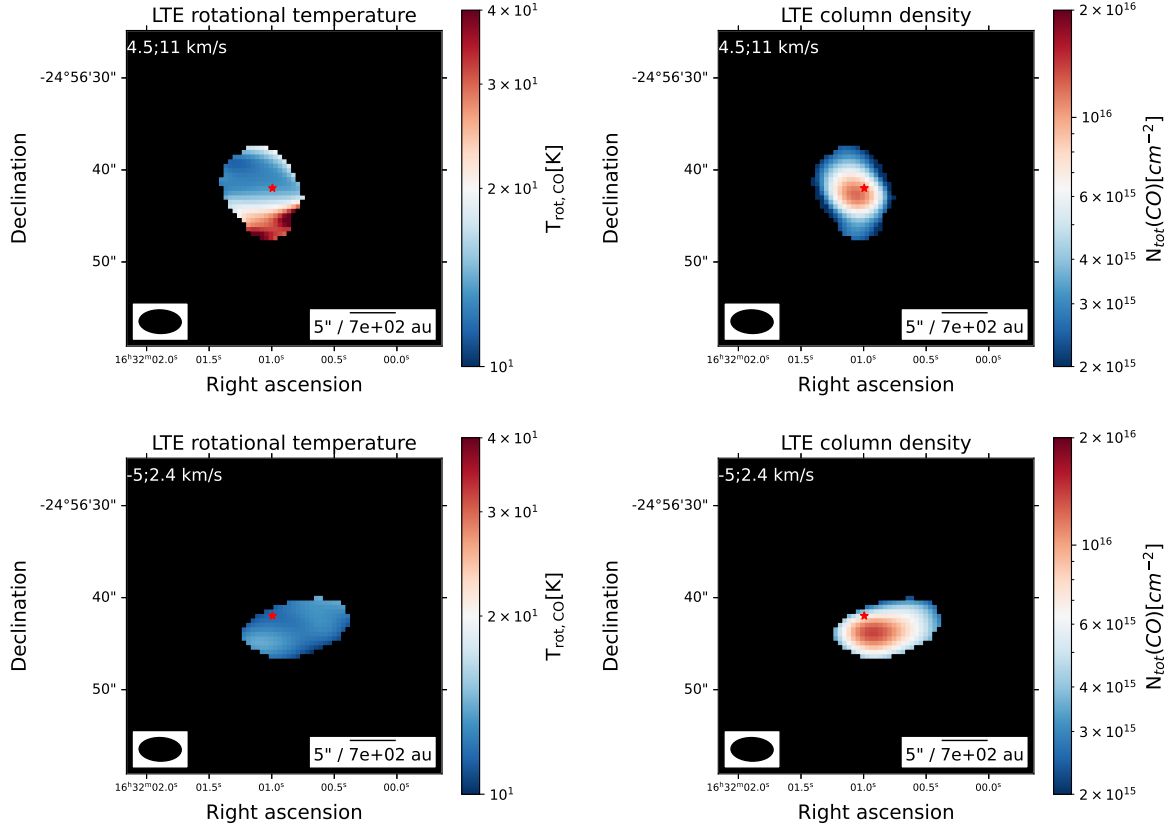


Figure A.7: T_{rot} and $N_{\text{tot}}(\text{CO})$ maps for Oph 39. The upper plots indicate the red-shifted lobes, integrated between 4.5 and 11.0 km s $^{-1}$. The lower plots indicate the blue-shifted lobes, integrated between -5.0 and 2.4 km s $^{-1}$. The beam size is indicated in the bottom left of each figure, a scale bar is indicated in the bottom right of each figure. 2MASS sources identified as YSO are indicated as red stars (Skrutskie et al., 2006; Connelley & Greene, 2010).

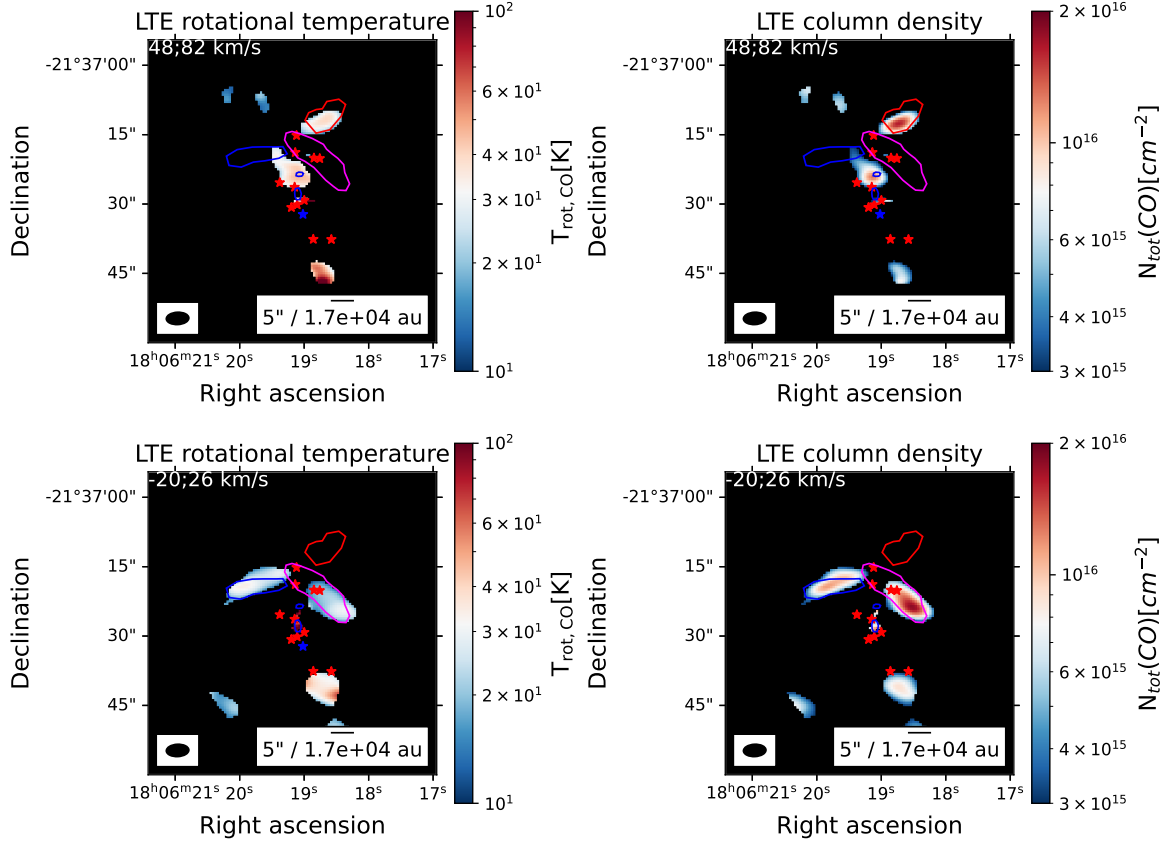


Figure A.8: T_{rot} and $N_{\text{tot(CO)}}$ maps for G008.67. The upper plots indicate the red-shifted lobes, integrated between 48 and 82 km s⁻¹. The lower plots indicate the blue-shifted lobes, integrated between -20 and 26 km s⁻¹. The beam size is indicated in the bottom left of each figure, a scale bar is indicated in the bottom right of each figure. SiO-identified outflows are indicated in red and blue for red-shifted and blue-shifted outflows, bipolar SiO-identified outflows are indicated in pink (Towner et al., 2023). Hot cores (Bonfand et al., 2024) are indicated as blue stars, while continuum cores (Cunningham et al., 2023) are indicated as red stars. Pixels are masked out if $T_{\text{rot}} < 1\text{K}$ or $T_{\text{rot}} > 200\text{K}$. We suspect that the majority of pixels is optically thick in the CO (2-1) line, therefore we treat derived temperatures as upper limits and derived column densities as lower limits.

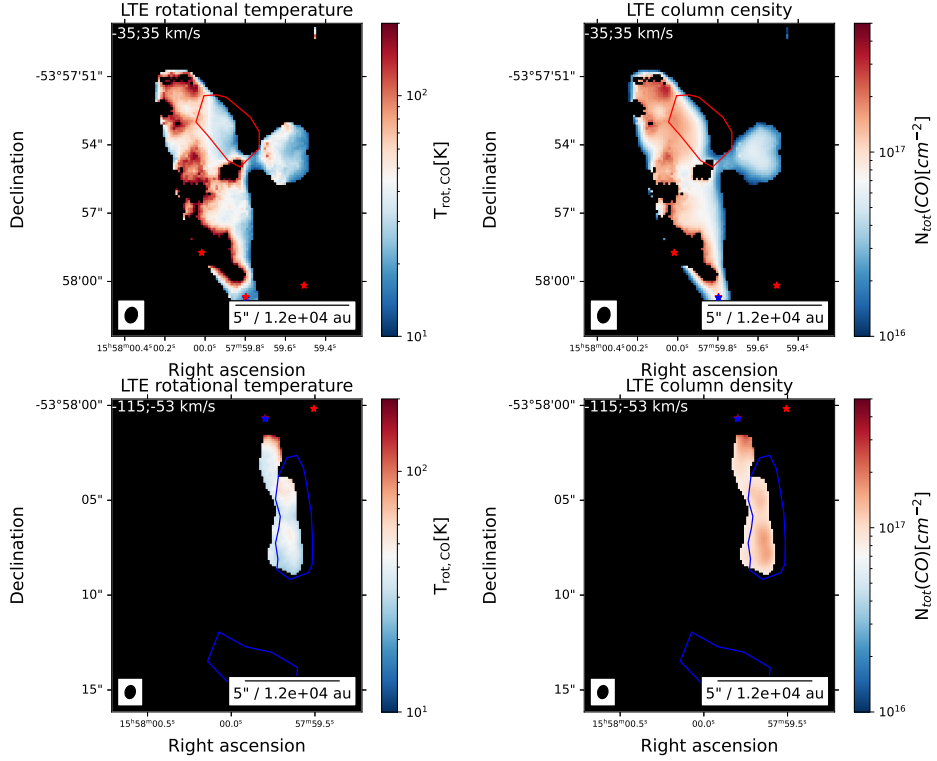


Figure A.9: T_{rot} and $N_{\text{tot}}(\text{CO})$ maps for G328.25. The upper plots indicate the red-shifted lobes, integrated between -35 and 35 km s^{-1} . The lower plots indicate the blue-shifted lobes, integrated between -115 and 53 km s^{-1} . The beam size is indicated in the bottom left of each figure, a scale bar is indicated in the bottom right of each figure. SiO-identified outflows are indicated in red and blue for red-shifted and blue-shifted outflows, bipolar SiO-identified outflows are indicated in pink (Towner et al., 2023). Hot cores (Bonfand et al., 2024) are indicated as blue stars, while continuum cores (Cunningham et al., 2023) are indicated as red stars. Pixels are masked out if $T_{\text{rot}} < 1 \text{ K}$ or $T_{\text{rot}} > 200 \text{ K}$. We suspect that the majority of pixels is optically thick in the CO (2-1) line, therefore we treat derived temperatures as upper limits and derived column densities as lower limits.

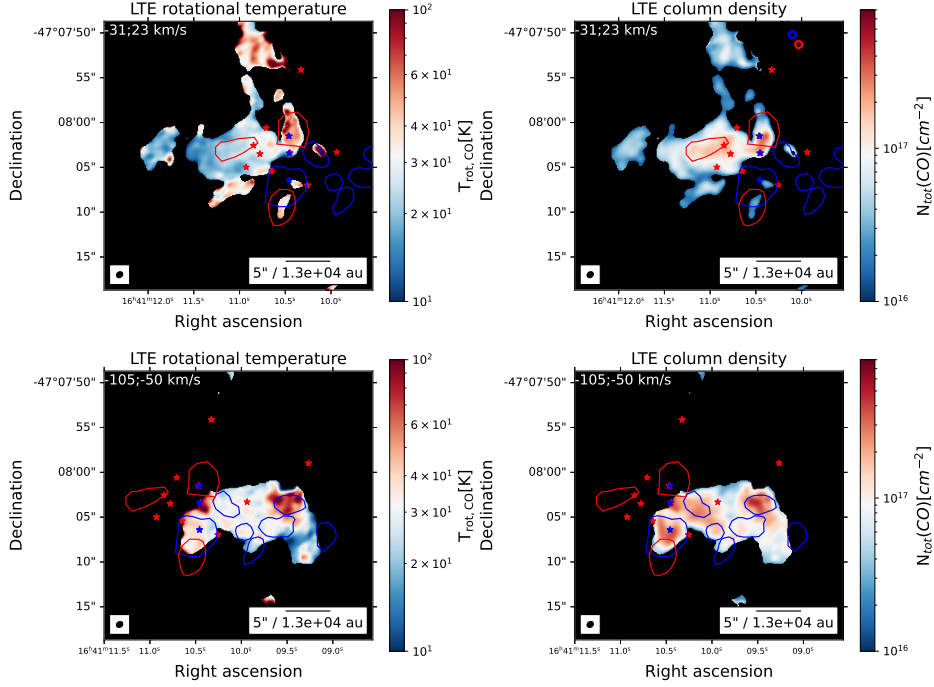


Figure A.10: T_{rot} and $N_{\text{tot}}(\text{CO})$ maps for G337.92. The upper plots indicate the red-shifted lobes, integrated between -31 and 23 km s^{-1} . The lower plots indicate the blue-shifted lobes, integrated between -105 and -50 km s^{-1} . The beam size is indicated in the bottom left of each figure, a scale bar is indicated in the bottom right of each figure. SiO-identified outflows are indicated in red and blue for red-shifted and blue-shifted outflows, bipolar SiO-identified outflows are indicated in pink (Towner et al., 2023). Hot cores (Bonfand et al., 2024) are indicated as blue stars, while continuum cores (Cunningham et al., 2023) are indicated as red stars. Pixels are masked out if $T_{\text{rot}} < 1 \text{ K}$ or $T_{\text{rot}} > 200 \text{ K}$. We suspect that the majority of pixels is optically thick in the CO (2-1) line, therefore we treat derived temperatures as upper limits and derived column densities as lower limits.

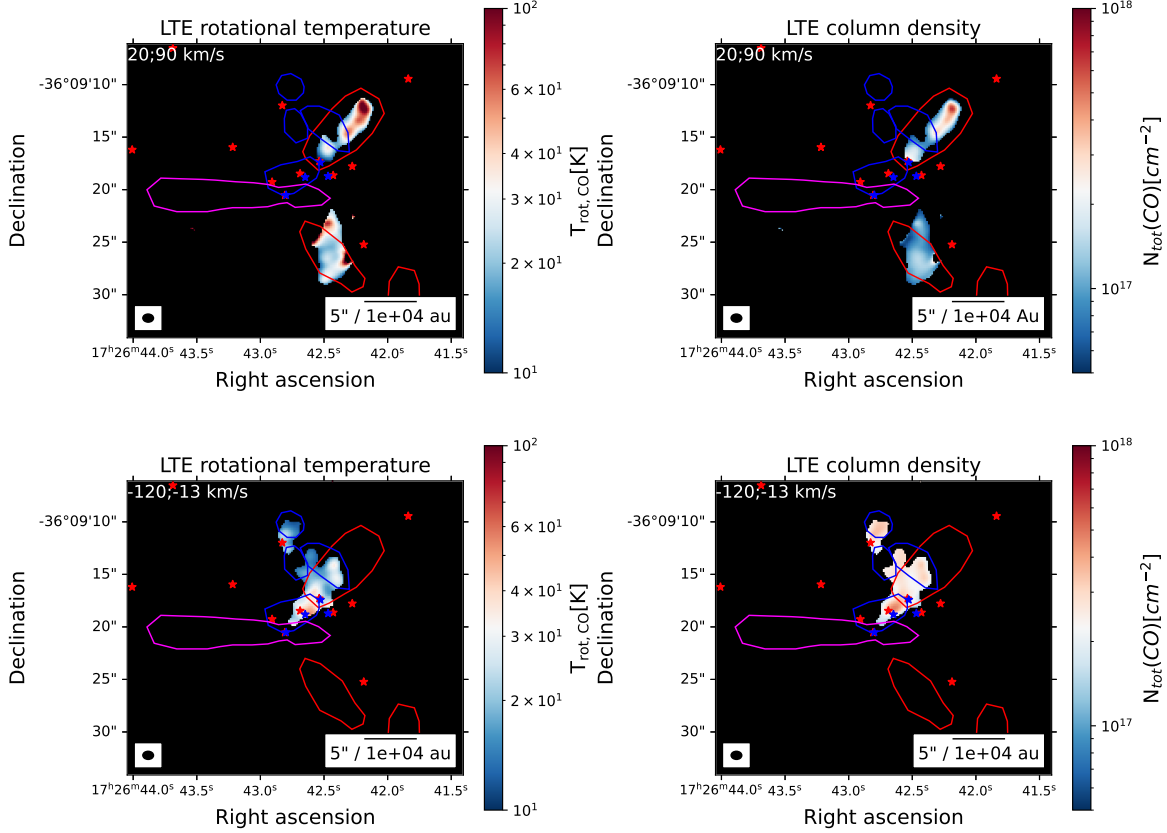


Figure A.11: T_{rot} and $N_{\text{tot}}(\text{CO})$ maps for G351.77. The upper plots indicate the red-shifted lobes, integrated between 20 and 90 km s^{-1} . The lower plots indicate the blue-shifted lobes, integrated between -120 and -13 km s^{-1} . The beam size is indicated in the bottom left of each figure, a scale bar is indicated in the bottom right of each figure. SiO-identified outflows are indicated in red and blue for red-shifted and blue-shifted outflows, bipolar SiO-identified outflows are indicated in pink (Towner et al., 2023). Hot cores (Bonfand et al., 2024) are indicated as blue stars, while continuum cores (Cunningham et al., 2023) are indicated as red stars. Pixels are masked out if $T_{\text{rot}} < 1 \text{ K}$ or $T_{\text{rot}} > 200 \text{ K}$. We suspect that the majority of pixels is optically thick in the CO (2-1) line, therefore we treat derived temperatures as upper limits and derived column densities as lower limits.

A.3 Opening angle determination

Below, we show the determination of the opening angle α of all sources in our low- and high-mass sample, as described in Chapter 4. Not indicated are G328.25 (see Figure 4.1) and Oph 26 (see Figure 4.2).

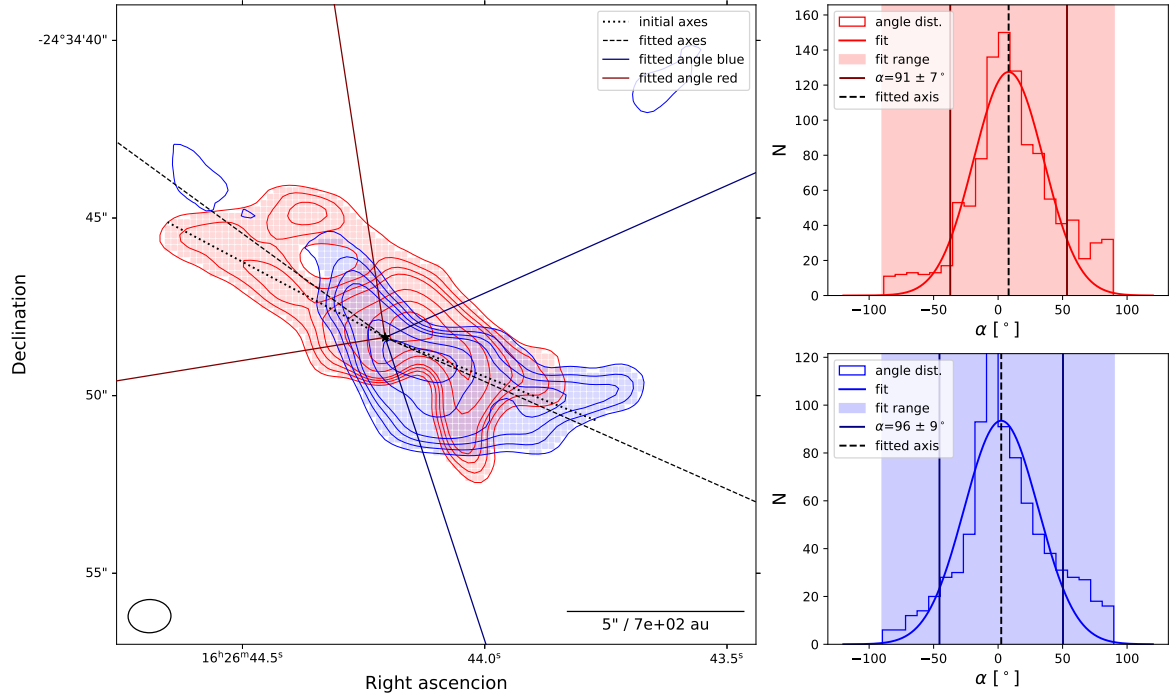


Figure A.12: Left: Integrated blue- and red-shifted CO (2-1) emission showing the Oph 12 outflow, integrated over the velocity interval reported in Table 3.1. The contour levels are at 3σ , 4σ , 5σ , 6σ , and then at intervals of 3σ . The initial axes, indicated as dotted lines, are the axes used to determine the radii of the outflow. The pixels in the shaded areas are included in determining the opening angles. The fitted opening angles are indicated as solid lines, relative to the fitted axis indicated as a dashed line. The position of the YSO is indicated as a black star. Right: The histograms of the angle distributions used to determine the opening angles of the outflow, to which a Gaussian distribution is fitted. The shaded regions indicate which bins were included in the fitting. The fitted axes are indicated as dashed lines, and the fitted opening angles are indicated as solid lines.

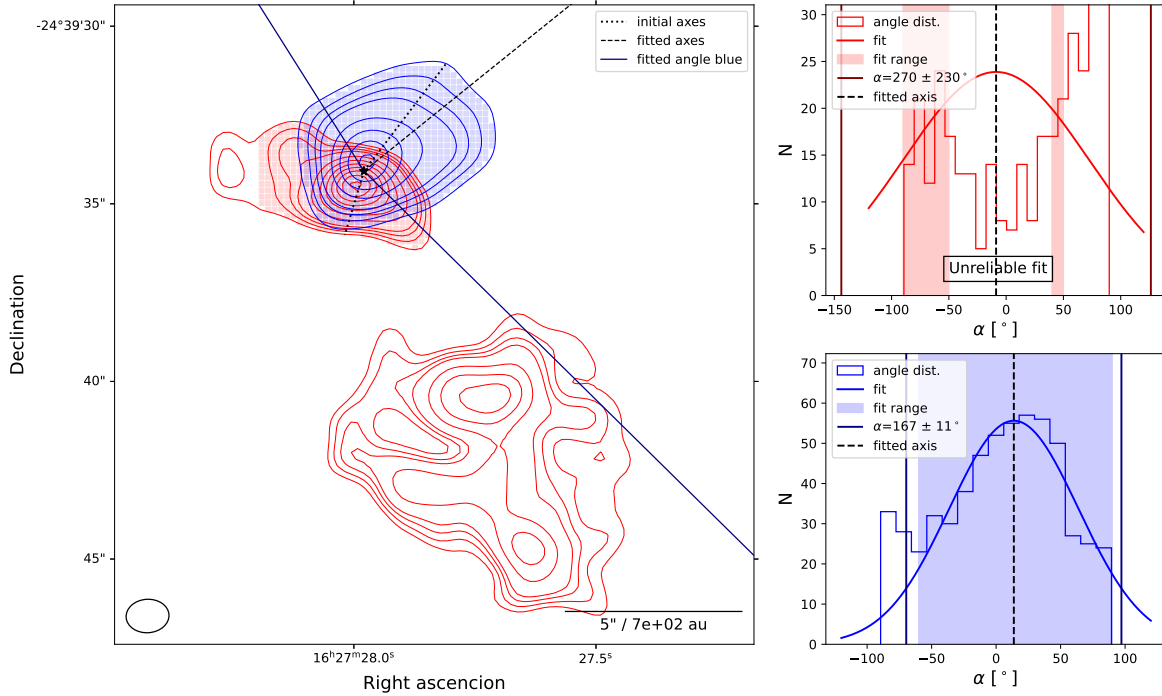


Figure A.13: Left: Integrated blue- and red-shifted CO (2-1) emission showing the Oph 27 outflow, integrated over the velocity interval reported in Table 3.1. The contour levels are at 3σ , 4σ , 5σ , 6σ , and then at intervals of 3σ . The initial axes, indicated as dotted lines, are the axes used to determine the radii of the outflow. The pixels in the shaded areas are included in determining the opening angles. The fitted opening angles are indicated as solid lines, relative to the fitted axis indicated as a dashed line. The position of the YSO is indicated as a black star. Right: The histograms of the angle distributions used to determine the opening angles of the outflow, to which a Gaussian distribution is fitted. The shaded regions indicate which bins were included in the fitting. The fitted axes are indicated as dashed lines, and the fitted opening angles are indicated as solid lines. For the red lobe, no reliable fit could be achieved.

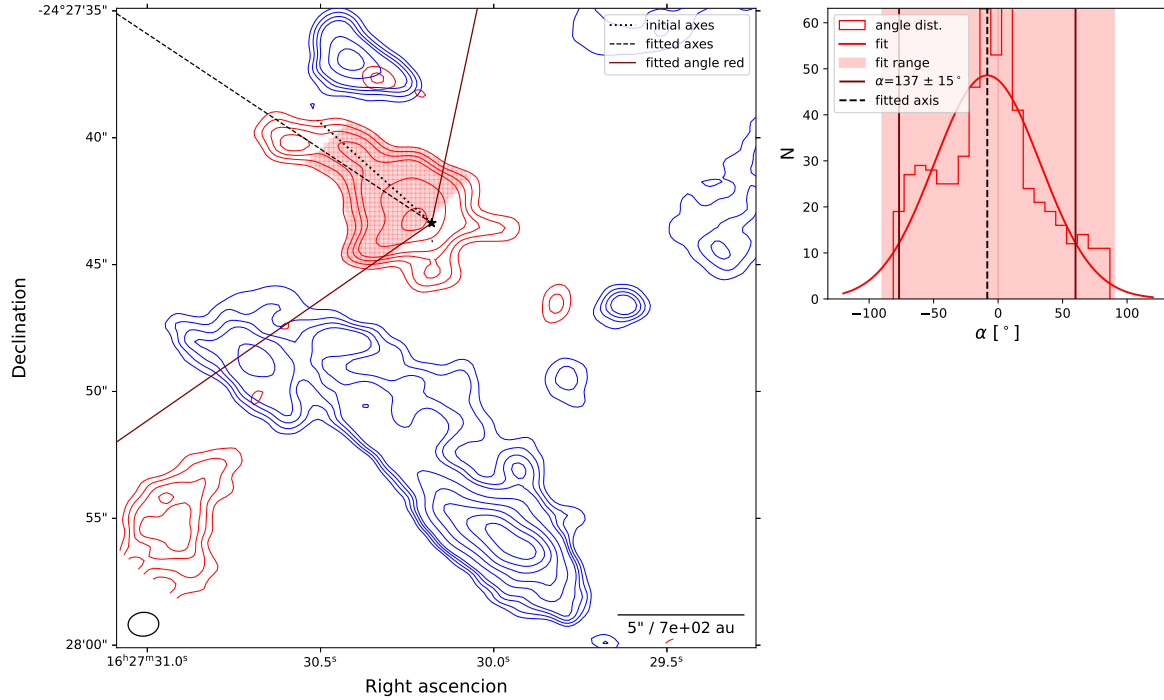


Figure A.14: Left: Integrated blue- and red-shifted CO (2-1) emission showing the Oph 29 outflow, integrated over the velocity interval reported in Table 3.1. The contour levels are at 3σ , 4σ , 5σ , 6σ , and then at intervals of 3σ . The initial axes, indicated as dotted lines, are the axes used to determine the radii of the outflow. The pixels in the shaded areas are included in determining the opening angles. The fitted opening angles are indicated as solid lines, relative to the fitted axis indicated as a dashed line. The position of the YSO is indicated as a black star. Right: The histogram of the angle distribution used to determine the opening angle of the outflow, to which a Gaussian distribution is fitted. For this source, only the opening angle of the red lobe was determined. The shaded region indicates which bins were included in the fitting. The fitted axis is indicated as a dashed line, and the fitted opening angle is indicated as a solid line.

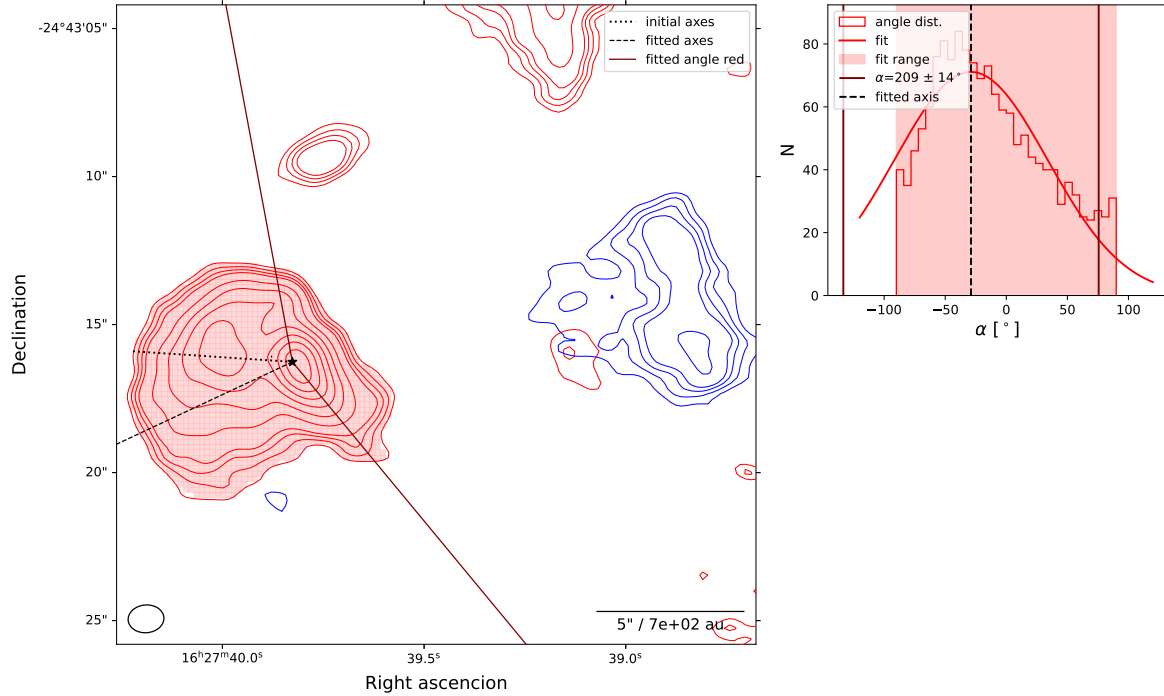


Figure A.15: Left: Integrated blue- and red-shifted CO (2-1) emission showing the Oph 31 outflow, integrated over the velocity interval reported in Table 3.1. The contour levels are at 3σ , 4σ , 5σ , 6σ , and then at intervals of 3σ . The initial axes, indicated as dotted lines, are the axes used to determine the radii of the outflow. The pixels in the shaded areas are included in determining the opening angles. The fitted opening angles are indicated as solid lines, relative to the fitted axis indicated as a dashed line. The position of the YSO is indicated as a black star. Right: The histogram of the angle distribution used to determine the opening angle of the outflow, to which a Gaussian distribution is fitted. For this source, only the opening angle of the red lobe was determined. The shaded region indicates which bins were included in the fitting. The fitted axis is indicated as a dashed line, and the fitted opening angle is indicated as a solid line.

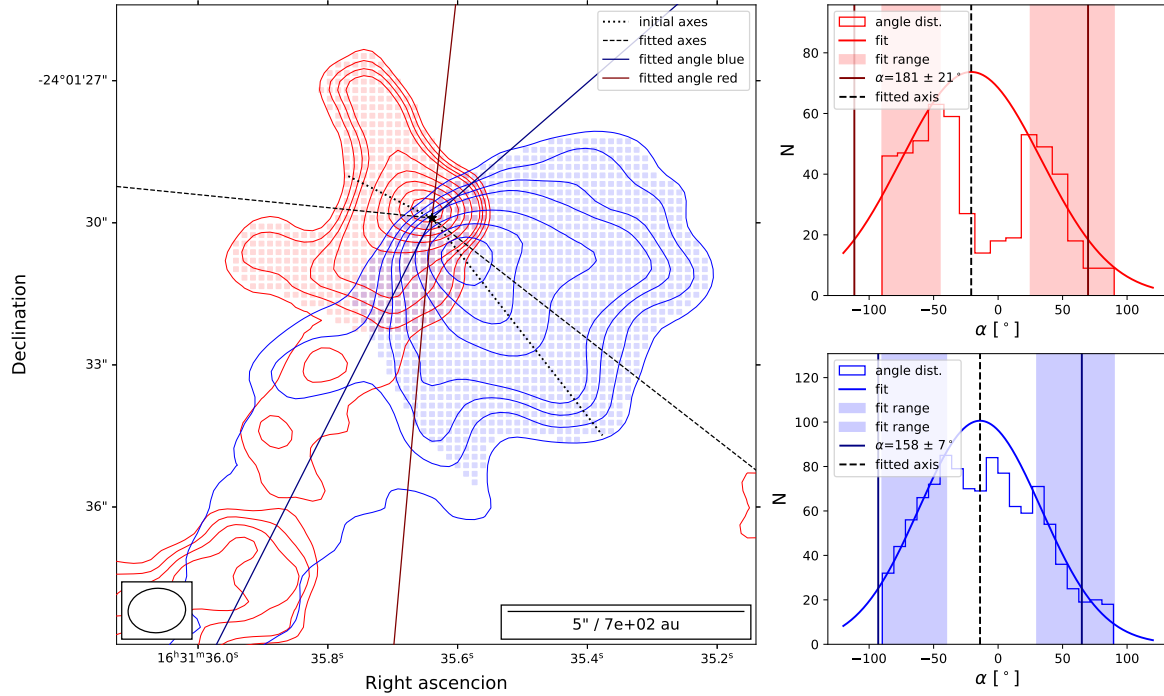


Figure A.16: Left: Integrated blue- and red-shifted CO (2-1) emission showing the Oph 34 outflow, integrated over the velocity interval reported in Table 3.1. The contour levels are at 3σ , 4σ , 5σ , 6σ , and then at intervals of 3σ . The initial axes, indicated as dotted lines, are the axes used to determine the radii of the outflow. The pixels in the shaded areas are included in determining the opening angles. The fitted opening angles are indicated as solid lines, relative to the fitted axis indicated as a dashed line. The position of the YSO is indicated as a black star. Right: The histograms of the angle distributions used to determine the opening angles of the outflow, to which a Gaussian distribution is fitted. The shaded regions indicate which bins were included in the fitting. For this source, a cavity was masked out from both lobes. The fitted axes are indicated as dashed lines, and the fitted opening angles are indicated as solid lines.

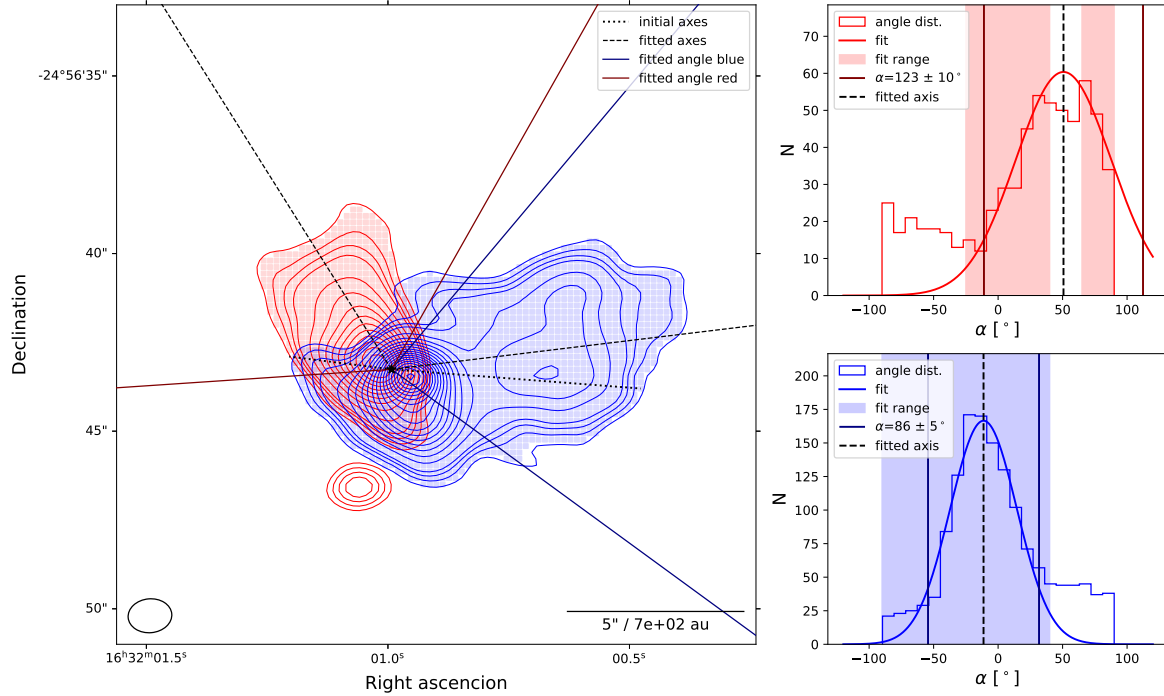


Figure A.17: Left: Integrated blue- and red-shifted CO (2-1) emission showing the Oph 39 outflow, integrated over the velocity interval reported in Table 3.1. The contour levels are at 3σ , 4σ , 5σ , 6σ , and then at intervals of 3σ . The initial axes, indicated as dotted lines, are the axes used to determine the radii of the outflow. The pixels in the shaded areas are included in determining the opening angles. The fitted opening angles are indicated as solid lines, relative to the fitted axis indicated as a dashed line. The position of the YSO is indicated as a black star. Right: The histograms of the angle distributions used to determine the opening angles of the outflow, to which a Gaussian distribution is fitted. The shaded regions indicate which bins were included in the fitting. For this source, a cavity was excluded from the red lobe. The fitted axes are indicated as dashed lines, and the fitted opening angles are indicated as solid lines.

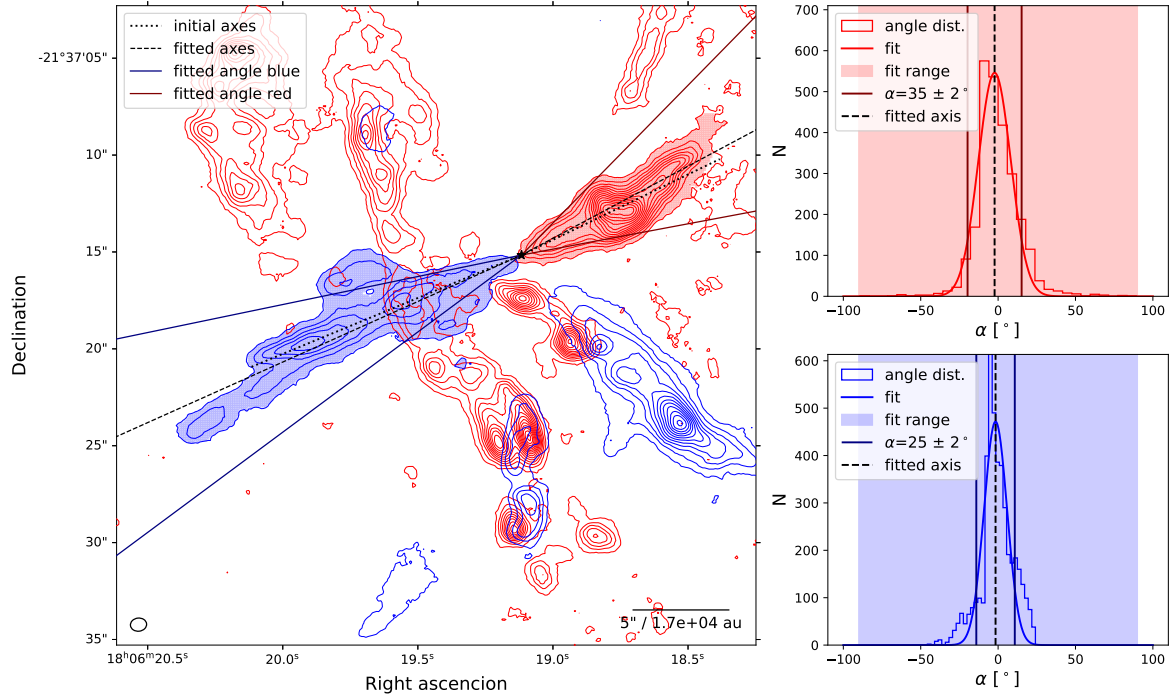


Figure A.18: Left: Integrated blue- and red-shifted CO (2-1) emission showing the G008.67_A outflow, integrated over the velocity interval reported in Table 3.1. Contour levels start at 3σ , and are then at intervals of 5σ . The initial axes, indicated as dotted lines, are the axes used to determine the radii of the outflow. The pixels in the shaded areas are included in determining the opening angles. The fitted opening angles are indicated as solid lines, relative to the fitted axis indicated as a dashed line. The position of the YSO is indicated as a black star. Right: The histograms of the angle distributions used to determine the opening angles of the outflow, to which a Gaussian distribution is fitted. The shaded regions indicate which bins were included in the fitting. The fitted axes are indicated as dashed lines, and the fitted opening angles are indicated as solid lines.

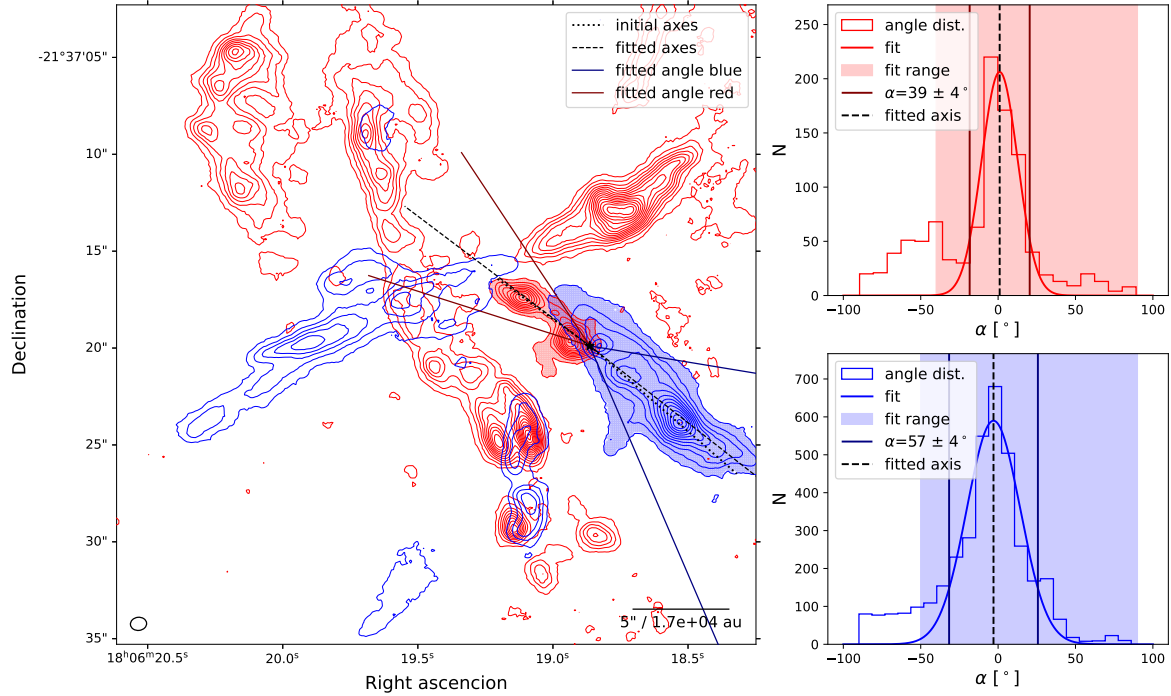


Figure A.19: Left: Integrated blue- and red-shifted CO (2-1) emission showing the G008.67_B outflow, integrated over the velocity interval reported in Table 3.1. Contour levels start at 3σ , and are then at intervals of 5σ . The initial axes, indicated as dotted lines, are the axes used to determine the radii of the outflow. The pixels in the shaded areas are included in determining the opening angles. The fitted opening angles are indicated as solid lines, relative to the fitted axis indicated as a dashed line. The position of the YSO is indicated as a black star. Right: The histograms of the angle distributions used to determine the opening angles of the outflow, to which a Gaussian distribution is fitted. The shaded regions indicate which bins were included in the fitting. The fitted axes are indicated as dashed lines, and the fitted opening angles are indicated as solid lines.

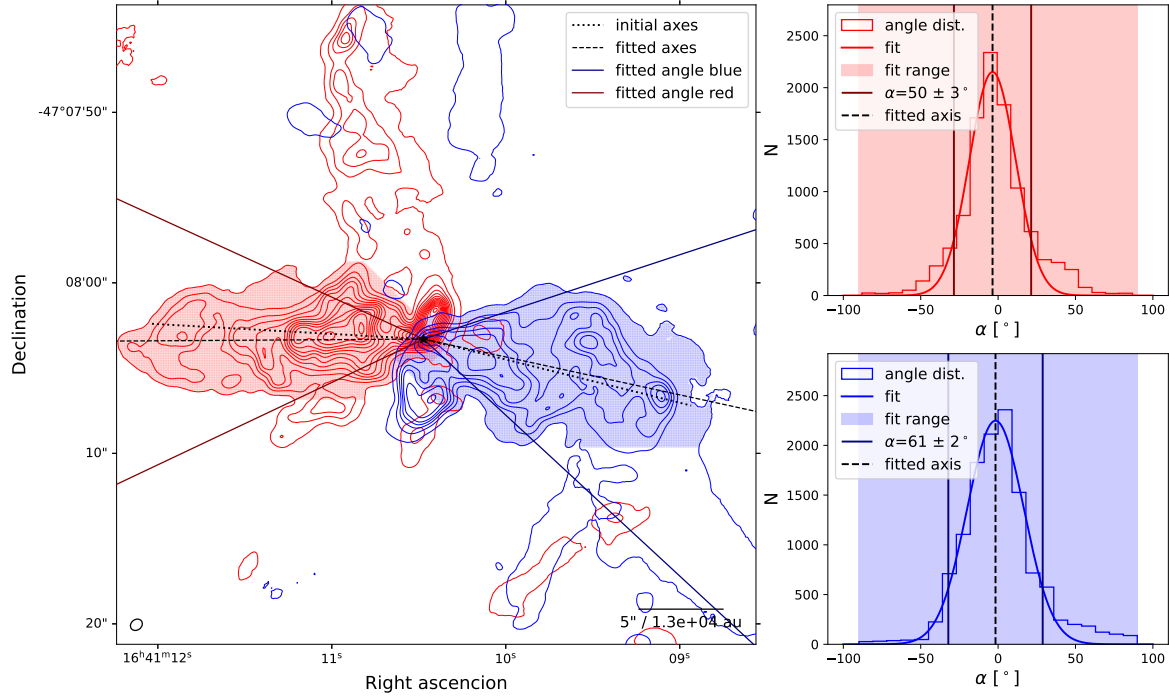


Figure A.20: Left: Integrated blue- and red-shifted CO (2-1) emission showing the G337.92 outflow, integrated over the velocity interval reported in Table 3.1. The red contour levels start at 3σ , and are then at intervals of 10σ . The blue contour levels start at 3σ , and then at intervals of 20σ . The initial axes, indicated as dotted lines, are the axes used to determine the radii of the outflow. The pixels in the shaded areas are included in determining the opening angles. The fitted opening angles are indicated as solid lines, relative to the fitted axis indicated as a dashed line. The position of the YSO is indicated as a black star. Right: The histograms of the angle distributions used to determine the opening angles of the outflow, to which a Gaussian distribution is fitted. The shaded regions indicate which bins were included in the fitting. The fitted axes are indicated as dashed lines, and the fitted opening angles are indicated as solid lines.

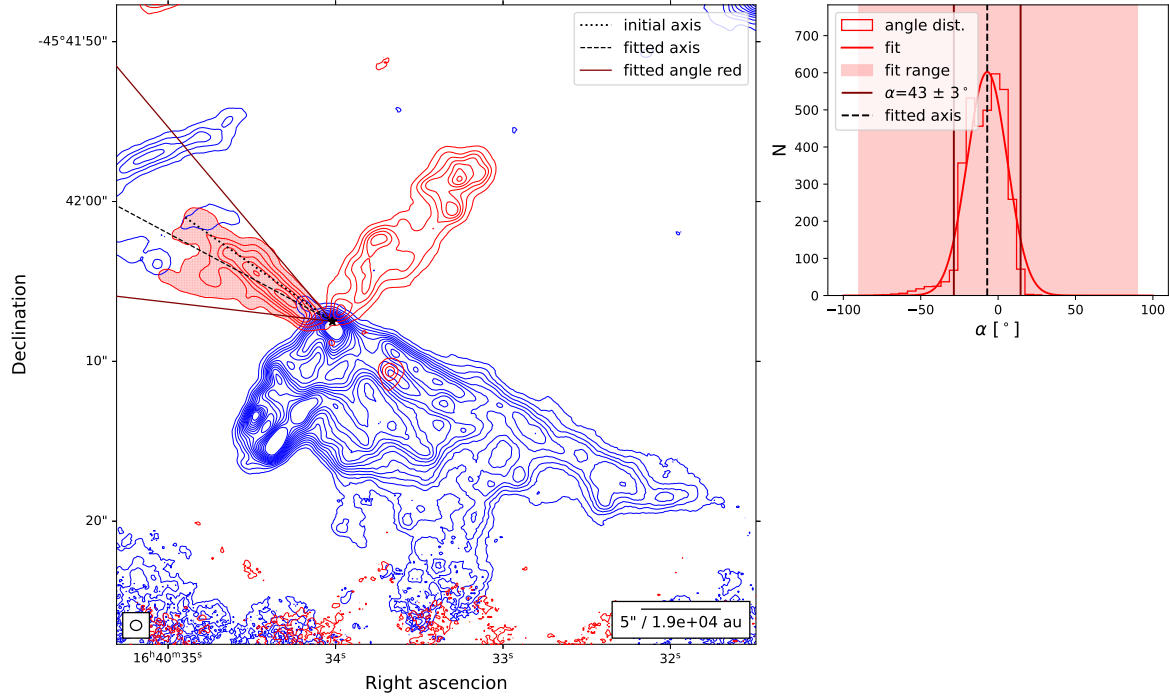


Figure A.21: Left: Integrated blue- and red-shifted CO (2-1) emission showing the G338.93 α outflow, integrated over the velocity interval reported in Table 3.1. The contour levels start at 3σ , and are then at intervals of 5σ . The initial axes, indicated as dotted lines, are the axes used to determine the radii of the outflow. The pixels in the shaded areas are included in determining the opening angles. The fitted opening angles are indicated as solid lines, relative to the fitted axis indicated as a dashed line. The position of the YSO is indicated as a black star. Right: The histogram of the angle distribution used to determine the opening angle of the outflow, to which a Gaussian distribution is fitted. For this outflow, only the opening angle of the red lobe was determined. The shaded region indicates which bins were included in the fitting. The fitted axis is indicated as a dashed line, and the fitted opening angle is indicated as a solid line.

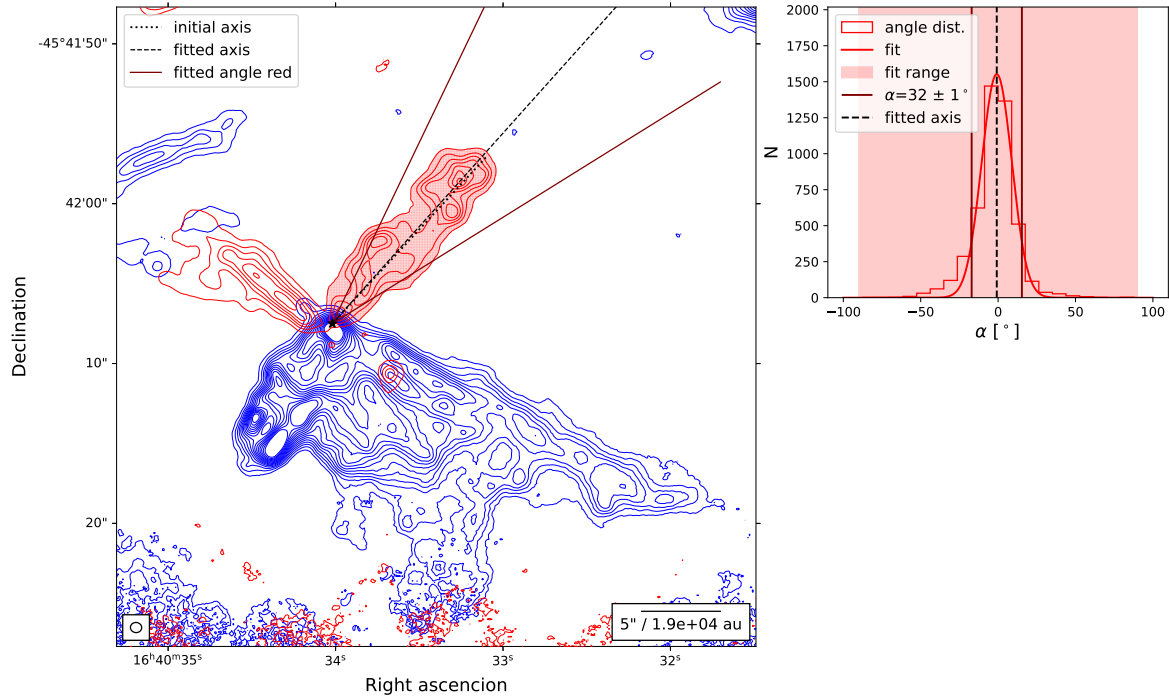


Figure A.22: Left: Integrated blue- and red-shifted CO (2-1) emission showing the G338.93_B outflow, integrated over the velocity interval reported in Table 3.1. The contour levels start at 3σ , and are then at intervals of 5σ . The initial axes, indicated as dotted lines, are the axes used to determine the radii of the outflow. The pixels in the shaded areas are included in determining the opening angles. The fitted opening angles are indicated as solid lines, relative to the fitted axis indicated as a dashed line. The position of the YSO is indicated as a black star. Right: The histogram of the angle distribution used to determine the opening angle of the outflow, to which a Gaussian distribution is fitted. For this outflow, only the opening angle of the red lobe was determined. The shaded region indicates which bins were included in the fitting. The fitted axis is indicated as a dashed line, and the fitted opening angle is indicated as a solid line.

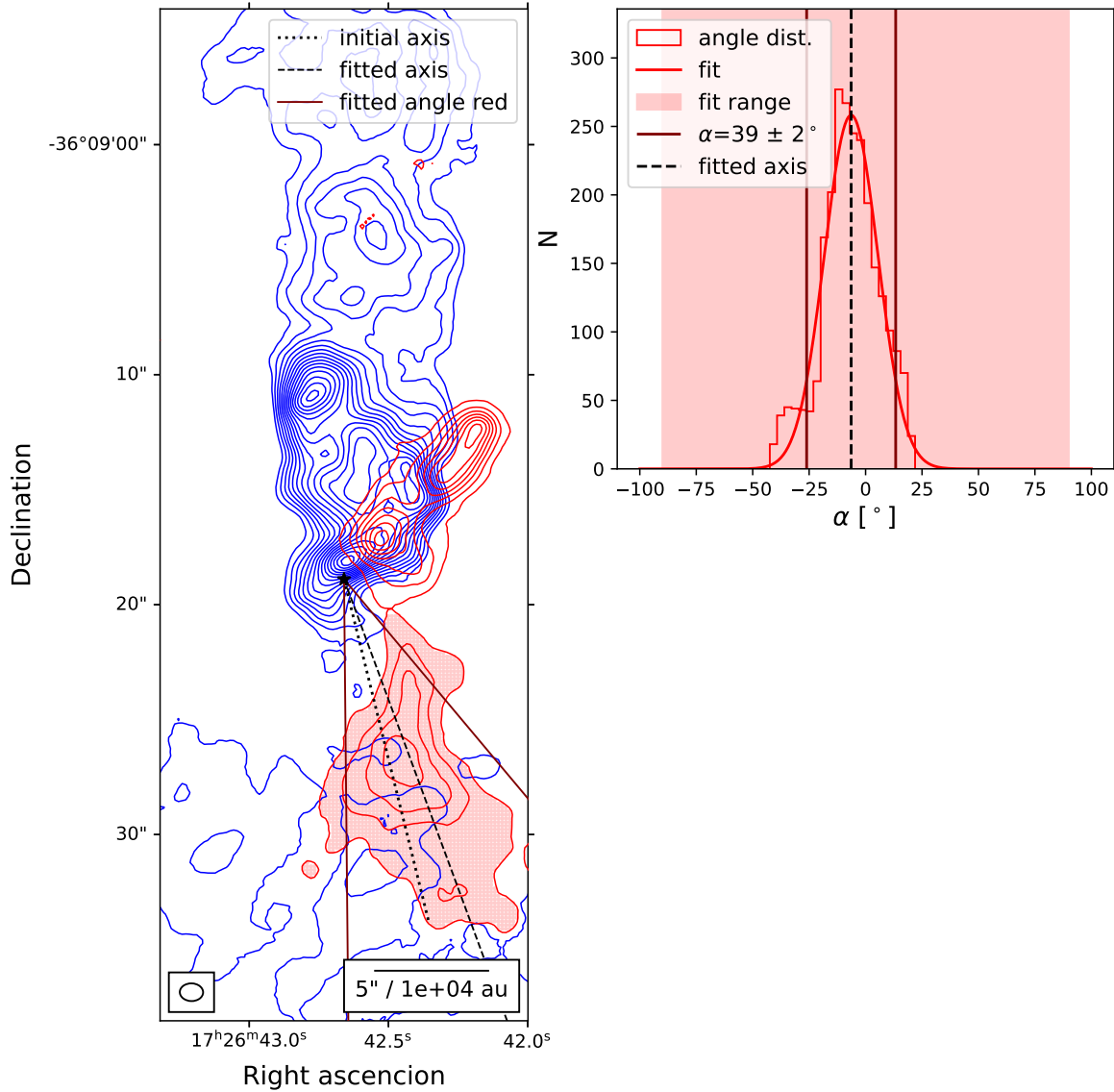


Figure A.23: Left: Integrated blue- and red-shifted CO (2-1) emission showing the G351.77_A outflow, integrated over the velocity interval reported in Table 3.1. The red contour levels start at 3σ , and are then at intervals of 10σ . The blue contour levels start at 3σ , and are then at intervals of 20σ . The initial axes, indicated as dotted lines, are the axes used to determine the radii of the outflow. The pixels in the shaded areas are included in determining the opening angles. The fitted opening angles are indicated as solid lines, relative to the fitted axis indicated as a dashed line. The position of the YSO is indicated as a black star. Right: The histogram of the angle distribution used to determine the opening angle of the outflow, to which a Gaussian distribution is fitted. For this outflow, only the opening angle of the red lobe was determined. The shaded region indicates which bins were included in the fitting. The fitted axis is indicated as a dashed line, and the fitted opening angle is indicated as a solid line.

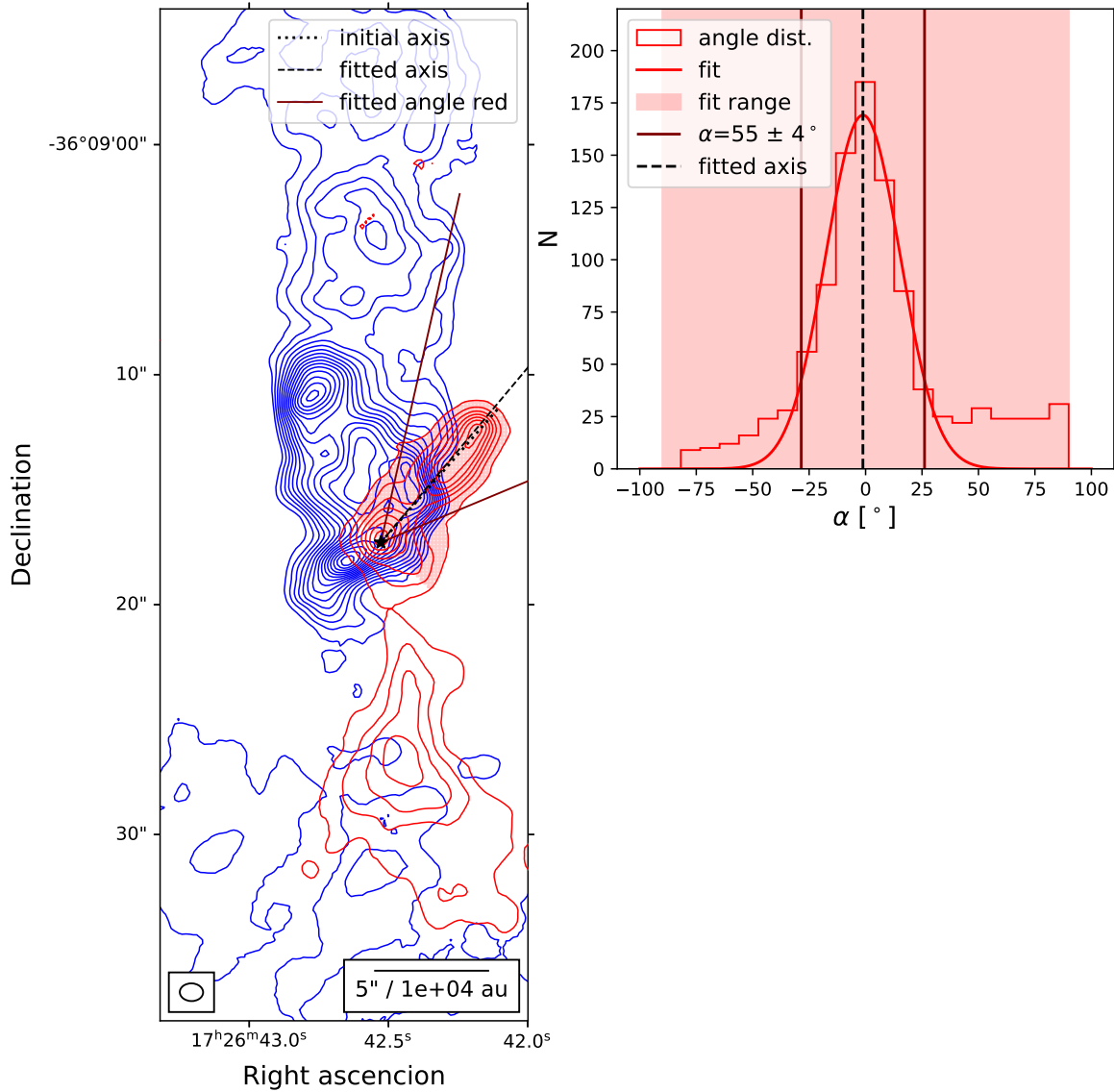


Figure A.24: Left: Integrated blue- and red-shifted CO (2-1) emission showing the G351.77_A outflow, integrated over the velocity interval reported in Table 3.1. The red contour levels start at 3σ , and are then at intervals of 10σ . The blue contour levels start at 3σ , and then at intervals of 20σ . The initial axes, indicated as dotted lines, are the axes used to determine the radii of the outflow. The pixels in the shaded areas are included in determining the opening angles. The fitted opening angles are indicated as solid lines, relative to the fitted axis indicated as a dashed line. The position of the YSO is indicated as a black star. Right: The histogram of the angle distribution used to determine the opening angle of the outflow, to which a Gaussian distribution is fitted. For this outflow, only the opening angle of the red lobe was determined. The shaded region indicates which bins were included in the fitting. The fitted axis is indicated as a dashed line, and the fitted opening angle is indicated as a solid line.

Bibliography

- Alves, J., Lombardi, M., & Lada, C. J. 2007, A&A , 462, L17, doi: [10.1051/0004-6361:20066389](https://doi.org/10.1051/0004-6361:20066389)
- Andre, P., & Montmerle, T. 1994, ApJ , 420, 837, doi: [10.1086/173608](https://doi.org/10.1086/173608)
- Arce, H. G., Borkin, M. A., Goodman, A. A., Pineda, J. E., & Beaumont, C. N. 2011, ApJ , 742, 105, doi: [10.1088/0004-637X/742/2/105](https://doi.org/10.1088/0004-637X/742/2/105)
- Arce, H. G., Mardones, D., Corder, S. A., et al. 2013, The Astrophysical Journal, 774, 39, doi: [10.1088/0004-637x/774/1/39](https://doi.org/10.1088/0004-637x/774/1/39)
- Arce, H. G., & Sargent, A. I. 2006, ApJ , 646, 1070, doi: [10.1086/505104](https://doi.org/10.1086/505104)
- Arce, H. G., Shepherd, D., Gueth, F., et al. 2007, in Protostars and Planets V, ed. B. Reipurth, D. Jewitt, & K. Keil, 245, doi: [10.48550/arXiv.astro-ph/0603071](https://arxiv.org/abs/astro-ph/0603071)
- Bachiller, R. 1996, Annual Review of Astronomy and Astrophysics, 34, 111–154, doi: [10.1146/annurev.astro.34.1.111](https://doi.org/10.1146/annurev.astro.34.1.111)
- Bally, J. 2016, Annual Review of Astronomy and Astrophysics, 54, 491–528, doi: [10.1146/annurev-astro-081915-023341](https://doi.org/10.1146/annurev-astro-081915-023341)
- Bally, J., & Lada, C. J. 1983, ApJ , 265, 824, doi: [10.1086/160729](https://doi.org/10.1086/160729)
- Beuther, H., Schilke, P., Sridharan, T. K., et al. 2002, A&A , 383, 892, doi: [10.1051/0004-6361:20011808](https://doi.org/10.1051/0004-6361:20011808)
- Beuther, H., & Shepherd, D. 2005, in Astrophysics and Space Science Library, Vol. 324, Astrophysics and Space Science Library, ed. M. S. N. Kumar, M. Tafalla, & P. Caselli, 105, doi: [10.1007/0-387-26357-8_8](https://doi.org/10.1007/0-387-26357-8_8)
- Billot, N., Morales-Calderón, M., Stauffer, J. R., Megeath, S. T., & Whitney, B. 2012, ApJL , 753, L35, doi: [10.1088/2041-8205/753/2/L35](https://doi.org/10.1088/2041-8205/753/2/L35)
- Blake, G. A., Sandell, G., van Dishoeck, E. F., et al. 1995, ApJ , 441, 689, doi: [10.1086/175392](https://doi.org/10.1086/175392)
- Bonfand, M., Csengeri, T., Bontemps, S., et al. 2024, Astronomy & Astrophysics, 687, A163, doi: [10.1051/0004-6361/202347856](https://doi.org/10.1051/0004-6361/202347856)

- Bonnell, I. A., Bate, M. R., Clarke, C. J., & Pringle, J. E. 2001, MNRAS , 323, 785, doi: [10.1046/j.1365-8711.2001.04270.x](https://doi.org/10.1046/j.1365-8711.2001.04270.x)
- Bonnell, I. A., Bate, M. R., & Zinnecker, H. 1998, MNRAS , 298, 93, doi: [10.1046/j.1365-8711.1998.01590.x](https://doi.org/10.1046/j.1365-8711.1998.01590.x)
- Bontemps, S., Andre, P., Terebey, S., & Cabrit, S. 1996, A&A , 311, 858
- Bontemps, S., André, P., Kaas, A. A., et al. 2001, Astronomy & Astrophysics, 372, 173–194, doi: [10.1051/0004-6361:20010474](https://doi.org/10.1051/0004-6361:20010474)
- Braatz, J., Biggs, A., Sanhueza, P., & Corvillon, A. 2021, ALMA Cycle 8 2021 Proposer's Guide (ALMA). <https://almascience.nrao.edu/documents-and-tools/cycle8/alma-proposers-guide>
- Cabrit, S., Raga, A., & Gueth, F. 1997, in IAU Symposium, Vol. 182, Herbig-Haro Flows and the Birth of Stars, ed. B. Reipurth & C. Bertout, 163–180
- Caselli, P., Hartquist, T. W., & Havnes, O. 1997, A&A , 322, 296
- Chabrier, G. 2003, PASP , 115, 763, doi: [10.1086/376392](https://doi.org/10.1086/376392)
- Comrie, A., Wang, K.-S., Hwang, Y.-H., et al. 2018, CARTA: The Cube Analysis and Rendering Tool for Astronomy, Zenodo, doi: [10.5281/zenodo.3377984](https://doi.org/10.5281/zenodo.3377984)
- Connelley, M. S., & Greene, T. P. 2010, AJ , 140, 1214, doi: [10.1088/0004-6256/140/5/1214](https://doi.org/10.1088/0004-6256/140/5/1214)
- Csengeri, T., Bontemps, S., Wyrowski, F., et al. 2017, Astronomy & Astrophysics, 601, A60, doi: [10.1051/0004-6361/201628254](https://doi.org/10.1051/0004-6361/201628254)
- Cunningham, A. J., Krumholz, M. R., McKee, C. F., & Klein, R. I. 2018, Monthly Notices of the Royal Astronomical Society, 476, 771–792, doi: [10.1093/mnras/sty154](https://doi.org/10.1093/mnras/sty154)
- Cunningham, N., Ginsburg, A., Galván-Madrid, R., et al. 2023, Astronomy & Astrophysics, 678, A194, doi: [10.1051/0004-6361/202245429](https://doi.org/10.1051/0004-6361/202245429)
- Deil, C., & Ginsburg, A. 2024, reproject 0.14.0. <https://pypi.org/project/reproject/>
- Downes, T. P., & Cabrit, S. 2007, A&A , 471, 873, doi: [10.1051/0004-6361:20066921](https://doi.org/10.1051/0004-6361:20066921)
- Dunham, M. M., Arce, H. G., Mardones, D., et al. 2014, ApJ , 783, 29, doi: [10.1088/0004-637X/783/1/29](https://doi.org/10.1088/0004-637X/783/1/29)
- Dunham, M. M., Stephens, I. W., Myers, P. C., et al. 2024, Monthly Notices of the Royal Astronomical Society, 533, 3828–3861, doi: [10.1093/mnras/stae2018](https://doi.org/10.1093/mnras/stae2018)
- Dunne, L., Eales, S., Ivison, R., Morgan, H., & Edmunds, M. 2003, Nature , 424, 285, doi: [10.1038/nature01792](https://doi.org/10.1038/nature01792)

- Edwards, S., & Snell, R. L. 1982, *ApJ*, 261, 151, doi: [10.1086/160326](https://doi.org/10.1086/160326)
- . 1983, *ApJ*, 270, 605, doi: [10.1086/161152](https://doi.org/10.1086/161152)
- . 1984, *ApJ*, 281, 237, doi: [10.1086/162093](https://doi.org/10.1086/162093)
- Ellerbroek, L. E., Podio, L., Kaper, L., et al. 2013, *A&A*, 551, A5, doi: [10.1051/0004-6361/201220635](https://doi.org/10.1051/0004-6361/201220635)
- Endres, C. P., Schlemmer, S., Schilke, P., Stutzki, J., & Müller, H. S. 2016, *Journal of Molecular Spectroscopy*, 327, 95–104, doi: [10.1016/j.jms.2016.03.005](https://doi.org/10.1016/j.jms.2016.03.005)
- Enoch, M. L., Evans II, N. J., Sargent, A. I., et al. 2008, *The Astrophysical Journal*, 684, 1240–1259, doi: [10.1086/589963](https://doi.org/10.1086/589963)
- Fall, S. M., Krumholz, M. R., & Matzner, C. D. 2010, *ApJL*, 710, L142, doi: [10.1088/2041-8205/710/2/L142](https://doi.org/10.1088/2041-8205/710/2/L142)
- Gibb, A. G., Richer, J. S., Chandler, C. J., & Davis, C. J. 2004, *The Astrophysical Journal*, 603, 198–212, doi: [10.1086/381309](https://doi.org/10.1086/381309)
- Greene, T. P., Wilking, B. A., Andre, P., Young, E. T., & Lada, C. J. 1994, *The Astrophysical Journal*, 434, 614, doi: [10.1086/174763](https://doi.org/10.1086/174763)
- Gusdorf, A., Pineau Des Forêts, G., Cabrit, S., & Flower, D. R. 2008, *A&A*, 490, 695, doi: [10.1051/0004-6361:200810443](https://doi.org/10.1051/0004-6361:200810443)
- Hansen, C. E., Klein, R. I., McKee, C. F., & Fisher, R. T. 2012, *The Astrophysical Journal*, 747, 22, doi: [10.1088/0004-637x/747/1/22](https://doi.org/10.1088/0004-637x/747/1/22)
- Harris, C. R., Millman, K. J., van der Walt, S. J., et al. 2020, *Nature*, 585, 357, doi: [10.1038/s41586-020-2649-2](https://doi.org/10.1038/s41586-020-2649-2)
- Hoang, T. D., Karska, A., Lee, M. Y., et al. 2023, *Astronomy & Astrophysics*, 679, A121, doi: [10.1051/0004-6361/202347163](https://doi.org/10.1051/0004-6361/202347163)
- Hogerheijde, M. 1998, PhD thesis, University of California, Berkeley, Department of Astronomy
- Hunter, J. D. 2007, *Computing in Science & Engineering*, 9, 90, doi: [10.1109/MCSE.2007.55](https://doi.org/10.1109/MCSE.2007.55)
- Könyves, V., André, P., Men'shchikov, A., et al. 2015, *Astronomy & Astrophysics*, 584, A91, doi: [10.1051/0004-6361/201525861](https://doi.org/10.1051/0004-6361/201525861)
- Könyves, V., André, P., Arzoumanian, D., et al. 2020, *Astronomy & Astrophysics*, 635, A34, doi: [10.1051/0004-6361/201834753](https://doi.org/10.1051/0004-6361/201834753)
- Kroupa, P. 2002, *Science*, 295, 82, doi: [10.1126/science.1067524](https://doi.org/10.1126/science.1067524)
- Krumholz, M. R., & Matzner, C. D. 2009, *ApJ*, 703, 1352, doi: [10.1088/0004-637X/703/2/1352](https://doi.org/10.1088/0004-637X/703/2/1352)

- Kuiper, G. P. 1938, *ApJ* , 88, 472, doi: [10.1086/143999](https://doi.org/10.1086/143999)
- Lada, C. J. 1985, *ARA&A* , 23, 267, doi: [10.1146/annurev.aa.23.090185.001411](https://doi.org/10.1146/annurev.aa.23.090185.001411)
- Lada, C. J. 1987, in IAU Symposium, Vol. 115, Star Forming Regions, ed. M. Peimbert & J. Jugaku, 1
- Lada, C. J., & Fich, M. 1996, *ApJ* , 459, 638, doi: [10.1086/176929](https://doi.org/10.1086/176929)
- Lada, C. J., & Lada, E. A. 2003, *ARA&A* , 41, 57, doi: [10.1146/annurev.astro.41.011802.094844](https://doi.org/10.1146/annurev.astro.41.011802.094844)
- Lee, C.-F., & Ho, P. T. P. 2005, *ApJ* , 624, 841, doi: [10.1086/429535](https://doi.org/10.1086/429535)
- Lefloch, B., Gusdorf, A., Codella, C., et al. 2015, *A&A* , 581, A4, doi: [10.1051/0004-6361/201425521](https://doi.org/10.1051/0004-6361/201425521)
- Leurini, S., Codella, C., Zapata, L. A., et al. 2009, *Astronomy & Astrophysics*, 507, 1443–1454, doi: [10.1051/0004-6361/200912783](https://doi.org/10.1051/0004-6361/200912783)
- Li, Q., Zhou, J., Esimbek, J., et al. 2018, *The Astrophysical Journal*, 867, 167, doi: [10.3847/1538-4357/aae2b8](https://doi.org/10.3847/1538-4357/aae2b8)
- Li, S., Sanhueza, P., Zhang, Q., et al. 2020, *The Astrophysical Journal*, 903, 119, doi: [10.3847/1538-4357/abb81f](https://doi.org/10.3847/1538-4357/abb81f)
- López-Vázquez, J. A., Lee, C.-F., Shang, H., et al. 2024, arXiv e-prints, arXiv:2411.01728, doi: [10.48550/arXiv.2411.01728](https://doi.org/10.48550/arXiv.2411.01728)
- Mairs, S., Johnstone, D., Kirk, H., et al. 2017, *ApJ* , 849, 107, doi: [10.3847/1538-4357/aa9225](https://doi.org/10.3847/1538-4357/aa9225)
- Matzner, C. D., & McKee, C. F. 2000, *The Astrophysical Journal*, 545, 364–378, doi: [10.1086/317785](https://doi.org/10.1086/317785)
- Maud, L. T., Lumsden, S. L., Moore, T. J. T., et al. 2015a, *MNRAS* , 452, 637, doi: [10.1093/mnras/stv1334](https://doi.org/10.1093/mnras/stv1334)
- Maud, L. T., Moore, T. J. T., Lumsden, S. L., et al. 2015b, *Monthly Notices of the Royal Astronomical Society*, 453, 645–665, doi: [10.1093/mnras/stv1635](https://doi.org/10.1093/mnras/stv1635)
- McKee, C. F., & Tan, J. C. 2003, *ApJ* , 585, 850, doi: [10.1086/346149](https://doi.org/10.1086/346149)
- Mignon-Risse, R., González, M., & Commerçon, B. 2021, *Astronomy & Astrophysics*, 656, A85, doi: [10.1051/0004-6361/202141648](https://doi.org/10.1051/0004-6361/202141648)
- Minier, V., Ellingsen, S. P., Norris, R. P., & Booth, R. S. 2003, *Astronomy & Astrophysics*, 403, 1095–1100, doi: [10.1051/0004-6361:20030465](https://doi.org/10.1051/0004-6361:20030465)
- Motte, F., Bontemps, S., Csengeri, T., et al. 2022, *Astronomy & Astrophysics*, 662, A8, doi: [10.1051/0004-6361/202141677](https://doi.org/10.1051/0004-6361/202141677)

- Müller, H. S., Schlöder, F., Stutzki, J., & Winnewisser, G. 2005, Journal of Molecular Structure, 742, 215–227, doi: [10.1016/j.molstruc.2005.01.027](https://doi.org/10.1016/j.molstruc.2005.01.027)
- Müller, H. S. P., Thorwirth, S., Roth, D. A., & Winnewisser, G. 2001, Astronomy & Astrophysics, 370, L49–L52, doi: [10.1051/0004-6361:20010367](https://doi.org/10.1051/0004-6361:20010367)
- Nakamura, F., & Li, Z.-Y. 2012, in AIP Conference Proceedings (AIP), 30–37, doi: [10.1063/1.4754324](https://doi.org/10.1063/1.4754324)
- Nakano, T., Hasegawa, T., & Norman, C. 1995, ApJ , 450, 183, doi: [10.1086/176130](https://doi.org/10.1086/176130)
- Nisini, B., Codella, C., Giannini, T., et al. 2007, A&A , 462, 163, doi: [10.1051/0004-6361:20065621](https://doi.org/10.1051/0004-6361:20065621)
- Nutter, D., Ward-Thompson, D., & André, P. 2006, MNRAS , 368, 1833, doi: [10.1111/j.1365-2966.2006.10249.x](https://doi.org/10.1111/j.1365-2966.2006.10249.x)
- Offner, S. S. R., Lee, E. J., Goodman, A. A., & Arce, H. 2011, The Astrophysical Journal, 743, 91, doi: [10.1088/0004-637x/743/1/91](https://doi.org/10.1088/0004-637x/743/1/91)
- Pattle, K., & Ward-Thompson, D. 2015, in IAU General Assembly, Vol. 29, 2245772
- Plunkett, A., Arce, H., Mardones, D., et al. 2015, Nature, 527, 70, doi: [10.1038/nature15702](https://doi.org/10.1038/nature15702)
- Pokhrel, R., Myers, P. C., Dunham, M. M., et al. 2018, The Astrophysical Journal, 853, 5, doi: [10.3847/1538-4357/aaa240](https://doi.org/10.3847/1538-4357/aaa240)
- Pontoppidan, K. 2023, Rho Ophiuchi (NIRCAM image) | Webb. <https://webbtelescope.org/contents/media/images/2023/128/01H449193V5Q4Q6GFBKXAZ3S03?news=true>
- Preibisch, T., & Zinnecker, H. 1999, AJ , 117, 2381, doi: [10.1086/300842](https://doi.org/10.1086/300842)
- Pudritz, R. E., & Ray, T. P. 2019, Frontiers in Astronomy and Space Sciences, 6, doi: [10.3389/fspas.2019.00054](https://doi.org/10.3389/fspas.2019.00054)
- Purcell, C. R. 2006, PhD thesis, University of New South Wales, Australia
- Reipurth, B., & Bally, J. 2001, ARA&A , 39, 403, doi: [10.1146/annurev.astro.39.1.403](https://doi.org/10.1146/annurev.astro.39.1.403)
- Richer, J. S., Shepherd, D. S., Cabrit, S., Bachiller, R., & Churchwell, E. 2000, in Protostars and Planets IV, ed. V. Mannings, A. P. Boss, & S. S. Russell, 867, doi: [10.48550/arXiv.astro-ph/9904097](https://arxiv.org/abs/astro-ph/9904097)
- Robitaille, T. P., Whitney, B. A., Indebetouw, R., Wood, K., & Denzmore, P. 2006, ApJS , 167, 256, doi: [10.1086/508424](https://doi.org/10.1086/508424)
- Rohde, P. F., Walch, S., Clarke, S. D., et al. 2020, Monthly Notices of the Royal Astronomical Society, 500, 3594–3612, doi: [10.1093/mnras/staa2926](https://doi.org/10.1093/mnras/staa2926)

- Rosen, A. L., Krumholz, M. R., McKee, C. F., & Klein, R. I. 2016, MNRAS , 463, 2553, doi: [10.1093/mnras/stw2153](https://doi.org/10.1093/mnras/stw2153)
- Rosen, A. L., Offner, S. S. R., Sadavoy, S. I., et al. 2020, SSRv , 216, 62, doi: [10.1007/s11214-020-00688-5](https://doi.org/10.1007/s11214-020-00688-5)
- Safron, E. J., Fischer, W. J., Megeath, S. T., et al. 2015, ApJL , 800, L5, doi: [10.1088/2041-8205/800/1/L5](https://doi.org/10.1088/2041-8205/800/1/L5)
- Schilke, P., Walmsley, C. M., Pineau des Forets, G., & Flower, D. R. 1997, A&A , 321, 293
- Schöier, F. L., van der Tak, F. F. S., van Dishoeck, E. F., & Black, J. H. 2005, A&A , 432, 369, doi: [10.1051/0004-6361:20041729](https://doi.org/10.1051/0004-6361:20041729)
- Shu, F. H., Adams, F. C., & Lizano, S. 1987, ARA&A , 25, 23, doi: [10.1146/annurev.aa.25.090187.000323](https://doi.org/10.1146/annurev.aa.25.090187.000323)
- Skrutskie, M. F., Cutri, R. M., Stiening, R., et al. 2006, The Astronomical Journal, 131, 1163–1183, doi: [10.1086/498708](https://doi.org/10.1086/498708)
- Staff, J. E., Tanaka, K. E. I., & Tan, J. C. 2019, The Astrophysical Journal, 882, 123, doi: [10.3847/1538-4357/ab36b3](https://doi.org/10.3847/1538-4357/ab36b3)
- Stahler, S. W. 1994, ApJ , 422, 616, doi: [10.1086/173754](https://doi.org/10.1086/173754)
- Sutton, E. C., Peng, R., Danchi, W. C., et al. 1995, The Astrophysical Journal Supplement Series, 97, 455, doi: [10.1086/192147](https://doi.org/10.1086/192147)
- Tan, J. C., Beltrán, M. T., Caselli, P., et al. 2014, in Protostars and Planets VI, ed. H. Beuther, R. S. Klessen, C. P. Dullemond, & T. Henning, 149–172, doi: [10.2458/azu_uapress_9780816531240-ch007](https://doi.org/10.2458/azu_uapress_9780816531240-ch007)
- Team, T. C., Bean, B., Bhatnagar, S., et al. 2022, Publications of the Astronomical Society of the Pacific, 134, 114501, doi: [10.1088/1538-3873/ac9642](https://doi.org/10.1088/1538-3873/ac9642)
- Towner, A. P. M., Ginsburg, A., Dell’Ova, P., et al. 2023, The Astrophysical Journal, 960, 48, doi: [10.3847/1538-4357/ad0786](https://doi.org/10.3847/1538-4357/ad0786)
- Turner, B. E. 1991, The Astrophysical Journal Supplement Series, 76, 617, doi: [10.1086/191577](https://doi.org/10.1086/191577)
- Tychoniec, Ł., Hull, C. L. H., Kristensen, L. E., et al. 2019, A&A , 632, A101, doi: [10.1051/0004-6361/201935409](https://doi.org/10.1051/0004-6361/201935409)
- Tychoniec, Ł., van Dishoeck, E. F., van ’t Hoff, M. L. R., et al. 2021, Astronomy & Astrophysics, 655, A65, doi: [10.1051/0004-6361/202140692](https://doi.org/10.1051/0004-6361/202140692)
- van der Marel, N., Kristensen, L. E., Visser, R., et al. 2013, Astronomy & Astrophysics, 556, A76, doi: [10.1051/0004-6361/201220717](https://doi.org/10.1051/0004-6361/201220717)

- van der Tak, F. F. S., Black, J. H., Schöier, F. L., Jansen, D. J., & van Dishoeck, E. F. 2007, *Astronomy & Astrophysics*, 468, 627–635, doi: [10.1051/0004-6361:20066820](https://doi.org/10.1051/0004-6361:20066820)
- Van Kempen, T. A., van Dishoeck, E. F., Salter, D. M., et al. 2009, *Astronomy & Astrophysics*, 498, 167–194, doi: [10.1051/0004-6361/200810445](https://doi.org/10.1051/0004-6361/200810445)
- Van Kempen, T. A., Hogerheijde, M. R., van Dishoeck, E. F., et al. 2016, *Astronomy & Astrophysics*, 587, A17, doi: [10.1051/0004-6361/201424725](https://doi.org/10.1051/0004-6361/201424725)
- Velusamy, T., & Langer, W. D. 1998, *Nature*, 392, 685, doi: [10.1038/33624](https://doi.org/10.1038/33624)
- Walsh, A. J., Burton, M. G., Hyland, A. R., & Robinson, G. 1999, *Monthly Notices of the Royal Astronomical Society*, 309, 905–922, doi: [10.1046/j.1365-8711.1999.02890.x](https://doi.org/10.1046/j.1365-8711.1999.02890.x)
- Whitney, B. A., Wood, K., Bjorkman, J. E., & Wolff, M. J. 2003, *ApJ*, 591, 1049, doi: [10.1086/375415](https://doi.org/10.1086/375415)
- Wienen, M., Wyrowski, F., Menten, K. M., et al. 2015, *Astronomy & Astrophysics*, 579, A91, doi: [10.1051/0004-6361/201424802](https://doi.org/10.1051/0004-6361/201424802)
- Wilking, B. A., Gagné, M., & Allen, L. E. 2008, in *Handbook of Star Forming Regions*, Volume II, ed. B. Reipurth, Vol. 5, 351, doi: [10.48550/arXiv.0811.0005](https://arxiv.org/abs/0811.0005)
- Williams, J. P., Plambeck, R. L., & Heyer, M. H. 2003, *ApJ*, 591, 1025, doi: [10.1086/375396](https://doi.org/10.1086/375396)
- Wilson, T. L., & Rood, R. 1994, *ARA&A*, 32, 191, doi: [10.1146/annurev.aa.32.090194.001203](https://doi.org/10.1146/annurev.aa.32.090194.001203)
- Woosley, S. E., Heger, A., & Weaver, T. A. 2002, *Reviews of Modern Physics*, 74, 1015, doi: [10.1103/RevModPhys.74.1015](https://doi.org/10.1103/RevModPhys.74.1015)
- Wu, Y., Wei, Y., Zhao, M., et al. 2004, *A&A*, 426, 503, doi: [10.1051/0004-6361:20035767](https://doi.org/10.1051/0004-6361:20035767)
- Yang, B., Stancil, P. C., Balakrishnan, N., & Forrey, R. C. 2010, *ApJ*, 718, 1062, doi: [10.1088/0004-637X/718/2/1062](https://doi.org/10.1088/0004-637X/718/2/1062)
- Yıldız, U. A., Kristensen, L. E., van Dishoeck, E. F., et al. 2012, *Astronomy & Astrophysics*, 542, A86, doi: [10.1051/0004-6361/201118368](https://doi.org/10.1051/0004-6361/201118368)
- Zhang, Q., Wang, K., Lu, X., & Jiménez-Serra, I. 2015, *The Astrophysical Journal*, 804, 141, doi: [10.1088/0004-637x/804/2/141](https://doi.org/10.1088/0004-637x/804/2/141)